NORTHWESTERN UNIVERSITY

A Biorobotic Study of the Rat Whisker System

A DISSERTATION

SUBMITTED TO THE GRADUATE SCHOOL

IN PARTIAL FULFILLMENT OF THE REQUIREMENTS

for the degree

DOCTOR OF PHILOSOPHY

Field of Mechanical Engineering

By

Joseph Hai Solomon

EVANSTON, ILLINOIS

JUNE 2008

ABSTRACT

A Biorobotic Study of the Rat Whisker System

Joseph Hai Solomon

The rat whisker (vibrissal) system provides rats with an exquisitely acute tactile sense that has helped allow them to thrive all over the world. By actively rotating their whiskers back-and-forth ("whisking") against objects, rats can extract a rich variety of information including position, size, shape, orientation and texture. Today, however, we have an incomplete understanding of how the mechanical interactions between whiskers and environment can carry sufficient information to allow sensation of these features. The research presented here offers new insights to help answer these questions, and concurrently develops novel tactile sensing concepts that apply to the realm of robotics.

The methodology employed here can be conveniently divided into two parts. The first part involves the construction of analytical and numerical models to describe how whiskers bend and transmit forces and moments in response to mechanical deflections. Also, a functional model is derived to explain how three-dimensional (3-D) object feature extraction is possible with rat whiskers. The second part involves the construction and testing of a robotic array of whiskers to validate the effectiveness of the model, and to also reveal additional aspects of the sensory task

that are difficult to identify through other methods of study such as computer simulation or high-speed video analysis. The results of this thesis should be of interest both to those involved in the study of the rat whisker system, and those interested in the field of robotic tactile sensing.

Acknowledgements

I hold a great deal of appreciation for the advice, guidance and support of a number of people.

My advisor, Professor Mitra Hartmann, has roused a great deal intellectual motivation and maturity on my part over the last four-and-a-half years, which continues to grow. She deserves credit as the architect of the overall approach taken by this research, in addition to many specific ideas. I also owe her tremendous gratitude for her meticulous proofreading, our stimulating discussions and her overall guidance.

Many thanks to my thesis committee – Professors Steven Gard, Kevin Lynch, and Michael Peshkin – for their involvement and astute suggestions. Additional thanks to Dr. Peshkin for his expert advice in debugging electronics, and Dr. Gard for proofreading this thesis.

The importance of studying in a lab with intelligent and personable students (and post-docs) during one's graduate studies cannot be understated. To this end, I was remarkably fortunate to work and become friends with Alex Birdwell, Venkatesh Gopal, Aniket Kaloti, Brian Quist, Chris Schroeder, Aimee Schulz, Mike Taylor, Montakan (Ploy) Thajchayapong, and Blythe Towal.

My wonderful girlfriend Margaret Spencer (MS) has tolerated the many consequences of my busy schedule with *seldom* more than brief spout of dissention. More importantly, her

immense confidence in my potential gives me extra ambition to achieve and to hopefully make the world a slightly better place.

I am mightily grateful to have such a close family. Thanks to Julie for laughing and making me feel smart when I'd explain my research, Becky for accepting when I couldn't attend family vacations, and Tammy for understanding the wholly inadequate amount of time I've spent with her two precious young daughters, Morgan and Ava. Finally, I would like to thank my parents, Carol and Hai, whose wisdom, love and never-ending support is the greatest of blessings.

For my parents, Carol and Hai, to whom I owe everything.

Table of Contents

List of Tables

List of Figures

Chapter 1

Introduction

Rats are one of the most widespread mammals on Earth due to their extraordinary ability to adapt to a diversity of environments. The Norwegian rat (*rattus norvegius*) in particular has populated nearly every area on the planet that humans have [1]. Because rats live much of their lives underground in burrows and have low acuity vision [2], tactile sensation plays a pivotal role in allowing them to navigate and find food. The rat whisker system provides tactile information through a behavior known as "whisking," wherein all the whiskers on each cheek are actively rotated back-and-forth against objects at about 5-12 Hz in a relatively stereotyped, rhythmic pattern [3]. Whisking provides rats with a highly acute and robust tactile window to their environment, providing detailed information about objects' position, size, shape, orientation and texture [4-7]. This remarkable ability has caught the attention of a large number of neuroscientists interested in understanding the fundamental principles involved in the process of active sensing. I personally am not a neuroscientist (although my interest in the field has grown faster than my understanding). However, as a mechanical engineer, my educational background

has given me a different perspective from which I have attempted to shed new light on the rat whisker system. The approach I have taken draws heavily on the engineering disciplines of Euler-Bernoulli beam theory and robotics, making the results of interest to a particularly diverse audience. The remainder of this chapter will explain and motivate the approach taken in this research, and give an overview of this thesis.

1.1 Motivation

The fundamental relationships between movement and sensing that guide the behavior of all animals have proven very difficult to understand due to the highly complex interaction between nervous system, body and external environment. At the same time as incoming sensory stimuli are interpreted in the context of outgoing motor commands, the resulting sensations determine the subsequent sequence of movements, forming a highly dynamic feedback loop. The rat whisker system possesses many unique properties that may help unravel the computational principles underlying this process. In terms of movement, whisking is largely rhythmic and stereotyped, and hence can be comprehensively described with few parameters. Having very little mass, whiskers are also negligibly affected by inertial forces and do not disturb the environment. In terms of sensing, whiskers gather discrete bundles of information, which can be described through units of force, moment and their derivatives. Nearly every stage of neural processing then architecturally preserves the neat, grid-like arrangement of whiskers on each whisker pad [8], allowing neuroscientists to study sensory acquisition in a highly structured context.

Despite these favorable properties, a cohesive, explicit framework to explain the remarkable acuity of the whisker system has remained elusive. Part of the reason is the incompleteness of the traditional investigative toolset, broad though it may be. This includes electrodes to measure the spiking of neurons, computer programs to test hypotheses about neural processing models, high-speed video to track the movement of the whiskers, and behavioral experiments to reveal underlying functional principles. What's lacking here is an accurate model of the complex physical interactions that take place between whiskers and environment. This is not a profound idea; models are one of the basic pillars of scientific inquiry and understanding [9, 10]. However, it is not entirely uncommon for this basic component of problem solving to be underused, and I believe the study of rat whisker system has suffered from this. This thesis serves to help fill that gap.

1.2 Approach

Central to the modeling approach that I have undertaken during the course of my research has been the incorporation of analytical, numerical and robotic techniques. The interaction between the three, shown in Figure 1.1, effectively induced a synergistic effect, wherein new ideas were motivated, formalized, validated and implemented in such a way that would not be possible if any one component were missing. This will be further reflected upon in the Conclusion.
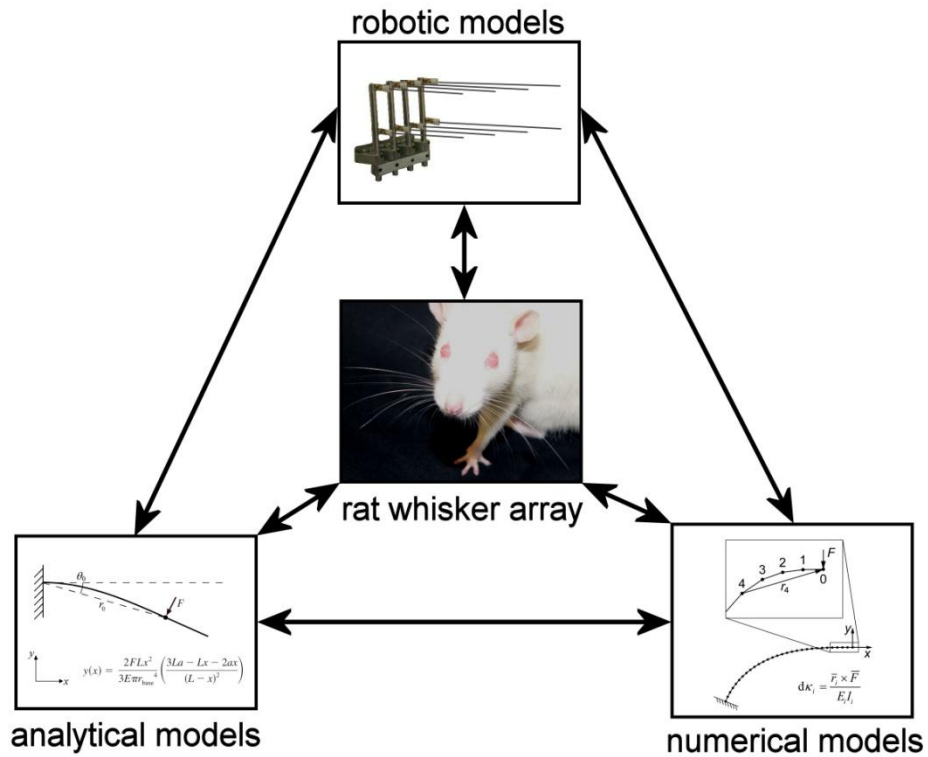
Figure 1.1: The synergistic interactions between analytical, numerical and robotic modeling techniques led to new insights about the rat whisker system.

This overall approach clearly falls under the domain of biorobotics [11]. Along with the growing appreciation for how the complex yet subtle interactions and feedback loops between animal and environment lead to the emergence of behavior, the multidisciplinary field of biorobotics has developed. Given the enormous difficulty in accurately modeling the physical world in simulation, many scientists have turned to robots to help answer specific questions regarding the operation of animal motor systems. Likewise, due to the amazing agility and adaptability displayed by animals, engineers have incorporated aspects of neural control and biomechanics (neuromechanics) [12] into robots. More often than not these two motivations overlap, making the biorobotic approach especially productive.

Beer *et al.* [13] recommend the following sequence of steps to maximize the utility of the biorobotic approach:

1. *Identify a biological hypothesis that is difficult to address experimentally.*

2. *Design a biorobot that captures the essential physical properties required to address the biological question of interest.*

3. *Test the feasibility of the original biological hypothesis on the biorobot.*

The research I have carried out has iterated through these steps several times, but without the need to reconstruct the robot. In other words, several different hypotheses were developed, but the robotic platform was built to be scalable and adaptable to address the specific experimental requirements.

In keeping with the multifaceted nature of biorobotics, several equations, algorithms and technologies were developed that have relevance to the field of robotic tactile sensing, which is rapidly growing [14]. Rats are nature's testament to the effectiveness of whiskers as robust tactile sensors in unstructured environments, and bear credence to the potential for robotic counterparts [15], [16]. The work presented here is thus highly relevant to mobile robots, in addition to several other specific robotic applications (see Chapter 4).

This section now concludes with the important remark that this research has focused on object feature extraction primarily from a functional point of view. The term "rat whisker system" not only refers to a collection of whiskers, but also the remarkably complex and interconnected web of neural structures that control their movement and process the resulting mechanoreceptor activity. No such neuronal activity was modeled here. Instead, the results serve more as basis to identify important sensory variables and formalize the fundamental mechanical

principles involved in the rat's sensations of shape. It is my hope that these ideas will lead to new testable hypotheses that will ultimately increase our understanding of the process of active sensing.

1.3 Thesis Outline

This thesis is organized in such a way that the ideas and models are developed in a smooth, cohesive manner; it does not reflect the order in which the research was carried out. The basic outline is as follows:

- Chapter 2 presents a brief overview of the rat whisker array.

- Chapter 3 develops and tests the analytical models for whisker deflection and the extraction of radial distance to an object.

- Chapter 4 addresses the issue of lateral whisker slip during object contact, and shows how it can be accounted for by sensing two components of moment.

- Chapter 5 implements the technique derived in Chapter 4 to perform detailed 3-D feature extraction on a complex object.

- Chapter 6 develops a technique for object profile extraction, wherein a continuous segment of an object can be sensed by a whisker during a single whisk.

- Chapter 7 discusses the overall results of this research.

- Appendix A outlines a technique for fitting the shapes of whiskers.

- Appendix B derives an analytical model of whisker deformation.

- Appendix C discusses the effects of taper on whisker mechanics.

- Appendix D derives the numerical model used throughout this research.

- Appendix E derives a model for lateral slip of a whisker against a flat surface.

- Appendix F derives a model for lateral slip of a whisker against a curved surface.

Chapter 2

The Rat Whisker Array

This chapter contains material that has been altered from the following publication:

2.1 Array Morphology

Rat whiskers are composed of keratin, and are structurally similar to fur or hair but with important differences. Whiskers are generally thicker and have a distinctly tapered shape, measuring between 50 and 20 μm thick at the base and about 5 μm at the tip [17]. They also gently curve along their lengths, but primarily lie flat within a plane. Rats have both large (macrovibrissae) and small (microvibrissae) whiskers on each side of the face. The microvibrissae exist around the lip region and are not actively whisked, but still play important roles in the sensing process [7]. They are generally under ~7 mm. The macrovibrissae are arranged in a grid-like pattern along the mystacial pad, which is consistent from animal to animal

(and interestingly, to a slightly lesser degree, is also evolutionarily conserved amongst mammals, including cats and pinnipeds) [4, 18]. The lengths of the macrovibrissae are fairly consistent in a given column, but smoothly vary from about 10 to up to 70 mm in the caudal (rearward) direction. Brecht *et al.* describes the lengths as exponentially increasing across rows [4]. However, the exponentiality was found to be mild, and newer research indicates that the trend may be accurately described as linear [19]. A cartoon schematic of the whisker layout is shown in Figure 2.1(a), and an actual array is shown in Figure 2.1(b).
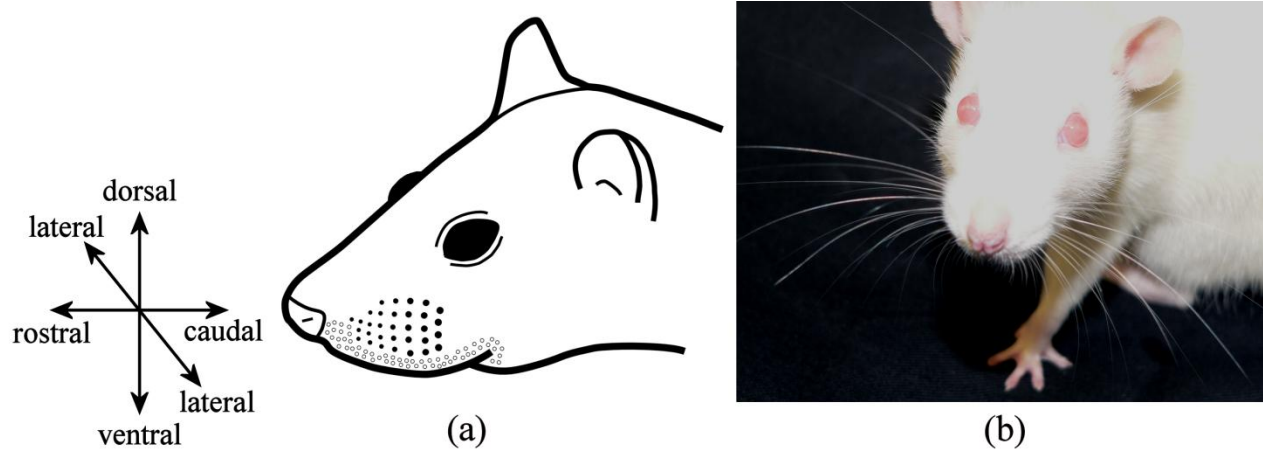
Figure 2.1: The rat whisker array. **(a)** This cartoon schematic shows the grid-like arrangement of the macrovibrissae (solid dots) along the mystacial pad, and the scattered distribution of the microvibrissae (small circles) around the lips. The varying sizes of the black dots corresponds the lengths of the associated whiskers. **(b)** A picture of an actual whisker array.

It can be seen in Figure 2.1(b) that the whiskers protrude from the mystacial pads in a smoothly-varying but elaborate 3-D configuration. Only recently has the array morphology been quantitatively described through research in my laboratory (the SeNSE lab – SEnsory and Neural Systems Engineering) [19]. The general pattern can be summarized as follows:

- In a given row, the rostrocaudal angle of emergence increases in the rostral direction, as shown by the dotted lines in Figure 2.2(a). In other words, whiskers in the front (rear) tend to emerge pointing more forwards (rearwards).

- In a given column, the dorsoventral angle of emergence increases in the dorsal direction, as shown by the dotted lines in Figure 2.2(b). In other words, whiskers higher (lower) on the mystacial pad tend to emerge pointing more vertically (downward).

- In a given column, the angle of planar orientation increases in the dorsal direction, as shown by the whisker shapes in Figure 2.2(b). In other words, the whiskers higher (lower) on the mystacial pad tend to have their tips point more vertically (downward).
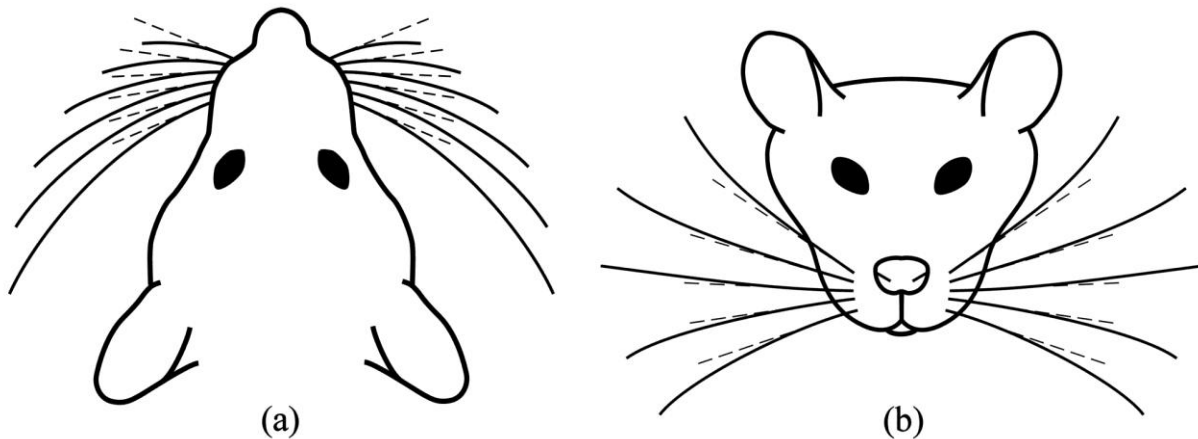
Figure 2.2: Emergence patterns of the macrovibrissae. **(a)** From the top view, the rostrocaudal trend of emergence within a given row is clear. **(b)** From the front view, both the dorsoventral trend of emergence and the pattern of planar orientation within a given column are clear. Dashed lines are tangent to the whisker bases.

2.2 Whisker Shape

Although rat whiskers are clearly curved in shape, there has been little if any systematic investigation of how they curve along their lengths. With the goal of gaining some deeper insight into their shape, I analyzed a collection of 231 whiskers (macrovibrissae) obtained from four adult female Sprague-Dawley rats. The whiskers were plucked, scanned, and processed into 2-D vector data in MATLAB using the procedure outlined in Appendix A.

Because most of the whiskers appeared to be planar, it was a natural choice to describe vibrissal shape as a plane curve. However, there are an infinite number of functional forms that can be used for this purpose. My aim was to use a characterization that was "simple" in an intuitive sense, while still accurately capturing all the essential features of the data. Initial attempts at fitting involved traditional Cartesian parameterizations such as polynomials, but it became clear that these techniques fail to reveal any intuitive meaning about the whisker shapes.

To describe whisker shape without reference to Cartesian coordinates, I used a coordinate-free representation, wherein the shape of the curve is specified by the curvature $\kappa(s)$ at each point as a function of the arc length s. Thus, the set of values $\{s, \kappa(s)\}$, completely specifies the curve intrinsically with respect to s, without reference to an external coordinate system [20].

In the absence of any *a priori* model for $\kappa(s)$, excellent fits to the data were obtained by using a linear parameterization, such that

$$\kappa(s) = as + b \tag{2.1}$$

where s is normalized by the whisker length and hence goes from 0 to 1. The fitting process involved dividing the whisker data into 20 nodes, and finding values for a and b that minimized the mean sum of squared Euclidean distances between the nodes of the normalized real whiskers

and those of the fit curves. Excellent fits were obtained using this approach with only a few exceptions, which were clearly atypically shaped whiskers. Some examples are shown in Figure 2.3.
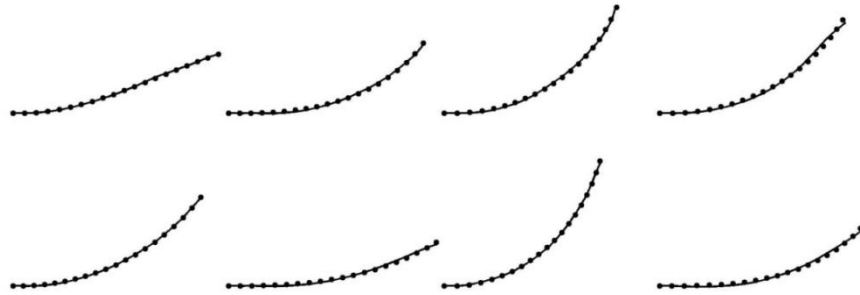
Figure 2.3: Examples of whisker fits. Solid lines are data from original whisker scans, and small dots represent nodes of the fitted curves.

Inspecting Figure 2.3, it is clear that (2.1) is able to fit a diversity of shapes. How is this possible with only two parameters? Figure 2.4 explains how the shape of a whisker can be inferred based on the coefficients of its fit, and thus helps to answer this question.
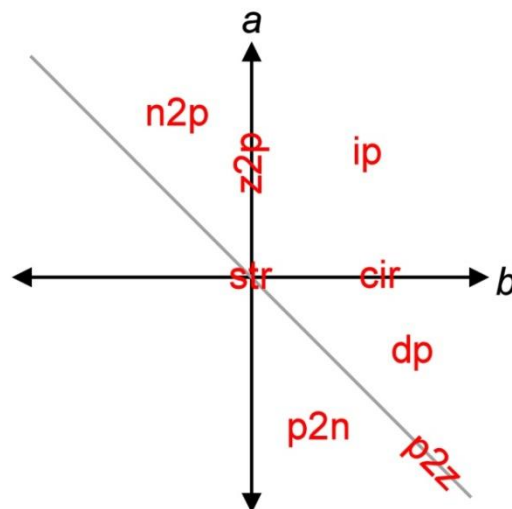
Figure 2.4: The general shape of any given whisker can be inferred from the coefficients of its fit to (2.1). Abbreviations in red refer to how the curvature changes from base to tip along the length of a whisker based on its coefficients. Abbreviations are explained in the text.

The abbreviations in Figure 2.4 have the following meanings:

- 'n2p' = negative to positive, i.e. the curvature starts out negative at the base and linearly increases along the whisker to become positive before the tip. The shape is similar to part of a sigmoid curve. Whiskers with $b < 0$ and $a > -b$ lie in this region.

- 'p2n' = positive to negative, i.e. the curvature starts out positive at the base and linearly decreases along the whisker to become negative before the tip. The shape is similar to part of a sigmoid curve. Whiskers with $b > 0$ and $a < -b$ lie in this region.

- 'z2p' = zero to positive, i.e. the curvature is zero (straight) at the base and linearly increases towards the tip. This is the line along $b = 0$ for $a > 0$.

- 'p2z' = positive to zero, i.e. the curvature starts out positive at the base and linearly decreases along the whisker to become zero (straight) at the zip. This is the line along $a = -b$ for $b > 0$.

- 'ip' = increasingly positive, i.e. the whisker curvature is positive at the base and linearly increases towards the tip. Whiskers with $b > 0$ and $a > 0$ lie in this region.

- 'dp' = decreasingly positive, i.e. the whisker curvature is positive at the base and linearly decreases towards the tip, but remains positive. Whiskers with $a > -b$ and $a < 0$ lie in this region.

- 'cir' = circular, i.e. the curvature is constant and hence the whisker shape is a segment of a circle. This is the line $a = 0$ for $b > 0$.

- 'str' = straight, i.e. the curvature is zero along the entire whisker and hence the whisker is a straight line segment. This is the origin $(0, 0)$.

Clearly a rich variety of shapes are possible using (2.1) – shapes which accurately describe rat whiskers. Now equipped with an intuitive understanding of the fit parameters, Figure 2.5 plots *a* vs. *b* for all the whiskers, revealing that they are closely correlated.

The plot shows data with fit equations:

$$a = -2.06b + 1.87$$
$$r^2 = -0.86$$
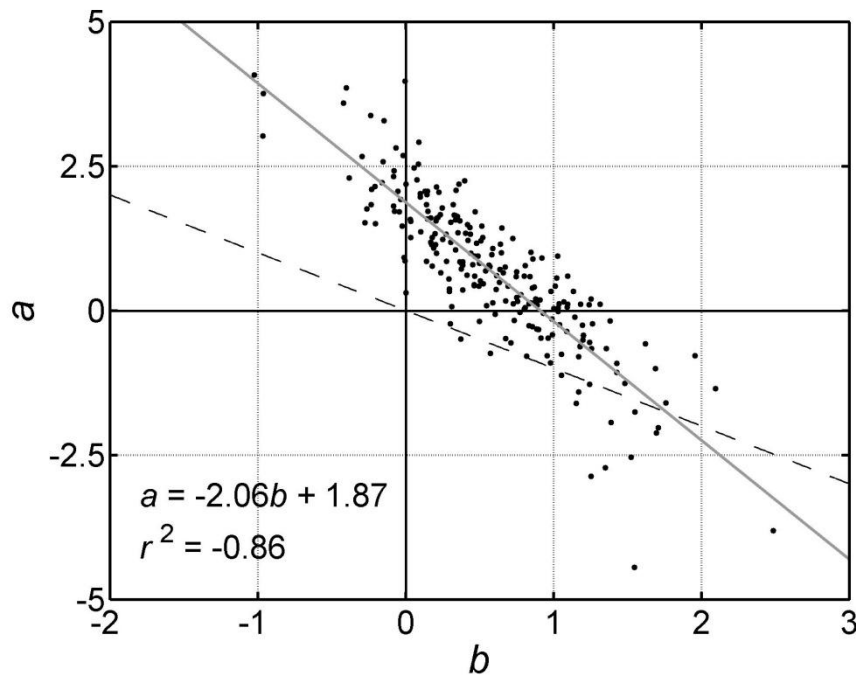
Figure 2.5: Fits from 231 whiskers shows that the fit coefficients are highly correlated. The gray line is a linear fit, and the dashed line is *a* = –*b.*

Interestingly, Figure 2.5 shows that not only are all basic types of whisker shapes outlined in Figure 2.4 embodied by actual whiskers, but also that there is a clear linear trend which describes the distribution of the coefficients. The reason for this trend is currently the subject of further investigation.

Chapter 3

Radial Distance Extraction

This chapter contains material that has been slightly altered from the following publication:

3.1 Introduction

Rats use their mystacial vibrissae during navigation and exploratory behaviors to 3-D object features, including size, shape, orientation, location, and texture [4, 5, 21-24]. To extract these complex 3-D features, the rat must at least implicitly estimate the distance from the base of the whisker to the point of object contact. However, the mechanism for radial distance encoding by a single whisker seems problematic, because mechanoreceptors are located only at the base of the whisker, within the follicle [25-27]. This means that object position cannot be directly measured by the location of contact on the whisker. Instead, the whisker's interaction with the environment must be transduced into parameters that can be measured at the whisker base.

It is well known that the length of the rat's whiskers varies from long to short along the caudal-rostral dimension [4, 28, 29]. Thus one plausible mechanism for radial distance encoding is for the rat to compare the identity of whiskers that contacted an object with those that did not. If a whisker of length L touched an object, but a whisker of length $L - \Delta L$ did not, the rat could infer that the object was located at a distance between those two values (after accounting for different whisker base locations). Behavioral studies have shown, however, that rats can determine aperture width with only one whisker remaining on each side of the face [30]. This suggests that cross-whisker comparisons cannot fully explain the rat's distance discrimination capabilities.

A preliminary analysis of the whisker as a cantilever beam suggested that the stiffness properties of the whisker might provide a mechanical explanation for the rat's ability to perform accurate radial distance discriminations. We specifically hypothesized that information about moment at the whisker base is critical for determining radial object distance. To test this hypothesis, we developed two closely-related biomechanical models of the whisker. Both models were deliberately developed in analytic form, so that researchers could easily calculate moment at the whisker base during experiments. The analytical models were tested against numerical simulations to quantify limits on their application, and together with experimental results confirmed our hypothesis: by correlating movement to changes in moment at the whisker base the rat could determine the radial distance of an object.

This work continues our characterization of vibrissa dynamics [29], and suggests some useful ways to represent the mechanical information encoded in the primary sensory neurons of the trigeminal ganglion (Vg). We interpret these results in the context of our evolving hypothesis

that neural responses in Vg can be comprehensively represented using a state-encoding scheme that includes combinations of four and only four mechanical variables at the whisker base: angular position, angular velocity, moment, and rate of change of moment.

3.2 Methods

3.2.1 Whisker Preparation for Static and Dynamic Experiments

The present analysis is based on a total of seven vibrissae obtained from three female Sprague Dawley rats that had been sacrificed in unrelated experiments. All procedures were approved in advance by Northwestern University's Animal Care and Use Committee. Each whisker was grasped firmly at the base and plucked out of the follicle for testing. Examination of the whisker by eye revealed that there was a qualitative difference in appearance between approximately the first mm of the whisker and the remainder of the whisker. Closer examination under the microscope additionally suggested that this first mm is approximately the portion of the whisker that would reside in the follicle, and we therefore used this portion to rigidly attach the whisker to the test stand or load cell during experiments.

3.2.2 Static Experiments to Determine Whisker Flexural Characteristics

A micromechanical force tester (Mach-1, BioSyntech, Montreal, Canada), was used to impose small vertical displacements on the whisker at known horizontal distances from the base and to measure the associated force. The Mach 1 has a positional accuracy of 1.5 μm, and we used a 50-gram load cell to achieve a load resolution of 0.0025 grams. This allowed us to

characterize force-bending relationships for all but the smallest whiskers. Images of the whiskers as they were bent during the experiment were acquired with a high-resolution (3088 by 2056 pixels) digital camera (Digital EOS Rebel, Canon, Inc**.**).

Figure 3.1(a) shows the experimental set up used to perform the static force measurements. Whiskers were rigidly fixed at their base to a cylindrical metal test stand using cyanoacrylate (superglue). All whiskers were mounted concave down. A shallow groove one mm in length was etched in the top face of the stand. The whisker was placed directly in the groove to ensure that exactly the first mm of the whisker was rigidly attached to the stand. As described above, this first mm is likely to correspond to the portion of the whisker which would normally reside inside the follicle. Miniature scales (Minitool, Los Gatos, CA) with 100 μm tick-marks were attached both vertically and horizontally to the side of the cylindrical stand. These scales provided an independent measure of displacement that could be compared with the positions given by the Mach-1 micromechanical tester. The inset of Figure 3.1(a) shows a close up view of the stimulator used to deflect the whisker. The stimulator was custom-machined to a fine taper so that the width that ultimately contacted the whisker was ~500 μm.
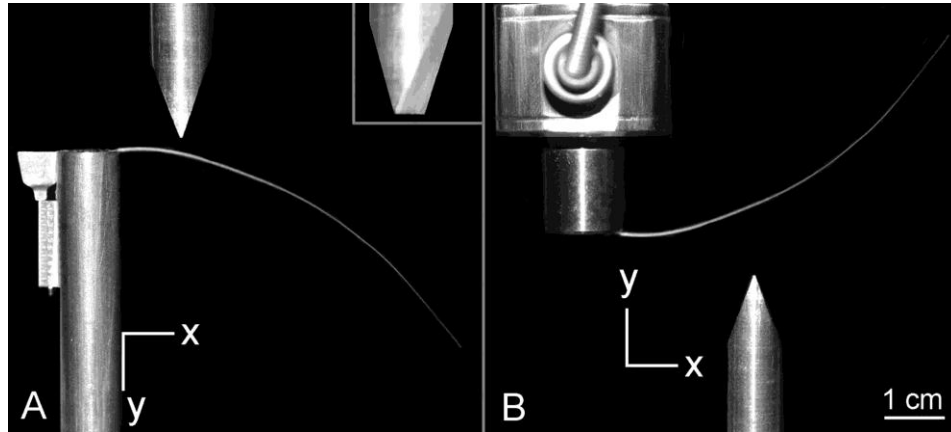
Figure 3.1: Experimental measurement of static and dynamic forces. **(a)** In static experiments the first 1 mm of each plucked whisker was glued rigidly to a cylindrical post with horizontal and vertical scales fixed to the left side. A tapered stimulator (inset shows side view) attached to a load cell was gradually lowered into the whisker at different distances from the whisker base. The load cell thus directly measured the force necessary to displace the whisker a known vertical distance (*y*), at a particular radial distance (*x*). **(b)** In dynamic experiments the base of the whisker was mounted directly to the load cell, and then translated into the tapered stimulator. Note that the *y*-axis is reversed for directional consistency. The tapered stimulator was held fixed and positioned at different radial distances from the whisker base. Under these conditions, the load cell directly measured the force at the whisker base as the whisker was increasingly deflected over time, at a particular radial distance. In both static and dynamic experiments the contact width of the stimulator on the whisker was approximately 500 μm. Also note that because the load cell in the Mach-1 tester measured only vertical force, the measured force was divided by the cosine of the whisker angle at the contact point to obtain the actual force applied.

At the beginning of each static experiment, the stimulator was rigidly attached to the Mach-1 load cell and carefully positioned in both *x*- and *y*-directions. In the *x*-direction, the stimulator was positioned at the right-most edge of the test stand, and this position was defined as $x = 0$. In the *y*-direction, the stimulator was positioned just above the surface of the base of the whisker, and this position was defined as $y = 0$. The stimulator was then lowered in small (100 μm) intervals in the *y*-direction (computer-controlled via the Mach-1 micromechanical tester) to

precisely displace the stationary whisker. The stimulator was lowered until the whisker had been deflected 1,500 μm (1.5 mm). Forces from the load cell were recorded at every step for every whisker, and digital pictures of the whisker's bending were taken at every step for all seven whiskers. Note that in these static experiments, the load cell measured the vertical force necessary to displace the whisker a known vertical distance, at a particular distance from the whisker base. It did not measure the force at the base of the whisker.

After the whisker had been deflected through a full 1,500 μm, the stimulator was moved back to $y = 0$ so that it no longer contacted the whisker. The stimulator was then moved in the positive x-direction, to a different horizontal distance from the base of the whisker. We typically moved the stimulator in 2,000 μm increments in the x-direction, but for some whiskers we moved in 1,000 μm intervals. The stimulator was again positioned carefully just barely above the surface of the whisker, this position was defined as a new $y = 0$, and the stimulator was then lowered to displace the whisker at this new x-location. We continued moving the stimulator further out horizontally from the base of the whisker until we reached the resolution of the force measurement capabilities of the Mach 1 tester.

3.2.3 Dynamic Experiments to Determine Whisker Flexural Characteristics

In dynamic experiments, the whisker base was mounted directly to the load cell and moved using the Mach-1 tester to hit the tapered stimulator, which was held fixed in position. This experimental setup is shown in Figure 3.1(b) and allowed us to continuously monitor the force at the base of the whisker as it deflected into the stimulator. We lowered each whisker into the

stimulator at two different velocities (50 μm/sec, and 500 μm/sec), and at five different horizontal locations away from the whisker base (3, 5, 7, 9, and 11 mm). Note that the *y*-direction is opposite that in Figure 3.1(a) for directional consistency with respect to the whisker.

3.2.4 Analysis of Experimental Data

Force and displacement data (from the Mach-1 tester), along with the digital images of the whiskers, were imported into MATLAB (v 7.0, 2004, The Mathworks, Nattick, MA). As is the convention for load cells, the load measurements from the Mach-1 were provided in grams. These measurements were multiplied by a factor of 9.8 meters/second^2 to account for the acceleration due to gravity and obtain the force in micronewtons (μN). Whisker-stimulator contact forces were always assumed to be normal to the whisker because the contribution of force from friction was negligible. The load cell in the Mach-1 tester measured only vertical force, and we therefore divided the measured force by the cosine of the whisker angle at the contact point to obtain the actual force applied.

To extract the geometrical shapes of the whiskers from the high-resolution photographs, the upper and lower outlines of the whisker were located using semi-automated image processing techniques in MATLAB. The shape of the whisker was then defined as the average of the upper and lower outlines. For each extraction the averaged points were overlaid on top of the photographed whisker to visually confirm that the averaging technique yielded data points that fell within the upper and lower outlines of the whisker, thus giving an excellent match to the overall shape.

3.2.5 Fundamentals of Elasticity: Cantilever Beam Theory

Our goal in this research was to develop an accurate but simple biomechanical model of the rat whisker as a cantilevered beam. Cantilever beam models are derived from elasticity theory [31-34], which relates the curvature, κ, of a cantilever beam to the moment, M, at each point along its length, x:

$$\kappa(x) = \frac{\dfrac{d^2 y}{dx^2}}{\left[1 + \left(\dfrac{dy}{dx}\right)^2\right]^{\frac{3}{2}}} = \frac{M(x)}{EI} \tag{3.1}$$

In (3.1), $y(x)$ is the displacement of the beam at each x location along the length, E is Young's modulus (also called the elastic modulus), and I is the area moment of inertia. In general, Equation (3.1) can only be solved numerically, but for small angle deflections ($< \sim 14$ degrees), the term $\left(\dfrac{dy}{dx}\right)^2$ in the denominator is negligible and (3.1) can be linearized as

$$\kappa(x) = \frac{d^2 y}{dx^2} = \frac{M(x)}{EI} \ , \quad \text{where } M(x) = \begin{cases} F(a-x), & 0 \leq x \leq a \\ 0 & , \quad a \leq x \leq L \end{cases} \tag{3.2}$$

In (3.2), F is the force exerted normal to the beam at a distance along the whisker, a, from the base of the beam. The linearization assumes that the beam is initially straight and that it deflects only through small angles. This means that the arc length distance a, is essentially the same as a horizontal distance.

If we now assume that the beam is cylindrical with a radius of r at the base, then the area moment of inertia $I = \pi r^4 / 4$ and (3.2) can be solved analytically for $y(x)$:

$$y(x) = \begin{cases} \dfrac{F}{6EI}(3x^2a - x^3) & , \quad x \le a \\[12pt] \dfrac{F}{6EI}(3a^2x - a^3) & , \quad x > a \end{cases} \tag{3.3}$$

Note that $y(x)$ is linear with horizontal position x for values of x greater than a. We adapted this model of the cylindrical beam into a model for the tapered beam (see the Results section and Appendix B), to more accurately represent the morphology of real rat whiskers.

It is important to note that elasticity theory itself is very general, simply relating curvature to moment. However, for biological materials Young's modulus (E) is an approximation at best, because these materials are typically anisotropic, heterogeneous, and nonuniform. For a material whose value of E is roughly 5 GPa, the best one might expect is to obtain a value correct to within a few gigapascals.

3.2.6 Comparing Results of Model 1 With Experimental Results

Our analysis required a comparison of the shape of the whisker as predicted by our tapered beam model (Model 1) with the shape of the real whisker obtained experimentally with high resolution photography. However, real rat whiskers have an inherent curvature. We therefore made the approximation that the deflection of the real whisker (under a force F at a particular arc length location, a) could be expressed as the deflection of a straight tapered cantilever beam (under that same force F, imposed at the same location a), summed with the inherent curved shape of the undeflected whisker (under conditions of zero force). This approximation is schematized in Figure 3.2. This analysis is valid as long as the assumptions of the linearized

beam model are not violated, namely that the deflections and inherent whisker curvature are sufficiently small. The first part of the Results section identifies the conditions in which these assumptions are valid.
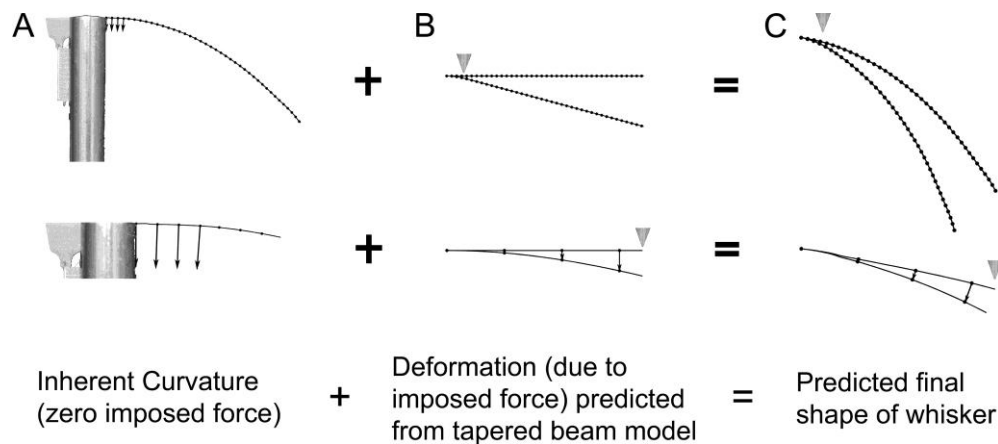
Figure 3.2: Geometrical method used to predict the final shape that a whisker will assume under an imposed force. The predicted whisker shape was found by summing the inherent curvature of the whisker (from a photo) with the curvature resulting from an imposed force as predicted by the tapered beam model. The top row shows deflections of the entire whisker, while the bottom row shows enlarged versions of the region near the base for visual clarity. In each figure, the upside-down triangle indicates the position of the applied force. **(a, top)** Under conditions of zero force, the (undeflected) shape of the whisker was extracted from a photograph and partitioned with nodes spaced at equal arc lengths. This quantified the inherent curvature of the whisker. **(a, bottom)** The inward pointing unit normal was found for all nodes between the base of the whisker and the stimulator contact point. **(b, top)** Model 1 was used to predict the deflection of a linearly-tapered cantilever beam with the same dimensions as the real whisker (base diameter and length). The modeled beam was partitioned with equally-spaced nodes as in (a). **(b, bottom)** The vertical distance that each node traveled from the undeflected to the deflected case was found. **(c, top and bottom)** The magnitude of the vertical deflection for each node in (b) was added to its corresponding node in (a), in the associated unit normal direction shown in (a, bottom). It is clear from (c, top) that even a very small deflection imposed near the whisker base can have a large effect on the position of the tip of the whisker.

Summing the deflection of the tapered cantilever beam (from analytical equations) with the inherent curvature of the undeflected whisker (from photography), required some careful

geometrical analysis. The summation process involved three steps, and is schematized in Figure 3.2. First, thousands of nodes along the (real, undeflected) whisker were placed at constant arc length (Figure 3.2(a)). Second, the arc lengths from the base of the whisker to each of the nodes were used as the *x*-values in the deflection equation to analytically solve for the small-angle deflection of a tapered cantilever beam ((3.5) in the Results section). Figure 3.2(b) shows the magnitude of the vertical deflection for each node. For small angles, the path of deflection can be assumed to follow a vertical translation instead of an arc [34]. Third, the resulting deflection values were added to each node along the undeflected whisker in an inward-pointing normal direction to the whisker at each node (Figure 3.2(c)). This three-step procedure has a very intuitive underpinning: it simply ensured that equivalent deflections were summed between the theoretical model and the experimentally-obtained photographs.

Note that for this model, nodes beyond the point of whisker-stimulator contact deflect linearly, as can be seen mathematically in (3.3). In the model, we could therefore assume that the portion of the whisker past the stimulator contact point was translated in the same direction as the last node before the stimulator contact. This portion of the whisker was thus aligned to match the tangent of the deflected whisker at the point of contact.

3.2.7 Numerical Simulations

Numerical simulations of whisker bending were performed in order to identify the limitations on and validate the results of the two analytical models. These numerical simulations also accounted for large angle deflections and inherent whisker curvature. All simulations were performed in MATLAB, and were based on the following principle: if a force $\bar{F}$ acts at an arc

length *a* from the base of a beam, the resulting beam shape can be found by dividing the beam into many nodes and repeatedly applying $d\kappa_i = (\bar{r}_i \times \bar{F}) / EI_i$, where $d\kappa_i$ is the change in curvature at node *i*, $\bar{r}_i$ is the vector connecting node *i* to *a*, and I_i is the area moment of inertia at node *i*. $\bar{F}$ always acts normal to the whisker as long as there is no friction. This procedure is further explained in Appendix D.

3.3 Results

We began by considering how best to realistically model a rat whisker. We noted three inadequacies of the analytical model of the cylindrical cantilever beam presented in (3.2) and (3.3):

1) The model assumes a cylinder, but the real whisker is tapered, as a cone.

2) The model assumes a straight beam, but the real whisker has inherent curvature.

3) The model is linearized, assuming only small angle deflections (no more than ~ 14°), but the real whisker can bend through very large angles during object contact.

The results below account for each of these three complexities, and are divided into three parts. In Part 1, we develop an analytical model (Model 1) to describe the bending of a rat whisker. The model uses the magnitude and location of the imposed force to determine the resultant shape of the whisker after deflection. The model accounts for both whisker taper and inherent whisker curvature, and limits on its applicability are tested using numerical simulations.

In Part 2, we validate Model 1 against experimental data obtained from real rat whiskers, demonstrating an excellent match between theory and experiment. Finally, in Part 3, we develop

a second analytical model (Model 2) that describes the relationship between the rate of change of moment at the whisker base and radial object distance. Numerical simulations are used to show that the inherent curvature of the whisker has a negligible effect on this relationship. We demonstrate that measuring changes in moment at the whisker base would permit the rat to extract radial object distance, and analyze the consequences of this result for coding in the trigeminal ganglion.

3.3.1 Part One: Developing an Analytical Model of a Tapered Rat Whisker With Inherent Curvature

3.3.1.1 An Analytical Expression for the Deformation of a Tapered Whisker With No Inherent Curvature

Expressions for the deflection of a straight cylindrical cantilever beam under a load are readily available in the literature [34]. However, the diameter of a rat whisker decreases approximately linearly with length [28, 29]. We therefore extended the cylindrical model to account for the taper of the whiskers. The basic derivation for tapered deflections is the same as for the cylindrical case, and can be found in Appendix B. The analytic solution for the small-angle deflections of a tapered beam was found to be:

$$
y(x) = \begin{cases}
\dfrac{2FLx^2}{3E\pi r_{\text{base}}^4}\left(\dfrac{3La - Lx - 2ax}{(L-x)^2}\right), & x \leq a \\[4ex]
\dfrac{2FLa^2}{3E\pi r_{\text{base}}^4}\left(\dfrac{3Lx - La - 2ax}{(L-a)^2}\right), & x \geq a
\end{cases}
\tag{3.4}
$$

Comparison of (3.4) with (3.3) shows clearly that a whisker's taper has a substantial effect on its deformation characteristics; these effects are quantified in detail in Appendix C.

3.3.1.2 Effects of Taper on the Small Angle Approximation

The small angle assumption implicit in the linearization of (3.1) means that the deformations expressed in (3.4) will become inaccurate after a certain bending angle. We used numerical simulations (see Appendix D) to explore how linearization impacts the accuracy of the analytical model under large angle deflections and inherent whisker curvature.

Figure 3.3(a) illustrates the difference between the small-angle approximation and the large-angle numerical result for a 200 μN force applied at distances of 10, 20, and 30 mm out along a 60 mm tapered whisker. For the first two locations of applied force, the difference between the small angle approximation (dotted line) and the numerical result (solid line) is negligible. When the force is applied at 30 mm the small angle approximation clearly diverges from the numerical result as the deflection angle becomes sufficiently large. The effect of taper increases for deflections applied further from the base.
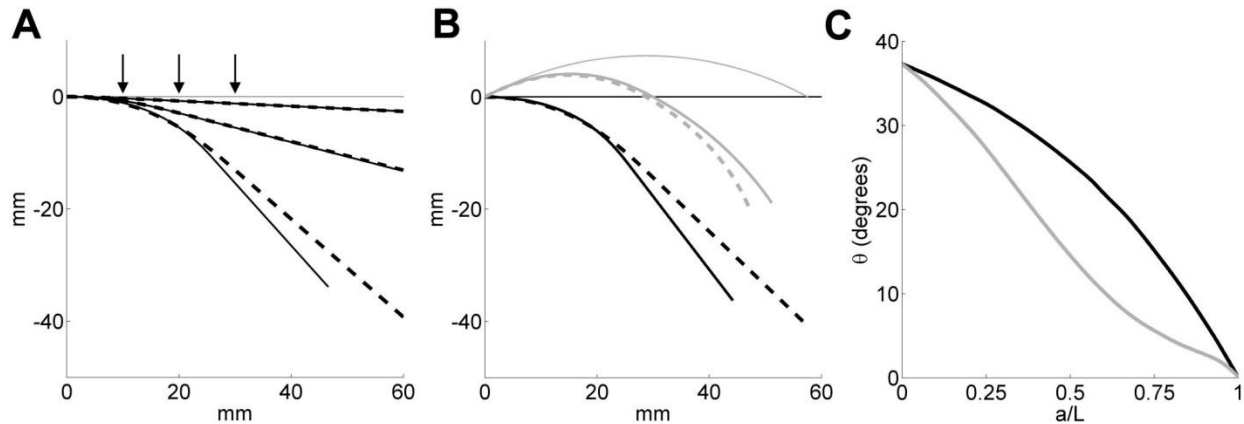
Figure 3.3: Effects of taper and inherent curvature on the small angle approximation. **(a)** The effect of the small-angle approximation is exemplified by imposing a 200 µN force at 10, 20, and 30 mm from the base of a straight, tapered 60 mm whisker and comparing the small-angle (linearized, analytic) and large-angle (numerical) results. Results using the small angle approximation are shown as dotted lines and results for the full numerical solution are shown as solid lines. Because the deflections increase as the force is exerted further from the base, the small angle assumption begins to break down and the curves accordingly diverge. **(b)** Comparison of analytical and numerical results after including the effects of inherent whisker curvature. The thin lines represent an undeflected straight whisker (black; overlaps with the *x*-axis) and an undeflected curved whisker (grey). Normalized curvature of the curved whisker is 1. In simulation, an increasingly large force was applied at *a* = 30 mm until the magnitude of the predicted deflection *y*(*a*) differed by 10% between analytic and numerical results. Thicker black (initially straight) and grey (initially curved) lines represent the results of the analytic (dashed) and numerical (solid) solutions. The analytical model does an excellent job of predicting the shape of the whisker up to *a*, but is less accurate beyond the point of contact. **(c)** Accuracy of the analytical model depends on the location of imposed force. An increasingly large force was applied at several points along a tapered, straight whisker (black) and a tapered, curved whisker with unity normalized curvature (gray) until the predicted deflection *y*(*a*) disagreed by 10% between analytic and numerical results. Values on the *y*-axis represent the angle *θ* that is achieved when the 10% threshold is reached. Analytical model clearly performs best when force is applied close to the base. It is also apparent that taper has a moderate affect on the accuracy of the analytic model.

3.3.1.3 Model 1: Deformation of a Tapered Whisker With Inherent Curvature

The simplest way to incorporate curvature into the analytical expression for a straight, tapered whisker (3.4) is to sum the inherently-curved shape of the real undeflected whisker with the deflection of a straight, tapered cantilever beam. Our first model performed this summation according the method depicted in Figure 3.2.

To validate the assumptions implicit in the summation, we used numerical simulations to calculate the deflections of an inherently curved whisker through large angles (see Appendix D). Before we could compare the analytical results of Model 1 and the results of the numerical simulations, however, we noted one additional complexity, as follows: if the whisker is initially straight and deforms only through small angles, the arc length a (the distance as measured along the length of the whisker) differs negligibly from the straight distance from whisker base to point a out along the whisker. This was discussed previously in the Methods section. If the whisker is not straight, but instead has an inherent curvature, these two values are different. Thus for the remainder of this paper, it is important to remember that a is always defined as the arc length distance, not the straight distance from base to point of contact distance.

Figure 3.3(b) illustrates the error between deflection profiles found using Model 1 and using numerical simulations. The thin solid lines represent straight (black) and inherently curved (gray) whiskers. The inherently-curved whisker was chosen to have a constant normalized curvature (ratio between the total arc length and the radius of curvature) of 1. This normalized curvature value is similar to the values found for the whiskers used in this study (data not shown). An increasingly large force was applied at $a = 30$ mm for both whiskers until the magnitude of deflection at a, $y(a)$, differed by 10% between the two models. The thick solid and

dashed lines give the deflected shape of the initially straight (black) and curved (grey) whiskers, as found by using Model 1 (dashed) and numerical simulation (solid). It is clear that Model 1 yields an accurate description of the deflected whisker up to the force location a, but is less accurate further out.

Figure 3.3(c) quantifies the amount of angular deflection that results in 10% error between the two models, for a force imposed at any point along the whisker. The inherently-curved whisker again had normalized initial curvature of 1, as described for Figure 3.3(b). The same procedure described for Figure 3.3(b) was repeated for several a values and the resultant deflection angle, θ, at which 10% error was reached for each a value was recorded. Figure 3.3(c) shows the amount of angular deflection plotted against normalized location of the imposed force, a/L, for an inherently straight (black) and curved (gray) whisker. It is apparent from this figure that imposed force location affects the amount of deflection possible before significant error results between Model 1 and the numerical simulations. As the location of imposed force increases, the amount of deflection before the 10% threshold is reached decreases for both the straight and pre-curved whiskers. This relationship is steeper for the inherently-curved whisker, but both cases show that Model 1 is most accurate when forces are applied close to the whisker base.

This analysis has shown that by summing the inherently-curved shape of the real whisker with the deformations calculated from (3.4), experimenters can obtain an approximation of the deflected whisker shape up to point a with $\leq$ 10% error, provided the force is imposed at $a/L <$ 70%.

3.3.2 Part Two: Validating Model 1 Against Experimental Data Obtained From Real Rat Vibrissae

Model 1 incorporates the effects of taper and inherent curvature, and we have shown it to be particularly accurate for forces applied close to the base. We used two different methods to determine how well Model 1 captured the bending characteristics of a real rat whisker. First, we compared force-displacement curves between model and experiment. Second, we used the model to predict the entire shape of deflected whiskers, and compared this prediction with experimentally-obtained shapes of deflected whiskers.

3.3.2.1 Force Displacement Curves: Analytical Equations and Experiment

We experimentally quantified bending for a real rat whisker in response to a force imposed at different distances from the base. Figure 3.4(a) shows three overlaid images of the E2 whisker bending under the same force (121.8 ± 24.5 μN) imposed at a distance of 7, 8, and 11 mm horizontally from the base. Note that although during experiments the stimulator was positioned at horizontal distances, during all analysis the horizontal distance was converted to arc length.
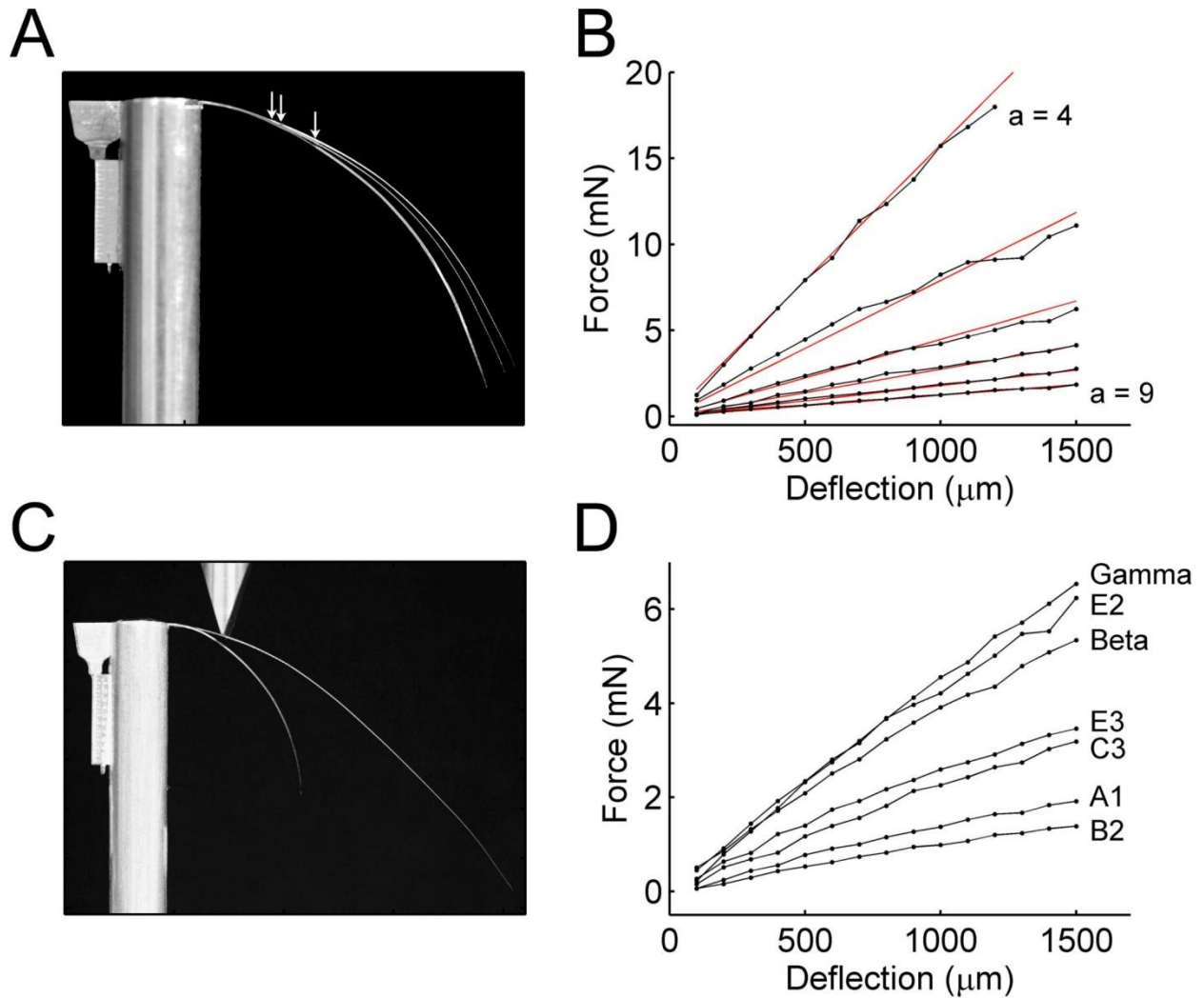
Figure 3.4: Matching force-displacement curves between theory and experiment. **(a)** Superimposed images of the E2 whisker, bending as a force F = 121.8 ± 24.5 μN is imposed at three different locations (arrows). **(b)** Relation between deflection and the force needed to cause that deflection is approximately linear for any given point where force is imposed. Solid red lines represent the expected force-deflection relationship derived from Model 1 using a Young's modulus of 2.6 GPa, whereas black dotted lines represent experimental data where deflections were imposed at evenly spaced horizontal distances from the base (4-9 mm). **(c)** Shorter whiskers deflect more than longer whiskers when the same load is applied. Bending of whiskers C3 (short whisker) and Beta (long whisker) is shown here. **(d)** Whiskers have unique geometrical dimensions, which result in different force-deflection relationships. Each whisker was tested with the force imposed 6 mm horizontally from the base.

Figure 3.4(a) clearly shows that when a force is imposed further away from the base, the whisker deflects more. This effect is quantified in Figure 3.4(b), in which forces are imposed at different distances (4, 5, 6, 7, 8, and 9 mm horizontally from the base of the E2 whisker). The solid red lines are the theoretical force-deflection relationship predicted from (3.4). The black lines indicate experimental data. In (3.4) we used the measured diameter (232 μm) to calculate I = 1.42 x 10^{-16} m^4. The measured length of the whisker was 48.0 mm, and a good fit for E was found to be 2.6 GPa. For these values of E and I, an excellent match was found between (3.4) and experiment.

Figure 3.4(c) shows superimposed images of the C3 and β whiskers as they were deflected by approximately the same force (840.3 ± 94 μN) imposed at a horizontal distance of 8 mm. It is clear that the force has a larger effect on the C3 whisker (D_{base}= 119 μm, L = 21.50 mm) than on the β whisker (D_{base} = 225 μm, L = 66.20 mm). Figure 3.4(d) quantifies this effect for seven different whiskers of varying size. In this experiment, whiskers β and γ are the longest whiskers, with lengths of 66.2 and 60.3 mm, respectively, while E2 and β are the thickest at the base, with base diameters of 232 and 225 μm, respectively. The last four whiskers are all shorter and thinner at the base than β, γ, or E2, and therefore require less force to deflect the same amount.

Notably, Figure 3.4(b,d) illustrates that at a given horizontal distance away from the base (6 mm in this case) the force-displacement curve follows a linear relationship for each whisker. This relationship can be seen explicitly in (3.4). Importantly, this does not mean that for a given force F the whisker will bend linearly along its length, because the proportionality constant between F and $y(x)$ is different at each point x.

3.3.2.2 Capturing the Complete Shape of a Whisker: Model 1 Compared to Experiment

The force-displacement curves in Figure 3.4 demonstrated a good match between (3.4) and experiment for discrete values of force and displacement. They also serve to quantify the effects of whisker size (base diameter and length) and force location on whisker deflection. However, the curves of Figure 3.4 only quantify the relation between force and displacement at point a, where the force is applied. How well can Model 1 as described in Part 1 characterize the entire shape of the whisker when it contacts an object, purely as a function of whisker length, diameter, and object distance a? To answer this question, Model 1 was used to predict the deflection of the whisker everywhere along its length (i.e., at all values of x). These modeling results were then compared with the photographed shape of the whisker (Figure 3.1(a)). Because Figure 3.3(c) shows that the model should remain accurate for relatively large deflections close to the base, it would be surprising if model and experiment were not in good agreement.

We used Model 1 to calculate the full shape of the whisker as a function of x analytically while leaving Young's modulus (E) as a free parameter. Experimentally, we took digital photographs to obtain the entire shape of each whisker as it was increasingly deflected by the stimulator. We imported the photographed shape into MATLAB and superimposed the modeling result. The value of E was varied in the model until the best match was found between model and experiment. If E was too large, the model did not deflect enough compared to the experimentally-deflected whisker, and if E was too small, the model whisker deflected too much.

The inset of Figure 3.5 illustrates the quantities used to find the best match between model and experiment. The error between the model and the experimental data was found by taking the ratio of the areas between the model and the deflected whisker (area 2) and the area between the

deflected whisker and the undeflected whisker (area 1 + area 2). All areas were calculated from the whisker base to the point of contact, *a*. Normalization to the area between the undeflected whisker and the deflected whisker accounted for any error induced by apparent changes in length due to the small angle approximation, and permitted comparisons of error estimates across whiskers of different lengths. This ratio is referred to as the percent area error, plotted on the *y*-axis of Figure 3.5.
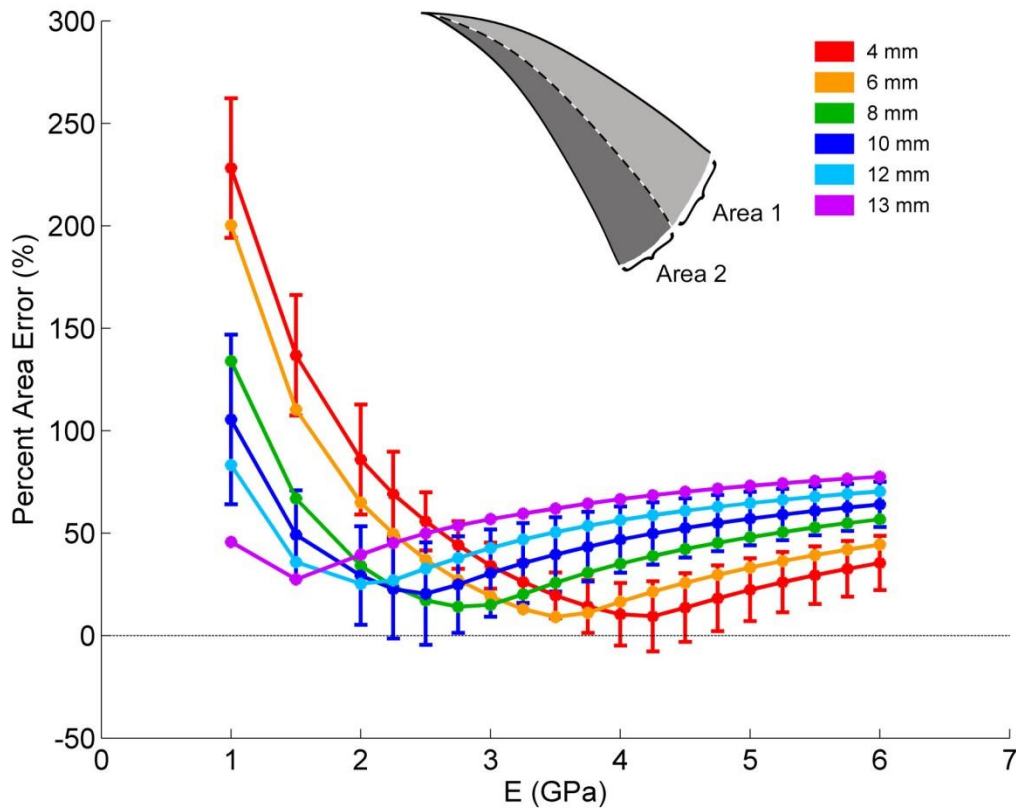
Figure 3.5: Model 1 accurately captures the shape of the entire whisker during deformation. The inset depicts how the error between model and experiment was calculated. The top solid line represents the undeflected whisker, the center dotted line is the model of the deflected whisker, and the bottom solid line is the shape deflected whisker as measured experimentally. Area 1 represents the difference between the modeled deflected whisker and the undeflected whisker. Area 2 represents the difference between the modeled deflected whisker and the experimental data. The "percent area error" was defined as the ratio of area 2 to the sum of areas 1 and 2. This measure normalized the error over different whisker lengths and stimulator placements. The plot shows the percent area error between model and experiment for changing values of Young's Modulus for the A1 whisker. Each trace represents the average of the percent error over 15 vertical displacements at a single horizontal distance from the whisker base as indicated in the legend. Best fits were obtained with values of Young's modulus that ranged between 1.5 and 4.25 GPa, with an average E = 2.75 GPa. For visual clarity, standard deviations are shown on only 2 traces (blue and red) displaying the largest and smallest error ranges.

Seven whiskers (A1, B2, β, C3, E2, E3, γ) were used in the analysis of the complete whisker shape. For each whisker, we averaged over all vertical deflections at each horizontal distance from the base. This amounted to ~110 comparisons between experiment and model, >20 values of Young's modulus, for a total of ~ 2200 comparisons per whisker.

Figure 3.5 illustrates the results for the A1 whisker. Plotting error as a function of Young's modulus (E) illustrates that:

1) The smallest error (2.72% for the A1 whisker) is found when the object is closest to the base of the whisker.

2) Estimated E for the A1 whisker has a range of ~1.5 to 4.3 GPa, with an average of 2.75 GPa, consistent with the value found for Figure 3.4(b) and with previous estimates [28, 29].

3) The value of the "best" E decreases as the object moves further from the base. These results were representative of those for all of the whiskers. A1 does not represent a "best case."

The ranges for E of the other whiskers were mostly similar to that of A1. Table 3.1 shows geometrical dimensions and average values of E for all seven whiskers. Results for the C3 whisker lay outside the range of results for the other whiskers. For C3, Young's modulus ranged from 4 to 9.5 GPa and had an average value of 6.25 GPa. The C3 whisker was by far the shortest and thinnest of the whiskers and deflections were imposed up to ~50% along the whisker length. Most other whiskers only had deflections imposed up to ~35% along the length of the whisker. This could help explain the large value of Young's modulus found for the C3 whisker.

Table 3.1: Geometrical whisker dimensions and calculated values for average Young's modulus.

Whisker Name	Arc Length (mm)	Base Diameter (μm)	Average E (GPa)
β	66.2	225	1.40
γ	60.3	199	3.75
A1	51.7	160	2.75
E2	48.1	232	1.90
B2	41.1	169	2.30
E3	33.3	189	3.90
C3	21.5	119	6.25

3.3.3 Part Three: A Biomechanical Model for Extracting Radial Object Distance Using Information About Moment

3.3.3.1 Model 2: An Analytical Expression for Radial Object Distance as a Function of Moment at the Whisker Base.

Equation (3.4) describes a relationship between the deflection, $y(x)$, at each point, x, along a tapered whisker and the arc length, a. The value of $y(x)$ is related to a through the force F imposed at point a, the bending stiffness represented by the product EI_{base}, and the total arc length, L, of the whisker. We asked whether the rat could use the relationship expressed in (3.4) to infer information about radial object distance, d, from the whisker base to the point. Note that radial distance, d, is shorter than arc length distance, a. However, assuming a straight whisker and evaluating (3.4) at d yields:

$$y(d) = \frac{FLd^3}{3EI_{base}(L-d)} \tag{3.5}$$

Using $M = d \times F$ and $\theta = y(d)/d$ (assuming small angle deflections) yields

$$M = C\theta\left(\frac{1}{d} - \frac{1}{L_{\mathrm{BT}}}\right) \tag{3.6}$$

where $C = 3E\dfrac{\pi r_{\mathrm{base}}^4}{4} \equiv 3EI_{\mathrm{base}}$ and L_{BT} is the linear base-to-tip length of the whisker. Note that L was replaced with L_{BT} to enforce the boundary condition that $M = 0$ when $d = L_{\mathrm{BT}}$. Solving for the variable d, and taking time derivatives yields

$$d = \frac{C\dot{\theta}L_{\mathrm{BT}}}{C\dot{\theta} + \dot{M}L_{\mathrm{BT}}} \tag{3.7}$$

Equation (3.7) represents our second analytical model (Model 2). It relates radial object distance to change in moment at the whisker base.

Note that (3.7) is expressed in terms of time derivatives. These time derivatives are included primarily for biological plausibility. Recall that θ represents the angle that the whisker has rotated since the time of initial contact with the object. M is the moment experienced at the base, which increases as the whisker rotates against the object. In an engineered system, it is easy to set $\theta = 0$ at the angle of initial contact, and then to keep track of its increasing value. In principle, just like the engineered system, the rat could use the absolute position of the whisker (θ) combined with an absolute measurement of moment to determine object distance. However, given the well-known inability of the nervous system to accurately measure absolute quantities, but its exquisite sensitivity to rates of change, we think it most probable that the rat would use the time derivatives as represented in (3.7).

If the whisker moves at constant velocity, then derivatives of moment with respect to θ and with respect to time are proportional. If, in contrast, the whisker moves at non-constant velocity, then the rat could keep track of how moment is changing relative to θ. Thus most generally, radial distance can be computed as:

$$d = \frac{CL_{\mathrm{BT}}}{C + (\mathrm{d}M / \mathrm{d}\theta)L_{\mathrm{BT}}} \tag{3.8}$$

The fact that the computation can be performed at every instant in time – and for varying whisking velocities – is a key advantage of the proposed mechanism for determining object distance. It seems likely that a particularly good time for the rat to choose would be immediately following contact up until the point in time when the linearization breaks down. For example, a constant protraction velocity of 400°/second would allow ~2° degrees of rotation in the 5 ms after object contact, well within the linear range. It should be noted that the rat will have much less time to compute object distance if contact occurs close to the tip, as the whisker will quickly fold in on itself and/or flick past the object for small θ, and $\dot{M}$ will change accordingly.

Equations (3.7) and (3.8) demonstrate that if the rat can keep track of the rate of change of moment and the velocity with which it is "pushing" its whisker against the object, then enough information will be present to infer object distance. Taken with the results of previous studies that have described mechanisms for encoding horizontal and vertical position [35-37], these equations effectively demonstrate that only three mechanical variables are required to extract all 3-D spatial information about objects. Those variables are: angular position, angular velocity, and rate of change of moment (or curvature). In addition to these three variables, we posit that

the rat is sensitive to a fourth variable – moment – so as to remain sensitive to static deflections of its whiskers.

3.3.3.2 Predicted Changes in Moment at the Whisker Base as the Whisker Rotates Against an Object

We now use Model 2 (3.7) to compute the predicted changes in moment at the whisker base as the whisker is rotated against an object. Figure 3.6(a) plots the rate of change of moment at the base of the whisker as a function of contact distance for two different whisking velocities. To highlight the effects of taper (see Appendix C), results for the cylindrical whisker are also shown (gray traces). For both tapered and cylindrical whiskers, the steepest change of $\dot{M}$ is for $d\,/\,L_{BT} \leq 0.3$, when the imposed force is closer to the vibrissal base. It is clear that $\dot{M}$ goes to infinity for positions very close to the base. In addition, $\dot{M}$ goes to zero at the tip of the tapered whisker, meaning that almost no moment is transmitted back to the base when contact is made very near the tip. Instead, the whisker tip might locally deflect and subsequently drag along the object. This suggests that the region near the whisker tip may be more sensitive to low-amplitude, high-frequency signals, because these small signals can be amplified by resonance [22], while the remainder of the whisker may be more sensitive to high-amplitude, low-frequency signals. This in turn implies that the tip of the whisker may transmit more vibration and texture information while the middle region and base could simultaneously be used to extract shape and position information.
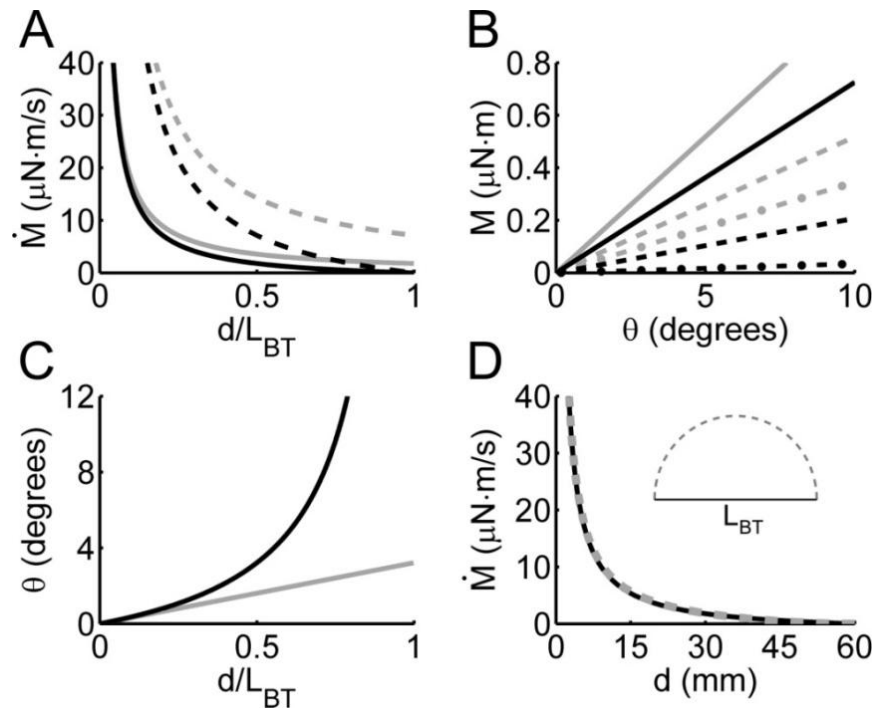
Figure 3.6: Model 2 provides relationships between rate of change of moment, $\dot{M}$, moment, M, deflection angle, θ, and radial object distance, d. All simulations modeled whiskers with a Young's modulus of 3.5 GPa, a base radius of 60 μm and a length of 6 cm. **(a)** Rate of change of moment versus normalized contact distance for conical and cylindrical whiskers rotating at different velocities. Black curves represent the relationship for a tapered whisker, while the gray curves are for a cylindrical whisker. Solid lines: velocity = 1 rad/s; Dashed lines: velocity = 4 rad/s. Rates of moment change for both whisker shapes rapidly approach infinity for $d/L_{BT} \leq 0.3$. **(b)** Moment as a function of whisker angle since contact with the object. Solid curves are for an object distance of 0.3 L_{BT}, the dashed curves for an object distance of 0.6 L_{BT}, and the dash-dotted curves for an object distance of 0.9 L_{BT}. The black curve models a tapered whisker, and the gray curve models a cylindrical whisker. **(c)** Whisker deflection as a function of normalized contact distance with an imposed 0.1 μN-m moment (the whisker rotated against the object until 0.1 μN-m was reached). **(d)** Inherent whisker curvature has a negligible effect on rate of change of moment $\dot{M}$. This graph plots $\dot{M}$ at the whisker base as the whisker is rotated against a point-object placed at different radial distances, d, out along the whisker. Solid black line indicates the initial rate of moment change for a tapered, straight whisker (Model 2). Dashed gray line indicates initial rate of moment change for a tapered whisker with an inherent curvature equal to that of a semi-circle (inset) found from numerical simulation. The two curves are virtually indistinguishable. Semi-circle inherent curvature is an extreme case and is much larger than that of any real rat whisker.

Figure 3.6(a) also shows that the magnitude of $\dot{M}$ is larger when the angular velocity $\dot{\theta}$ is larger. This is an intuitive result, but the figure makes clear that the rat can obtain the same value of $\dot{M}$ at the whisker base either by increase whisking speed or by moving its snout closer to the object. This may suggest the existence of a "sweet spot" or "sweet combination" of object distance and whisking velocity. This location on the whisker would be constrained by the following criteria:

- If the snout is too close to the object, moment may become so large that receptors in the follicle may saturate, or the "motor" (i.e. the sling muscles) could max out and the whisker may barely even bend.

- If the snout is too far away from the object, the moment transmitted to the base may be below the rat's detection threshold, or differences in moment may be difficult to resolve. Also, if contact occurs very close to the tip, the whisker will quickly fold in on itself and subsequently either flick past the object or drag along it.

- Different velocities will scale the curve in Figure 3.6(a). Faster velocities mean that better resolution will be obtained for objects further away.

Figure 3.6(b) plots the moment at the base of the whisker as a function of whisker angle, θ. As mentioned earlier, θ is the angle subtended since initial contact with the object, and is interchangeable with time on the x-axis as long as $\dot{\theta}$ is constant. Each curve in Figure 3.6(b) represents a different object distance ($0.3L_{BT}$, $0.6L_{BT}$, and $0.9L_{BT}$). It is critical to understand that the linear relationship between M and θ does not mean that the whisker will bend linearly along its length. The proportionality constant between $M(x)$ and $y(x)$ is different at each point x along

the whisker. In addition, imposing a force at position $2x$ does not make the whisker bend twice as much as if the force were imposed at position x. This can be seen in the uneven spacing of the lines for $0.3L_{BT}$, $0.6L_{BT}$, and $0.9L_{BT}$ in Figure 3.6(b).

3.3.3.3 Predicted Changes in Curvature at the Whisker Base as the Whisker Rotates Against an Object

It is clear from (3.1) that curvature and moment are directly proportional. The change in curvature at any point along a beam is equal to moment divided by the whisker bending stiffness, EI. Figure 3.6(c) plots the angular position of the whisker, θ, as a function of normalized contact distance d / L_{BT}, for an imposed 0.1 μN-m moment. Simply put, this plot predicts how much the whisker will bend if the whisker is being actuated by a maximum moment of 0.1 μN-m. For a cylindrical beam, the relationship is purely linear. For a tapered beam, much less moment is required for the whisker to deflect past a distal object compared to a more proximal one.

3.3.3.4 Effects of Inherent Whisker Curvature on Moment Sensed at the Base

Finally, we now show that Model 2 holds for all realistic values of whisker curvature (and even much larger curvatures). A mechanical rule of thumb states that if the radius of curvature of a beam is ≥10 times its maximum cross-sectional height, many fundamental principles of deformation analysis remain valid [34]. Geometrical analysis showed that the real rat whiskers used in this study exhibited a maximum curvature of 1.7 (units normalized to whisker arc length) along their length. A typical ratio of the radius of curvature to depth was ~250. The minimum

ratio found along any whisker was ~100. Since the minimum value is ≫10, fundamental elasticity equations apply.

Numerical simulations were used to compare changes in $\dot{M}$ profiles for a straight whisker and for a whisker with a large inherent curvature. To be conservative, we modeled the deformation of a whisker bent into the extreme shape of a semi-circle, which has a constant normalized curvature of $\pi \approx 3.14$. This is roughly twice the maximal curvature found for any of the real whiskers. Base-to-tip length for both models was 60 mm. Figure 3.6(d) illustrates the results of the simulation: the $\dot{M}$ profiles for the straight and inherently curved whiskers overlap almost exactly. The inherent curvature has negligible effect on the moment that will be sensed at the whisker base.

3.3.3.5 The Effects of Whisker or Head Translations Compared to Whisker Rotations

As established by earlier studies [36, 38], and as schematized in Figure 3.7(a), cylindrical coordinates are the most natural system to describe whisking movements of the rat. θ describes the rostral-caudal angle, z is the height of the whisker row, and r is the radial distance out along the whisker. This coordinate system is particularly suited to describe the rotational movements that most typically characterize whisking behavior.
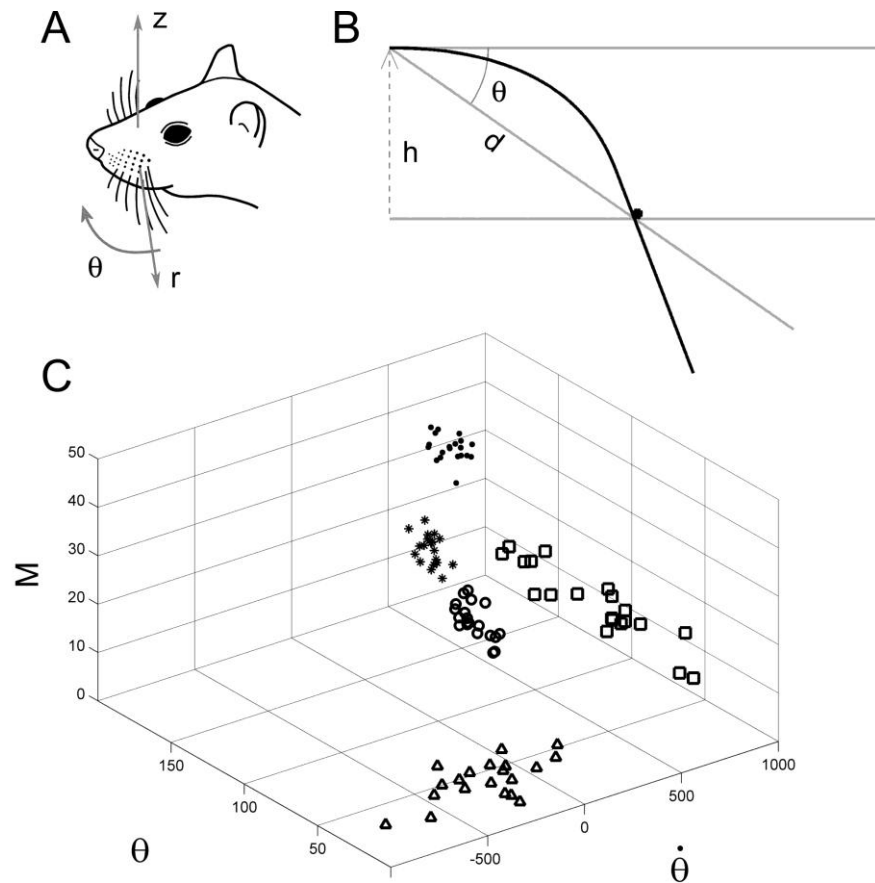
Figure 3.7: Neural encoding of primary mechanical variables during translation and rotation. **(a)** Cylindrical coordinates are the most natural system in which to describe whisking movements of the rat. **(b)** The whisker deflection model presented in this paper can be used to describe deflections due to translation as well as rotation. A straight, undeflected whisker is represented by the solid horizontal and slanted lines. The whisker either rotates *θ* degrees, or translates a distance *h*. Deflection by an object (black dot) at a radial distance, *d*, will eventually result in identical deflection profiles (black trace). **(c)** Proposed representation for three of the four mechanical variables found to be important in the current study. The axes of the graph are angular position, angular velocity, and moment at the base of the whisker. Neural responses of Vg cells could be quantified by placing them within the state-space defined by these axes. In this schematic, each symbol represents the spike of a ganglion neuron responsive to a particular combination of parameters. The magnitude of the neural response is represented by the number of data points (spike count), and the variability in the response is represented by the 3-dimensional breadth of the distribution. The triangles, for example, depict a cell sensitive to a particular combination of angular position (near 40⁰) and velocity (between -800 and 250⁰/sec), but not responsive to moment. The square symbols lie in the velocity-moment plane, and represent a cell that responds roughly independent of position, but only to a particular combination of velocity and moment.

Sometimes, however, rats' exploratory behaviors involve translational movements of the head instead of rotations of the whiskers. For example, a recent study demonstrated that rats were able to discriminate the width of an aperture to within millimeter resolution using a translational "nose poke" through the aperture [30]. Rats were able to perform this task at above chance levels even when only one whisker remained on each side of the face. The authors did not propose an encoding mechanism for distance detection, but noted that whiskers were "deflected rearward" as the rats entered the aperture.

Figure 3.7(b) illustrates that the model presented in the current paper holds equally well for translation and rotation, and can explain the results of the earlier study by [30]. The model thus applies to earlier studies that involve small-angle passive displacements of the whiskers in anesthetized rats (e.g., [39-42]). With knowledge of whisker length and base diameter, approximate Young's modulus (3-4 GPa), the location of the imposed stimulus and its magnitude (which could take the form of a force, rotation or linear deflection), experimenters can now calculate approximately how much moment is experienced at the base of the whisker during passive displacement experiments. As will be shown in the Discussion section, however, this may not be a very useful calculation to perform for passive displacement experiments.

The variables that the present study has found to be important for shape extraction are angular position, angular velocity, moment (or equivalently, curvature), and rate of change of moment. This mechanical analysis suggests that a state-encoding scheme [43-45] is a parsimonious and quantitatively rigorous way to represent the responses of Vg neurons. Figure 3.7(c) illustrates an example of a state-encoding scheme using three of the four mechanical variables. Neurons have a certain probability of firing a spike when the whisker is in a particular

"state." A state is uniquely defined by whisker position, velocity, moment, and moment-dot; in the example of Figure 3.7(c) only three of the four variables are included. If necessary, velocity could be defined to have two dimensions (rostral-caudal and dorsal-ventral) to account for the directional sensitivity of the cells of velocity information [46]. This would result in a higher dimensional space but would otherwise leave the state-encoding representation unchanged.

3.4 Discussion

3.4.1 Technical Considerations

3.4.1.1 Why Develop an Analytical Model?

The present study has developed a simple, analytical model of a rat vibrissa that accounts for vibrissal curvature as well as taper. The model is well matched by experimental results (Figures 3.4 and 3.5). The advantage of an analytical model over the numerical method also presented in this paper is that it can be solved quickly and exactly, without use of a computer, to obtain a very close approximation to how a real whisker will bend. This is potentially useful to all investigators performing experiments in which the whiskers are deflected by an amount within the confines defined by Figure 3.3(c). Analytic models also make explicit the dependence of whisker bending properties on mechanical variables. Numerical simulations are required to precisely quantify bending of the whiskers in other cases. It is important to note that the change in curvature and the change in moment at every point along the whisker length are directly proportional, related through the whisker bending stiffness EI.

3.4.1.2 Young's Modulus and Whisker Stiffness

Young's modulus (E) for biological materials is an approximation at best. The present study finds E approximately equal to 3-6 GPa, in line with previous estimates [28, 29, 47]. A puzzling result of the present experiments is that the value for E seemed to decrease as forces were imposed further from the whisker base (Figure 3.5). There are at least four possible explanations for this result. First, the result could be taken at face value. The whisker material may vary with length in such a way as to result in lower E values further from the whisker base. Second, it is possible that the equivalent stiffness of the whisker decreases with whisker length. For example, if the whisker tapered parabolically instead of linearly, then the smaller cross sectional area as a function of length would result in an apparently lower E value. Third, Figure 3.3(c) demonstrates that the accuracy of the tapered-beam model decreases as the force is imposed further from the base. It is therefore possible that the decreased accuracy of Model 1 is directly responsible for the apparent change in Young's modulus. This is consistent with the increase in error associated with the "best fit" Young's modulus as deflections were imposed at increasing radial distances. Fourth, friction would have the largest effect on the most curved (shortest) whisker, thereby increasing the apparent value for E.

3.4.1.3 The Importance of Moment

Almost all previous studies of the vibrissae have focused exclusively on kinematic variables, that is, angular position and its time derivatives. These variables are termed kinematic because they describe the motion of a body without consideration to the forces or moments that affect the motion. During active whisking, however, kinematic variables alone cannot provide a

complete representation of all the information transmitted to the rat through its whiskers. Under active whisking conditions, the whisker could well be at the same angular position and yet experience very different moments at the base. Figure 3.8 illustrates some of the differences between active and passive whisker displacements. The models presented in the current study begin to consider the potentially important role that moment may play in conveying meaningful information to the rat.
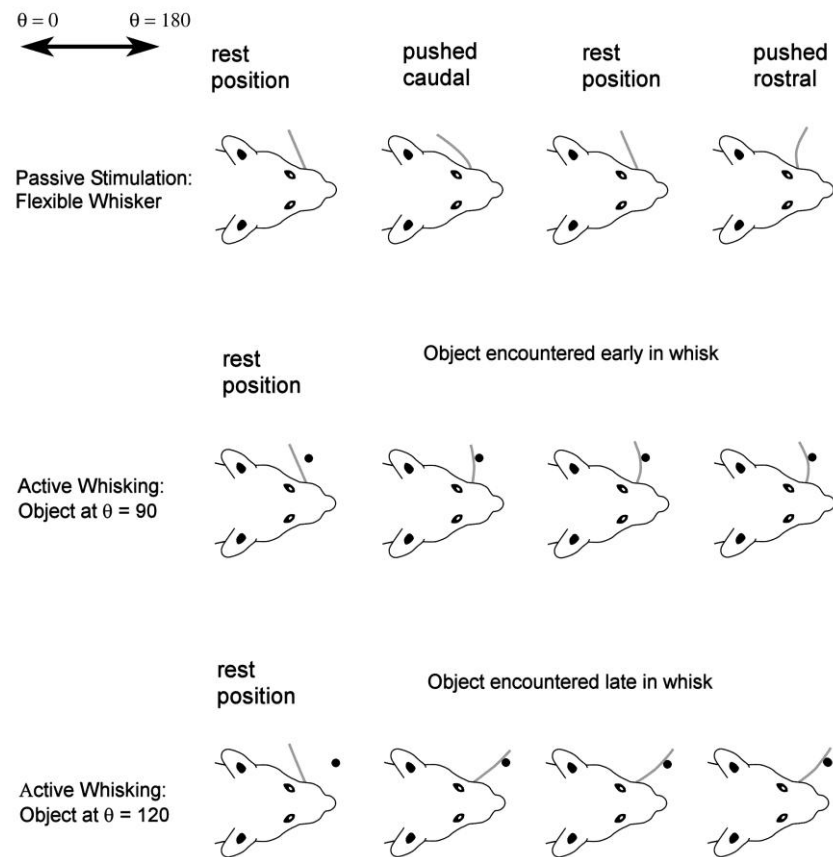
Figure 3.8: Passive displacement experiments **(top row)** force a direct relationship between angular position and moment. In active whisking experiments **(bottom two rows)** the moment changes at the base as the whisker deflects into an object placed at different angular positions.

For completeness, we note that both of the present models would be considered "quasi-static," because they assume that the movement of the whisker can be approximated so that at every point in time it is essentially at equilibrium. Assumptions for a quasi-static model require that all forces and moments are conservative and that the whisker has two physical constraints: the rigid connection at its base and at the contact point with the object. A fully dynamic (not quasi-static) treatment of the whisker would have to incorporate mass and inertial quantities and collision forces that may result in "whip."

3.4.1.4 The Relative Importance of Whisker Diameter, Length, Curvature, and Taper

All equations in the current paper indicate that moment at the whisker base will depend on the base diameter of the whisker raised to the fourth power. Thus whisker diameter will have the largest influence of any single variable on the moment experienced at the whisker base. There is more tolerance for small deviations in whisker length. The inherent curvature of the whisker plays a relatively small role in determining how the deflected whisker will change shape, while in contrast, the taper of the whisker greatly affects how the whisker will bend and the moment transmitted to the base.

3.4.2 The Models are Highly Applicable to Natural Whisking Behaviors

Throughout the Methods and Results sections, we have been careful to emphasize the assumptions embedded in the models, and the limitations that these assumptions impose. This careful exposition of modeling constraints may leave the impression that the models apply only

under very limited conditions. It is therefore important to emphasize that our analysis is in fact very general, and that versions of the models will hold even for very complex behaviors.

3.4.2.1 The Models Can Apply to a Wide Range of Boundary Conditions: The Importance of Instantaneous Measurement

Moment at the whisker base will vary depending on how stiffly or loosely the whisker is held in the follicle, that is, on the boundary conditions in and near the follicle. The rat could presumably change follicular boundary conditions through muscular activation as well as by modulating blood flow to the follicular sinus [48]. The models of the current paper are based on clamped boundary conditions at the whisker base, but more realistic, tissue-like conditions might be modeled with a spring-mounted or a torsional-spring-mounted whisker. It is critical to note, however, that the fundamental results of the present paper will not change, even if boundary conditions are very different from the clamped condition modeled here. This is because the relationship between moment at the base and radial object distance will remain monotonic regardless of boundary conditions. As long as the rat can learn the monotonic function that relates these variables (M and d), the method proposed here will work for radial distance extraction.

What happens if the rat changes the boundary conditions at the whisker base during the course of a whisk? Equations (3.7) and (3.8) demonstrate that the rat can determine radial object distance based on the instantaneous rate of change of moment. This means that the rat need only sense distance at a single instant during the whisk, and it does not matter if boundary conditions change before or after that instant. Recent behavioral data from Prescott and colleagues ([49])

have shown that rats often use an exploratory strategy of "minimum impingement," in which they tap, rather than sweep, their whiskers over objects. This suggests that the rat gains a sense of radial object distance in the first few milliseconds immediately following object contact. This strategy is consistent with the one determined to be most effective for radial distance extraction in a hardware model of the whiskers [47], and also helps avoid measurement complications due to whisker slip along the object. Finally, we note that regardless of boundary conditions, the amount that the moment will change in a given time interval is directly related to the whisking velocity. We therefore suggest that variations in velocity over the trajectory of the whisk may be of particular behavioral importance to the rat during tasks that require estimates of object distance.

3.4.2.2 The Models Can Apply to a Wide Range of Angular Displacements, Velocities, and Distances to Object Contact

Numerous papers have demonstrated that naturalistic rat behaviors employ a large range of angular positions, velocities, and distances to object contact [4, 5, 21-24]. It might therefore be asked how the values for these variables presented here fit into these ranges. For example, over what range of angles, whisking amplitudes, and velocities, do the proposed models apply? The short answer is that the fundamental results of the models hold over virtually all distances to contact except very near the tip, all angular velocities, and all angular displacements. Figure 3.8 illustrates the broad applicability of the models and the differences between passive displacements and active whisking.

The rat-centered coordinate system for Figure 3.8 is defined by θ in the top left corner. A value of $\theta = 0$ means that the whisker is completely retracted, pointed directly backwards towards the tail of the rat. A value of $\theta = 180°$ means that the whisker is completely protracted, pointed directly forward towards the snout of the rat. The first row of Figure 3.8 illustrates passive deflection assuming that the whisker behaves as a flexible beam. In this case, pushing a point on the whisker backwards or forwards causes the whisker to bend, and generates a moment at the whisker base. Consistent with the models presented in the Results section, this figure assumes that the whisker is held rigidly at the base. Assume that the point on the whisker in contact with the stimulator is pushed to some value of θ, different from the whisker's rest position. Then the amount of whisker bending, and hence the moment generated at the base, depends directly on $\theta - \theta_{rest}$, that is, on the position to which the whisker is pushed. This means that there is no way to "decouple" the absolute angular position of the whisker (as measured at the point of stimulator contact) from the moment generated at the base.

The second and third rows of Figure 3.8 illustrate that active whisking permits decoupling of the values of absolute whisker position θ and the moment generated at the base. In the second row, the whisker is actively protracted forwards, and behaves as a rigid body until it encounters the object at $\theta \approx 90°$. As the whisker is increasingly protracted into the object, the whisker begins to bend, and the moment at the whisker base increases with increased bending. In the third row, the whisker does not encounter an object until $\theta \approx 120°$. Just as before, the whisker bends as it is protracted into the object, and the moment at the whisker base increases with increased bending. The only difference is that the bending is now occurring near $\theta \approx 120°$ instead of $\theta \approx 90°$.

Examination of Figure 3.8 rows two and three clearly shows that the models apply to the whisker encountering an object at any angular position. The models also apply regardless of the whisker's angular velocity. The rate of moment change at the whisker base depends directly on the angular velocity with which the whisker is protracted. By learning the relationship between moment change and angular velocity, the rat can extract radial object distance *d*. The second and third rows of Figure 3.8 also demonstrate that the small angle approximation applies in all cases of initial object contact. When the whisker first makes contact with an object, the initial bending angle is zero. As the whisker presses by the object, the bending angle increases, and the angular deflection to which the model holds up depends on the object's radial distance, as depicted in Figure 3.3(c). As discussed above, we suggest that the rat gains a sense of radial object distance in the first few milliseconds immediately following object contact, exactly when the small angle approximation applies. Importantly, however, the fundamental result of this paper does not depend on small angles. Large bending angles will change the function that relates moment M and the radial distance d, but it will not change the fact that M and d are monotonically related for a given value of θ. Thus as long as the rat can learn this relationship, a variation of the model will apply.

3.4.2.3 The Models can be Adapted to Apply to Multi-Point Contact

The models, experiments, and analysis presented in the present paper have assumed frictionless point contact. This means that forces are assumed to be applied only normal to the vibrissa at the point of contact. But recent studies from several laboratories have shown that rats engage objects and surfaces in complex ways, some of which have a large fraction of the whisker

in contact with an object as it sweeps by. How do the models presented in this paper hold up under conditions of multipoint contact? The answer to this question has four components.

First, the initial contact of a whisker with an object will almost certainly be single-point, before the rest of the whisker has a chance to make contact with the object. As discussed above, we suggest that it is only the first few milliseconds after object contact that the rat needs in order to estimate object distance. Second, any force applied to the whisker can be divided into normal and tangential components. It seems likely that the rat is able to sense these components independently [50], which would then permit not only extraction of radial distance, but also horizontal angle [51]. Third, the principle of superposition states that any load distributed along a beam can be modeled as a resultant force F_R acting at a single point at the beam. This means that moment at the base can be calculated even for multipoint contact, provided that the appropriate location and magnitude F_R can be determined. Determining the magnitude and the location of the resultant force for multipoint contact during natural behaviors will be an interesting future adaptation to the model. Finally, point-contact is standard in passive-stimulation experiments in the anesthetized animal.

3.4.3 Behavioral Implications and Relevance

3.4.3.1 Why do Rats Need to Extract Radial Distance With a Single Whisker at All?

It could be argued that during natural exploratory behavior the rat has use of multiple vibrissae, and thus might not need to figure out radial distance along each whisker. Instead, the rat could compare contact points between whiskers. We can imagine two ways that this

comparison could occur: 1) the rat could either have a sense for the relative lengths of each of its whiskers and compare contact between them, or 2) the rat could "mold" its entire whisker array around an object, and determine object features by the relative moments felt at the base of each whisker. The rat could also combine the two methods.

Let us suppose that the rat has a sense for, or "knows" the relative length of each of its whiskers. If a whisker of length L touched an object, but a whisker of length $L - \Delta L$ did not, the rat could infer that the object was located at a distance between those two values, after accounting for different whisker base locations. There are at least three problems with this technique. First, a recent paper has shown that rats have tactile "hyperacuity;" they can distinguish between differences less than ΔL [52]. Second, it has been shown that rats can make accurate distance judgments with a single whisker remaining on each side of the face [30]. Third, during complex natural behaviors whiskers are very likely to contact objects anywhere along their length, not just at their tips. How can the rat know where this contact has taken place, given that there are no receptors on the whisker itself? The present paper provides a good explanation for how the rat could obtain this information.

Now let us suppose that the rat shapes or "molds" its whisker array around an object. What would it mean, mechanically, for this to occur? It would mean that the whiskers are pushed against the object until the rat is able to sense that the whiskers have touched the object. The only possible mechanical cues that could provide this information are moment and force. No other variable can describe the "push" on the receptors in the follicle. As the whiskers are molded around the object, the rat must then determine where along each whisker's length it has touched the object. This is one key point of the present paper. Finally, we emphasize that we think it

highly unlikely that the rat explicitly determines the absolute radial distance of points on an object. Instead, what the present paper shows is that there is a mechanical variable (moment) that the rat could directly sense that in turn directly correlates with object distance. An ability to accurately measure moment would be greatly useful for sensing 3-dimensional object shape, as rats are known to do.

3.4.3.2 Behavioral Consequences of Curvature and Taper

An intriguing result of the present study is that the inherent curvature of the whisker plays a relatively small role in determining deflected whisker shape for a given force and force location (Figure 3.3(c)). Furthermore, the initial rate of change of moment sensed at the base is not affected by inherent whisker curvature, regardless of where along its length the whisker hits an object. This suggests that the curvature of the whisker may serve some other behavioral function, such as maximizing the sensory volume searched during whisking. In contrast, the taper of the whisker plays a substantial role in determining the way the whisker will bend and the moment that will ultimately be transmitted to the whisker base (see Appendix C). For a particular force imposed at a given distance out along the whisker, the tapered whisker will bend substantially further, yet transmit the same moment to the base as a cylindrical whisker of the same base diameter. The biomechanics thus ensure that large deflection amplitudes of the distal parts of the whisker are required in order to transmit a moment to the base. This makes sense behaviorally, as the most distal parts of the whiskers are often deflected through very large amplitudes as they brush past an object.

3.4.3.3 Complementarity of Vibrations and Bending

Does whisker taper make the whisker "more sensitive" or "less sensitive" near the tip? The answer depends on the definition of "sensitive." The taper makes the whisker bend more for the same imposed force (more sensitive), but it reduces the moment ultimately transmitted to the base (less sensitive). This suggests that object contact near the tip will tend to cause the whisker to abruptly bend in on itself (or otherwise flick past), and therefore implies that the tip would be useful if vibrations were amplified during resonance [22, 28, 29]. This in turn suggests that differential extraction of texture and shape may occur at different locations along the whisker as well as within two different frequency regimes. The two types of information could be simultaneously extracted in the same whisking motion: vibrations can be superimposed on the overall deflection of the whisker.

3.4.3.4 Do Rats "Tap" or "Sweep" Their Whiskers?

The present study has shown that radial object distance can be determined by examining how moment at the whisker base changes with angular position θ as the whisker is increasingly deflected into an object. Although outside the scope of the current paper, it is also possible to show that local object curvature can be determined by looking at the second derivative of moment with respect to time as the whisker is increasingly deflected into an object. If rats "tap" their whiskers against an object, they would be able to build up a representation of the object point by point. If rats "sweep" their whiskers against an object, they would be able to make use of local curvature information in determining object shape as well as texture. Combining these two strategies might help maximize the sensory information acquired. Behavioral studies to

investigate these two potential exploratory strategies are currently underway. Data from Mitchinson *et al.* (2007) suggest that tapping tends to be the preferred strategy [49].

3.4.4 Physiological Correlates and Implications for Higher-Order Neural Processing

3.4.4.1 Responses of Trigeminal Ganglion Neurons

In a recent study, Szwed *et al.* (2006) recorded from Vg neurons while stimulating the facial motor nerve to rotate whiskers into objects placed at varying radial distances [36]. Their results showed that a subset of Vg neurons (called "touch" cells) encode radial distance primarily by increases in firing rate. The present study offers a clear biomechanical explanation for these recent physiological results.

For example, Figure 2(c,d) in Szwed *et al.* (2006) illustrates that touch cells increase their firing rate as the object is placed closer to the whisker base. This is exactly what would be expected from Figure 3.6(a) of the present study, if the Vg neurons were responding to rate of change of moment (Szwed *et al.*, Figure 2(c)), and to moment (Szwed *et al.*, Figure 2(d)). Figure 4 of Szwed *et al.* illustrates that higher velocities at the instant of object contact also increase the firing rate of Vg neurons. This result is also predicted by the data in Figure 3.6(a) of the present study. Faster velocities scale the relationship between moment and radial object distance (compare solid and dashed lines). This makes good intuitive sense, as the rate of change of moment will be larger if the whisker is pushed faster past the object. Thus the present study strongly suggests that the touch-sensitive Vg neurons found by Szwed *et al.* are responding to the moment and rate of change of moment at the whisker base.

3.4.4.2 State Encoding

Responses of Vg neurons have been classified according to two schemes. The first method divides Vg neurons into rapidly-adapting (RA) and slowly-adapting (SA) cells [39, 40, 42]. It has recently been shown that the RA and SA properties of Vg cells are modulated by the direction of movement [46]. The second method classifies Vg responses by their activity during active touch. Neurons are described as "whisking," "touch," and "whisking-touch" cells [36, 38].

The present study has shown that whisker angular position, angular velocity, moment, and the time derivative of moment provide all information to completely describe the 3-D coordinates of any object, as well as static deflection information. This mechanical representation most naturally lends itself to a state-encoding scheme in which these variables form the axes of a state-space. The activity of a neuron can be represented by placing a data point at the correct place in the state space every time that neuron fires. The responses of RA and SA cells, as well as "whisking," "touch," and "whisking-touch" cells would then form trajectories through the space. In no way do we intend to suggest that Vg neurons cleanly encode any mechanical parameters, or that the Vg is in any way "imposing" state-encoding on the incoming data. Vg neurons merely respond to highly nonlinear signals from mechanoreceptors in the follicle. The state-encoding scheme illustrated in Figure 3.7(c) is intended as a conceptual tool for grappling with the real-world complexity of Vg neuron responses.

We suggest that the scheme proposed in Figure 3.7(c) will be particularly useful for precisely quantifying the spatiotemporal patterns of activity across the whisker array resulting from different behaviors. State encoding inherently permits a spectrum of response types, and

allows us to examine how the Vg neurons "cover" the relevant behavioral space of the rat. This may ultimately allow us to make strong predictions for coding strategies in the trigeminal nuclei.

3.4.4.3 Computations of Gradients of Distance and Curvature at Higher Stages of the Nervous System

It is well known that the rat often combines whisking behavior with small, periodic head movements that tend to be temporally synchronized with whisking [3, 4, 7]. These head movements seem to allow the rat to obtain multiple, overlapping samples of the object. If, as we suggest, information about moment is encoded in trigeminal ganglion responses, then how might it be subsequently processed in the trigeminal nuclei? We propose that during object exploration, the trigeminal nuclei are used to compute gradients of object distance and gradients of object curvature, as follows: 1) Within a single whisk, ganglion neurons provide information about the radial distance at which each whisker has contacted an object. The trigeminal nuclei could then compute the local curvature of the object by calculating gradients of these distances. 2) Across whisks, head movements permit the rat to compare overlapping whisked samples of the object. The trigeminal nuclei could then compute gradients of local object curvatures to reconstruct the entire object shape. A very similar strategy may be used by humans as they perform exploratory hand movements that enclose objects and follow object contours [53].

3.4.4.4 What Type of Learning is Required of the Rat, Were it to Calculate Radial Distance According to the Model Proposed Here?

Equation (3.8) relates moment at the whisker base to object distance through the parameters C and L_{BT}. This in turn suggests that the rat would need some "knowledge" of these parameters, which implicitly include parameters such as Young's modulus and whisker radius. We do not suggest, however, that the rat "knows" C or L_{BT} as numbers. Instead, we suggest that, through interactions with the environment, the rat gains implicit knowledge of the mechanical properties of its body. The most general result of the present paper is that the rate of change of moment at the base is a curve that monotonically decreases with object radial distance, and this curve scales linearly with whisking velocity. This means that object distance d can always be uniquely inferred from measurement of M for any given whisking velocity θ. The rat must learn the shape of the function that relates M, d, and θ through interaction with the environment. As the whiskers get damaged, fall out, grow back, age, we expect that it will feel "odd" to the rat at first, just as when you put on gloves, the movements of your hands feel different. You have to "learn" the curves that relate a commanded exploratory movement to a particular sensory input. This is all that our models require of the rat.

3.4.5 "Take Home" Messages for Investigators of the Vibrissal System

This paper is by necessity replete with technical details. We want to ensure that the following points are clear:

1) Change in curvature of the whisker and moment (due to whisker deflection) are always proportional. They are related through the quantity EI, representing the whisker bending

stiffness. Both curvature and moment vary as a function of arc length for a deflected whisker, up until the point of contact. A whisker cannot be said to have a single curvature, and it cannot be said to have a single moment. One can only talk about curvature at a point on the whisker and moment at a point on the whisker. A useful point to talk about is often the whisker base, where the rat would actually sense these variables.

2) If an experimenter is performing passive displacement experiments, in which a whisker is grabbed and shaken, it will not be particularly useful to calculate the moment at the base of the whisker. In passive experiments, the moment at the whisker base is linearly related to angular position of the whisker. (Figure 3.8, row 1 and (3.6)). This is very different from situations that can arise during active whisking (Figure 3.8 rows 2 and 3).

3) If an experimenter performing passive displacement experiments for some reason did wish to compute the moment at the whisker base, it can be calculated from (3.6). The experimenter would need to measure the base-to-tip length and base diameter of the whisker, the angular position of the whisker, and the radial distance from the whisker base to the contact location. Both Models 1 and 2 will apply to almost all passive deflection experiments to date, but limitations on their use are shown in Figure 3.3(c).

4) Kinematic descriptions of whisker trajectories are not sufficient to describe the information available to the rat during active behaviors. During active whisking, the whisker can experience very different moments while its base is at the same angular position (Figure 3.8, rows 2 and 3). A complete description of the information available to the rat during active behaviors must include moment, or its geometrical analog, curvature. To ensure the utility of our equations to experimentalists, we have expressed

them both in terms of moment and curvature. If one knows the curvature at the whisker base (say from high-speed video), one can estimate the moment at the base. Conversely, if one knows the moment at a point along the whisker (say from contact with a load cell), one can estimate the curvature near the whisker base.

5) The inherent curvature of the whisker negligibly affects the dependence of the rate of change of moment on radial distance. In contrast, the whisker taper has a large influence on this property.

6) Vibrations of the whisker generated by object contact near the tip are a natural complement to the low-frequency moments that can be generated anywhere along the whisker length. This is likely to permit the simultaneous extraction of texture and shape.

7) The rat could extract radial object distance by keeping track of the rate of change of moment at the whisker base along with whisker angular velocity. This proposed computation for radial distance works for both translation and rotation, and works even if the rat only keeps track of instantaneous rates of change in these variables. In theory, this allows the computation to be performed at every instant in time.

8) The mechanism for computing radial distance proposed in the present study can account for many of the recently-discovered physiological response properties of Vg neurons during active touch [36].

9) The mechanical description of whisking variables presented here has shown that angular position, angular velocity, moment, and the time derivative of moment, can completely describe the dynamic-state of the whisker. This result naturally lends itself to a state encoding scheme, describing the dynamic states of an oscillating cantilever beam. This

representation is likely to be particularly useful when quantifying responses of Vg neurons during active behaviors, and responses at subsequent stages of processing (e.g., the trigeminal nuclei).

10) We propose that the shape of an object can be reconstructed by finding gradients of distance (r, θ, z) over the sensor array, and then gradients of curvature across different positions of the entire array.

Chapter 4

Accounting for Lateral Slip

This chapter contains material that has been slightly altered from the following publication:

J. H. Solomon and M. J. Z. Hartmann, "Artificial whiskers suitable for array implementation: Accounting for lateral slip and surface friction," *IEEE Transactions on Robotics*, to appear.

The biomechanical analysis performed in Chapter 3 revealed that the radial distance to an object can be uniquely inferred by the rate of change of moment sensed at the base of the whisker for a given whisking velocity. However, robotic experiments performed in the early stages of this research revealed that a significant complication called lateral slip can occur when the orientation of the object causes the whisker to bend outside its plane of rotation. This section derives and validates a method for accounting for lateral slip by incorporating the lateral component of moment into the distance extraction equation. It applies to both cylindrically shaped whiskers, as focused upon here, and tapered whiskers, as in the rat.

4.1 Introduction

The growing research into the biological function of whiskers has been paralleled by an increasing interest in constructing their robotic counterparts. The simplest types of artificial whiskers are used as binary contact detection sensors [54-57], which can be used in tasks such as obstacle avoidance [58]. These types of whiskers have been used successfully on several toys (e.g., the BioBug from Wowwee toys). Other researchers have explored the use of artificial whiskers for wall-following [16], for terrain mapping [59], to characterize surface texture [56, 57, 59-61] and surface defects [62], to sense fluid flow profiles [47] and to investigate questions in neuroscience [47, 56, 57]. Most recently, a whisker sensor was designed for precise three-dimensional measurement of heart position in robot assisted beating heart surgery [63].

An important feature of biological whiskers is their ability to extract three-dimensional (3-D) features, either of solid objects or of fluid flows. Several studies have investigated how this capability might be replicated in an artificial whisker array. Tsujimura and Yabuta [64] showed that a stiff, insensitive probe attached to a six-axis force/torque sensor can be used to measure probe-object contact positions along 3-D objects. Russell [65] attached a curved, binary whisker to a Puma robot to sweep along and estimate object contours. Wilson and Chen [66] used a pneumatic bellow tube actuation system to sweep a flexible spring steel wire whisker instrumented with strain gages at the base along objects and estimate their profiles. Ueno *et al.* [67] measured the vibration frequencies of a flexible beam with a payload at the tip to estimate contact point position with an object. Kaneko *et al.* [68] actuate a flexible beam while measuring bending moment at the base to determine contact distance based on the rotational compliance. Russell and Wijaya [69] develop a geometric approach to feature extraction using an array of

eight rigid rods with angle sensors. Scholz and Rahn [70] actuate a Nitinol whisker attached to a mini load cell that measures both force and torque to achieve continuous estimation of 2-D whisker shape, and thus the surface profile as it sweeps along objects. Clements and Rahn [71] used a similar setup along with a two-axis robot to gather discrete contact points while sweeping a whisker along unknown objects. Kim and Möller [72] explore the advantages of using multiple whiskers with the ability to measure both horizontal and vertical deflections for shape recognition. Table 4.1 summarizes several of the whisker sensor technologies that have been successfully implemented and the way in which they were used. In all cases, the actual sensing device resides at or near the base of an insensitive beam (the "whisker"), and a motor is typically used for actuation.

Table 4.1: Whisker sensor technologies.

Sensor	Description
Binary	An electrode housing at the base detects the presence (ON) or lack (OFF) of contact with the whisker. Binary whiskers are usually used for contact detection [16, 55], but have also been used to sense contours [65].
Capacitor microphone	Forces and moments transmitted to the whisker base lead to deformation of a microphone membrane, which has been used to measure surface texture [57, 60] and avoid obstacles [58].
Strain gage	Strain gages are mounted either on a block or on thin plates to measure bending moment at the base of the whisker. They have been used to measure both contact points [47, 59, 63, 66] and texture [56, 59].
Six-axis force/torque load cell	Load cells can measure all three components of both force and moment and have been used to estimate contact points [64, 71] and continuous object profiles [70]. They provide the most information, but tend to be bulky and expensive.
Piezoelectric	Piezoelectric sensors produce signals directly proportional to rate of change of moment at the whisker base [72].
Hall effect	Hall effect sensors measure magnetic flux caused by deflection of the whisker near the base (i.e. moment), and have been used to estimate both contact points [72] and texture [61].
Photo-interrupter	Deflection of the whisker near the base is measured by analog occlusion of a light beam, effectively giving a measurement of bending moment [55].
Vision-based	A CCD camera records deformation of the whisker as it contacts an object, allowing estimation of both contact location and object stiffness [73].

Despite the significant number of studies suggesting the possibility of 3-D feature extraction with whiskers, there are two interrelated problems that have as yet prevented artificial whiskers from being used in large, highly parallel, actuated arrays to sense object features. The first problem is *lateral slip*, in which the whisker slides out of its plane of rotation, thus preventing an accurate measurement of object distance. The second problem, which follows from the first, is that the extent of lateral slip depends on the *coefficient of friction*, which in general is not known and can vary greatly from object to object.

Both Kaneko *et al.* and Clements and Rahn [68, 71] independently addressed the problem of lateral slip by sensing it, and then actively reorienting the plane of rotation until lateral slip is eliminated. However, this method has serious drawbacks: it requires adjustment of actuator orientation to keep the whisker oriented perpendicular to the object [68] and also generally requires multiple rotations for each measurement of contact point location. This is awkward in practice, and infeasible when arrays of multiple whiskers are employed to contact the object.

We demonstrate the ability to quantify and passively accommodate for lateral slip of a rotating whisker in the presence of friction. This permits us to accurately determine the contact location with the object without having to reorient the rotation plane of the whisker. These new results directly enable large-scale implementation on an artificial whisker array actuated with a single motor that may begin to mimic the ability of biological systems.

4.2   Motivation: The Problem of Lateral Slip

One method for obtaining an estimate of 3-D object shape is to determine where in 3-D space each whisker makes initial contact with the object during the course of object exploration, and then interpolate between the resulting collection of contact points to approximate object shape [47]. If we define a cylindrical coordinate system at the base of each whisker, the goal is to estimate the value of each coordinate upon contact: (r_c, θ_c, z_c). We first make the assumption that the plane of rotation for each whisker is fixed at a given height z_c. The variable θ_c can easily be found by denoting the angle at which the moment or rate of moment change measured at the base becomes nonzero or crosses a threshold (assuming that any inertial effects will be negligible or

filtered out). Finally, we are left with the task of estimating r_c – a process we will refer to as *radial distance extraction*.

As noted by Kaneko *et al.*, the rotational compliance of a flexible rod rotated against an "edged" or "point" object increases as the distance to the object increases; in fact, if the rod is cylindrical in shape, compliance is directly proportional to object distance [68]. *Longitudinal slip* occurs when the point of contact moves along the length of the whisker, e.g. when the object is not a sharp edge, but instead has a finite curvature in the plane of rotation (*longitudinal curvature*), as depicted in Figure 4.1(a). The result is a decrease in the resulting rotational compliance and underestimation of contact distance. However, Kaneko *et al.* also showed that (in the absence of lateral slip; discussed next) the decreased compliance will be negligibly small unless the surface has extremely low curvature or contact occurred very close to the whisker base [68].
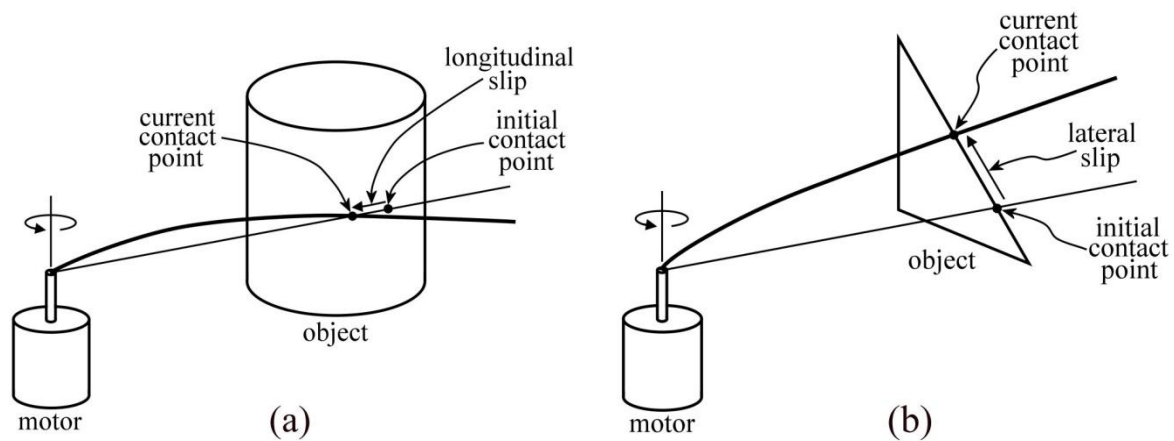
Figure 4.1: There are two types of whisker slip: **(a)** longitudinal slip and **(b)** lateral slip. Note that although here they are depicted independently, they can in general occur simultaneously.

A more significant complication arises when the object surface is slanted relative to the plane of whisker rotation, as shown in Figure 4.1(b). In such cases, a phenomenon called *lateral*

slip occurs, in which the point of contact slides along the periphery of the object, the whisker bends outside the plane of rotation and the resulting compliance is greater than would have occurred without slip, thus leading to an overestimation of contact distance. Techniques developed independently by Kaneko *et al.* [68] and Clements & Rahn [71] involve sensing the lateral slip and actively reorienting the plane of rotation until the lateral slip is eliminated, thus permitting straightforward calculation of contact point location. The problem with this approach when implemented on an array of robotic whiskers is that each whisker requires an individual motor to tilt its plane of rotation. The additional size, cost and complexity requirements make such a solution infeasible, and encourages an alternative approach.

In the present chapter, we develop a model for radial distance extraction that senses lateral slip, but then passively account for its presence through a 2-D modification of the compliance rule found by Kaneko *et al.* [68] to extract radial object distance. The need to adjust the plane of rotation is effectively eliminated as long as a reasonable estimate can be made for the friction coefficient between the whisker and the surface. We quantify analytically how the accuracy of the model degrades for differing friction conditions and object lateral curvatures, and suggest movement strategies to mitigate these inaccuracies. The model is experimentally validated, substantiating the reliability of the analytical results. Finally, we suggest a simple array design capable of actuating an arbitrary number of robotic whiskers with a single motor. In summary, the model demonstrates that distance extraction can be performed even in the presence of lateral slip and friction, to permit reliable and efficient overall shape extraction with a robotic whisker array.

4.3   Distance Extraction in the Presence of Lateral Slip

4.3.1 Object Contact Along the Whisker Without Lateral Slip

The whisker is modeled as a straight, flexible beam rotating with a fixed center of rotation and at a constant velocity. At some point, the whisker comes into contact with an object, at which time the task of finding the distance from the whisker base to contact point arises. We assume the object is rigid and that the point of contact is fixed, discrete, and exists somewhere along the length of the whisker (as opposed to the tip, a condition which will be discussed later). In the case that slip is negligible, the configuration of the whisker can be described in two dimensions as shown in Figure 4.2.
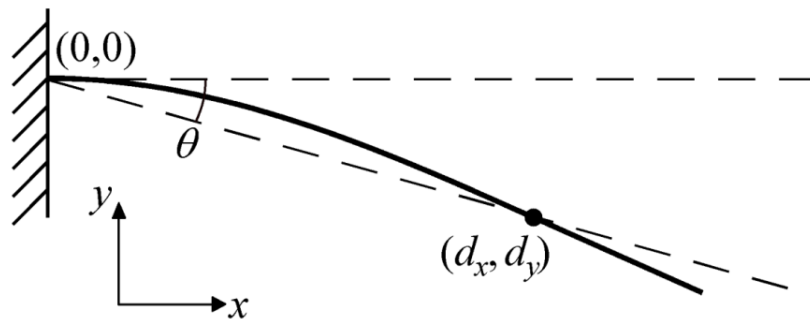
Figure 4.2: Geometry of whisker deflection under no slip.

Because only a small deflection is needed to sense the rotational compliance, classical linear beam theory can be used. The whisker rotates by a small *pushing angle θ* against an object at *radial distance d_x*, imposing a *deflection d_y*. The resulting *bending moment m_z* at the base of the whisker is measured by a torque sensor. Under these conditions, Kaneko *et al.* showed that

the rotational compliance k_θ is directly proportional to object distance [68], and can be expressed as:

$$d_x = Ck_\theta \tag{4.1}$$

where $C = 3EI$, E is the elastic modulus and I is the area moment of inertia. Rotational compliance is defined as the ratio of angular displacement to bending moment at the base, allowing us to write:

$$d_x = C\frac{\theta}{m_z} \tag{4.2}$$

4.3.2 Factors that Influence the Magnitude of Lateral Slip

When orientation of the object is not perpendicular to the plane of rotation at the contact point, lateral slip may occur, in which case the contact point will drag along the periphery of the object, as shown in Figure 4.1(b). The resulting rotational compliance will be greater than when lateral slip does not occur, causing (4.2) to overestimate d_x.

Quantifying lateral slip is aided by analysis of the sensing plane [68], illustrated in Figure 4.3. The sensing plane is an imaginary 2-D projection of the region where the whisker is touching the object, parallel to the y-z plane and intersecting the contact point. In Figure 4.3, the dashed line indicates the initial contact point, the dotted line indicates the current contact point, and the dash-dotted line indicates where the whisker would intersect the sensing plane were it not obstructed by the surface – the so-called 'virtual point' [68]. A basic geometrical analysis of the relationships between variables in the sensing plane is sufficient to derive a modified form of (4.2) that accounts for the lateral slip. We will derive this modified equation in the next section.
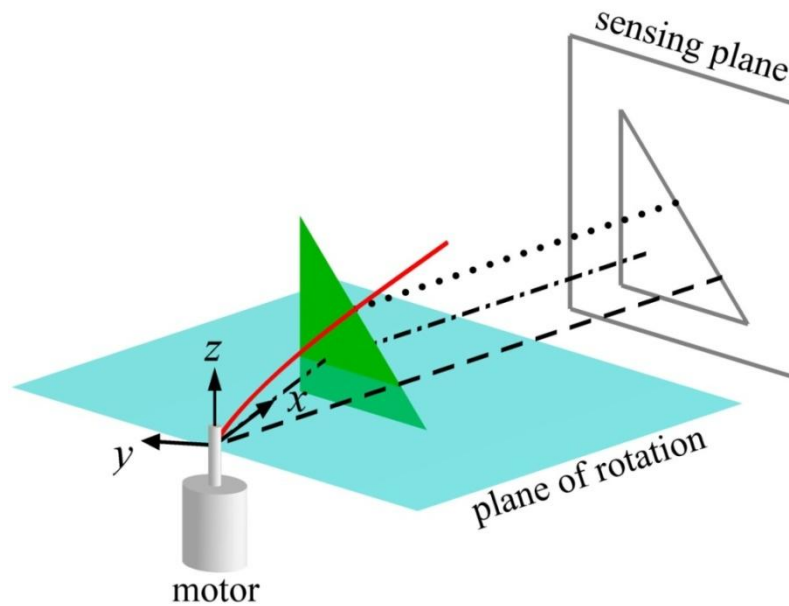
Figure 4.3: A 3-D perspective view of the sensing plane.

There are specific parameters at the region of contact that affect if and how lateral slip occurs. Those parameters are:

1) the slope of the object surface at the contact point within the sensing plane.

2) the curvature of the object surface at the contact point within the sensing plane. In analogy to the term lateral slip, we refer to this quantity as *lateral curvature*.

3) the frictional properties between the whisker and the object.

In the results that follow, we will develop an equation for distance extraction that directly takes into account the slope of the surface at the contact point in the sensing plane. It will be shown that the lateral curvature has only a mildly detrimental impact on distance extraction in most cases as long as θ is sufficiently small. Friction can present some difficulties, although there are ways to address them, which will be discussed.

4.3.3 Accounting for Lateral Slip

In the derivation that follows, we assume that lateral slip occurs in the absence of significant concurrent longitudinal slip (as depicted in Figure 4.3), the implications of which are addressed in the Discussion section. We also assume that both lateral and longitudinal curvatures are zero (i.e. the surface is locally flat), and that traditional Coulomb friction exists between the whisker and the surface. Because this is a quasi-static analysis, any possible discrepancies between static and kinetic friction coefficients are assumed to be negligible.

Figure 4.4 defines the relevant variables projected on the sensing plane. It geometrically predicts the lateral slip σ of the whisker along the object, depending on the local *surface slope β* in the sensing plane and the *friction cone angle α*. Slip will not occur when $\alpha \geq \beta$ because in this case no movement of the contact point is required to keep the contact force f within or on the boundary of the friction cone, and the resulting *slip angle ϕ* will be zero. Conversely, when $\alpha < \beta$, the contact point will slip just enough to enable static equilibrium, resulting in a contact force angle of $\beta - \alpha$.
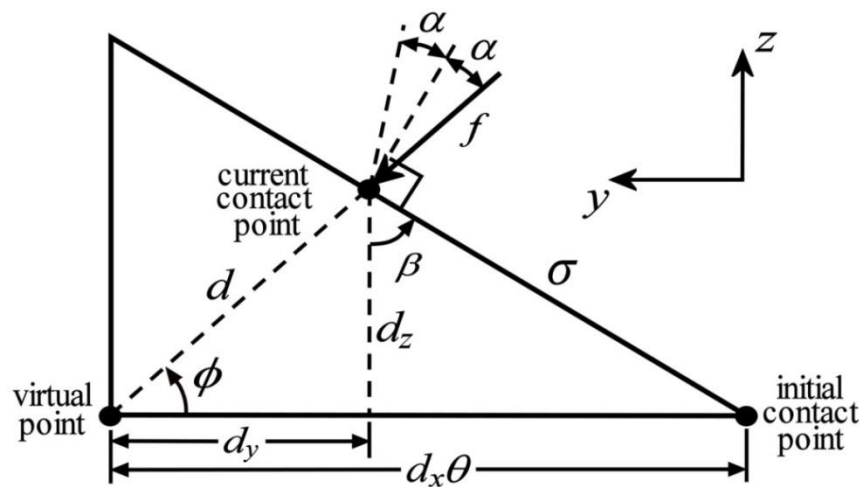
Figure 4.4: A geometrical description of the sensing plane

Summarizing, we have

$$\text{if } \begin{cases} \alpha \geq \beta, & \phi = 0 \\ \alpha \leq \beta, & \phi = \beta - \alpha \end{cases} \tag{4.3}$$

which can be expressed more compactly as

$$\phi = \max(0, \beta - \alpha) \tag{4.4}$$

Notice that the overall linear deflection d is now split into two components: d_z and d_y. This means that to sense lateral slip, the torque sensor at the base of the whisker must be equipped to measure out-of-plane bending of the whisker, that is, bending moment m_y. For small angles, the distance between the virtual point and the initial contact point is simply the contact distance d_x multiplied by θ. Following the geometry of Figure 4.4, it can be shown that the slip distance σ along the object is:

$$\sigma = \frac{d_x \theta}{\sin \beta + \cos \beta \cot \phi} \tag{4.5}$$

Using this model of lateral slip, we seek an equation analogous to (4.2) that will allow determination of the distance d_x based on known and measurable variables: E, I, θ, m_z and m_y. Analysis of Figure 4.4 along with application of some basic cantilever beam analysis (see Appendix E) yields the following result:

$$d_x = C \frac{\theta}{m_z + m_y \tan \beta} \tag{4.6}$$

Unfortunately, there's no way to reliably estimate the surface slope β in the presence of unknown friction. The most straightforward concession that can be made to arrive at a solution is to assume or estimate some nominal friction coefficient μ_{est}. First, we note that

$$\alpha_{est} = \tan^{-1}(\mu_{est}) \tag{4.7}$$

and that ϕ can be directly measured as

$$\phi = \tan^{-1}(m_y / m_z) \tag{4.8}$$

If we now assume $\alpha_{est} \leq \beta_{est}$, β_{est} can easily be computed using (4.3):

$$\beta_{est} = \phi + \alpha_{est} \tag{4.9}$$

Replacing the unknown surface slope β from (4.6) with β_{est} yields

$$d_x = C \frac{\theta}{m_z + m_y \tan \beta_{est}} \tag{4.10}$$

Note that (4.10) is reliable even when $\alpha_{est} > \beta_{est}$ (contrary to the assumption made in (4.9)) because in this case $m_y = 0$ and the term $m_y \tan \beta_{est}$ becomes zero as well.

One obvious situation to consider is that of frictionless contact, resulting in $\beta_{est} = \phi$ and thus

$$d_x = C \frac{\theta}{m_z + m_y^2 / m_z} \tag{4.11}$$

which can alternatively be written as

$$d_x = C \frac{\theta}{|m|} \cos \phi \tag{4.12}$$

where $|m| = \sqrt{m_z^2 + m_y^2}$ as in [47].

In the following section, the two most significant potential sources of distance extraction error are addressed analytically, namely discrepancy between α_{est} and the true α, and lateral curvature of the object surface.

4.4   Potential Sources of Distance Extraction Error

4.4.1   Unknown Friction Coefficient

Distance extraction using (4.10) requires an estimate of the friction coefficient between the whisker and the surface. In order to characterize how discrepancy between α_{est} and the true α results in distance extraction error, we return to the lateral slip model of Figure 4.4 to obtain (see Appendix E):

$$m_z = \frac{C\theta}{d_x}\left(\frac{1}{\tan\beta\tan\phi + 1}\right) \tag{4.13}$$

$$m_y = \frac{C\theta}{d_x}\left(\frac{1}{\tan\beta + \cot\phi}\right) \tag{4.14}$$

Equations (4.13) and (4.14) along with (4.4) define how m_z and m_y will increase as the whisker rotates against a slanted surface as a function of α and β. Thus, assuming some estimate of friction cone angle α_{est}, we can numerically compute the surface slope β_{thresh} at which at a given percentage of distance extraction error (an "error threshold") is incurred for a range of actual friction cone angles α. β_{thresh} can in principle range between 0° (vertical) and 90° (horizontal). The larger β_{thresh} is, the more reliable the distance extraction is in the presence of a complex and/or arbitrarily oriented object.

Figure 4.5(a,b,c) shows the relation between β_{thresh} and α for $\alpha_{est} = $ 0°, 10° and 20°, respectively. The surface slope at 1%, 5% and 10% error thresholds for distance extraction using (4.2) and (4.10) are represented by dashed lines and the solid lines, respectively. Naturally, as the error threshold increases, so does β_{thresh} for both distance extraction equations. However, Figure 4.5(a) shows that (4.10) is always equally or more accurate than (4.2) when $\alpha_{est} = $ 0°, with the

relative advantage becoming progressively more significant with increasing error threshold level. The advantage of (4.10) over (4.2) is even more pronounced when a reasonable guess can be offered for α_{est}. So long as α_{est} falls within a moderate range of α, distance extraction will be accurate even for steep surface slopes. For example, Figure 4.5(b) tells us that if $\alpha_{est} = 10°$, distance extraction will be accurate to within 5% so long as α ranges between 8.2° and 11.7° and $\beta \leq 60°$, or to within 10% so long as α ranges between 7.8° and 12.3° and $\beta \leq 70°$.
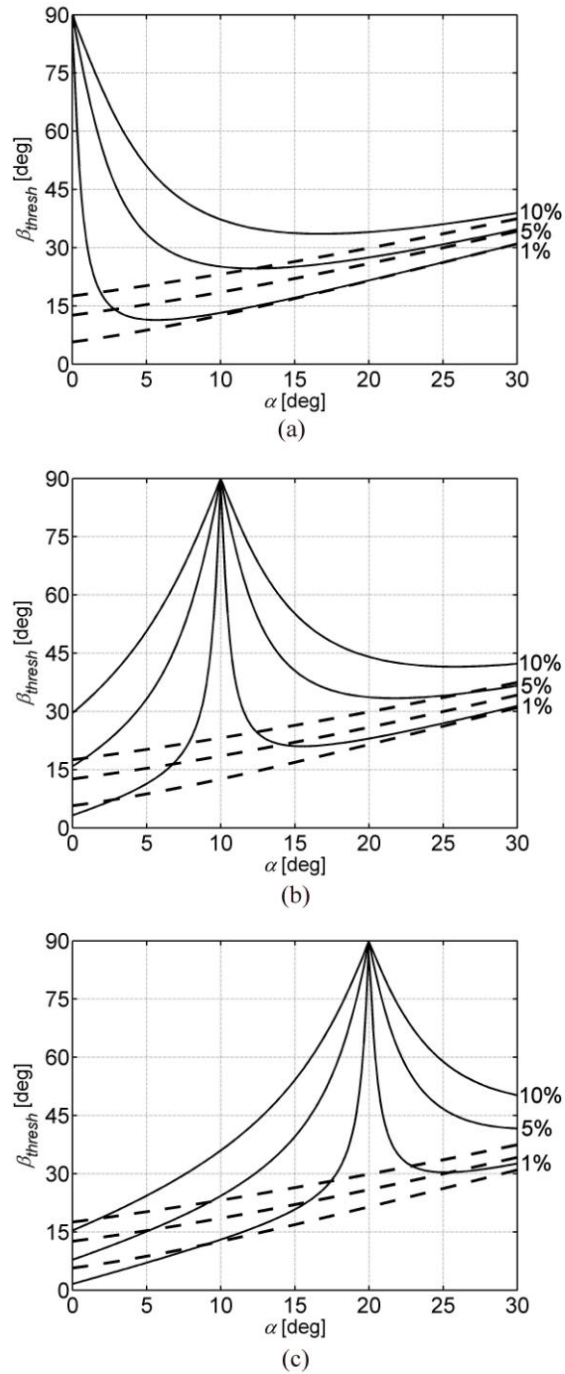
Figure 4.5: Error threshold analysis for maximum allowable surface slope given particular deviations between α and α_{est} with **(a)** $\alpha_{est} = 0^0$, **(b)** $\alpha_{est} = 10^0$, **(c)** $\alpha_{est} = 20^0$. β_{thresh} is the surface slope at which at a given percentage of distance extraction error is incurred for a range of actual friction cone angles α. Dashed lines represent β_{thresh} calculated using (4.2). Solid lines represent β_{thresh} calculated using (4.10).

4.4.2 Lateral Curvature of the Object Surface

Equation (4.10) assumes that the surface being contacted has a lateral curvature of zero. Although this at first may seem to be a restrictive assumption, one must consider the effect of curvature within the scale of the contact distance. The radius of curvature r_κ scaled relative to the contact distance d_x, defines the *normalized lateral curvature* as

$$\kappa_n = d_x / r_\kappa \tag{4.15}$$

and thus the *normalized radius of curvature* as $r_n = 1/\kappa_n$. The smaller κ_n is, the flatter the surface effectively is. Note, however, that the effect of curvature on distance extraction must be considered in the context of three additional variables: θ and α, as defined above, and also β_0 – the surface slope in the sensing plane at the initial contact point. To understand the interplay between these variables, we may refer to error threshold plots similar to those in Figure 4.5, but now with r_n as the independent variable (see Appendix F for derivation).

Figure 4.6(a), (b) and (c) plot the maximum allowable β_0 (β_{thresh}) as a function of r_n that keeps distance extraction error under 1%, 5% and 10% respectively. Each plot shows these relationships for three different pushing angles: $\theta = 1°$, $3°$, and $5°$. As expected, β_{thresh} always increases with increased error threshold and with increased r_n (surface flatness).
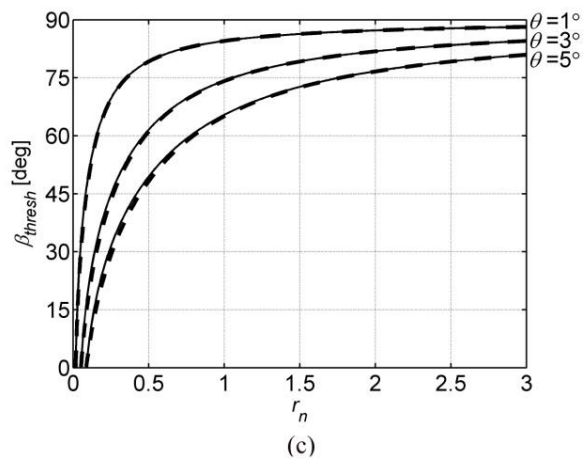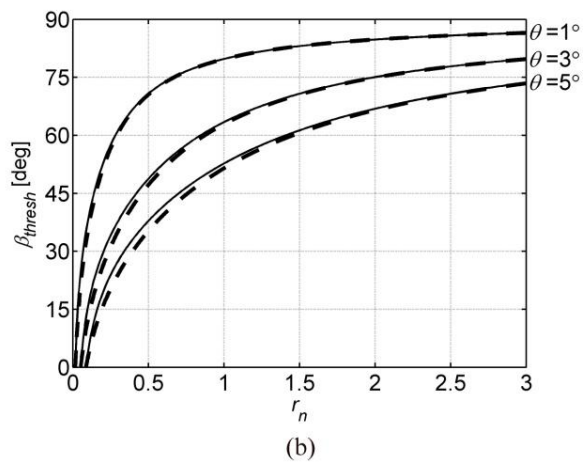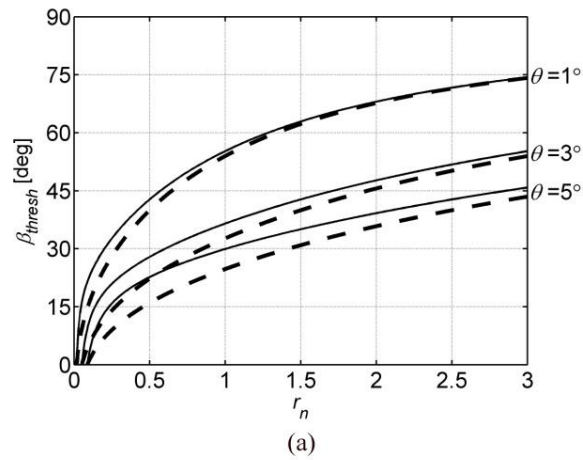
Figure 4.6: Error threshold analysis for maximum allowable surface slope given particular normalized lateral radii of curvature and **(a)** 1% error, **(b)** 5% error, **(c)** 10% error. Dashed lines are for frictionless contact (and $\alpha_{est} = 0°$), and solid lines are for contact with $\alpha = 20^0$ (and $\alpha_{est} = 20°$).

Interestingly, Figure 4.6 illustrates that friction has an overall negligible impact, while in contrast, increasing θ has a significantly detrimental impact. The reason for this goes back to the issue of scale – a larger θ will result in a larger slip relative to any given r_n, and thus more deviation from the assumption of a flat surface. As a practical issue, the benefit of using a small θ to guard against lateral curvature must be balanced against the decreased reaction torque at the whisker base that will result. Generally speaking, θ should be chosen to be as small as possible while still ensuring a sufficient reaction torque to allow accurate distance extraction when contact occurs near the whisker tip.

Overall, Figure 4.6 shows that the consequence of lateral curvature is relatively mild. For example, given a significantly curved surface with $r_n = 1$ and a realistic pushing angle of $\theta = 3°$, a β_0 of 63° will result in 5% distance extraction error and a β_0 of 74° will result in 10% error. Increasing θ to 5° would decrease the maximum β_0 to 52° and 65°, respectively.

4.5 Model Validation

Experimental validation of the lateral slip model was performed. The artificial whisker used for these experiments had two components: a flexible beam (the "vibrissa") and a two-axis torque sensor (the "follicle") (see Figure 4.7(a)).
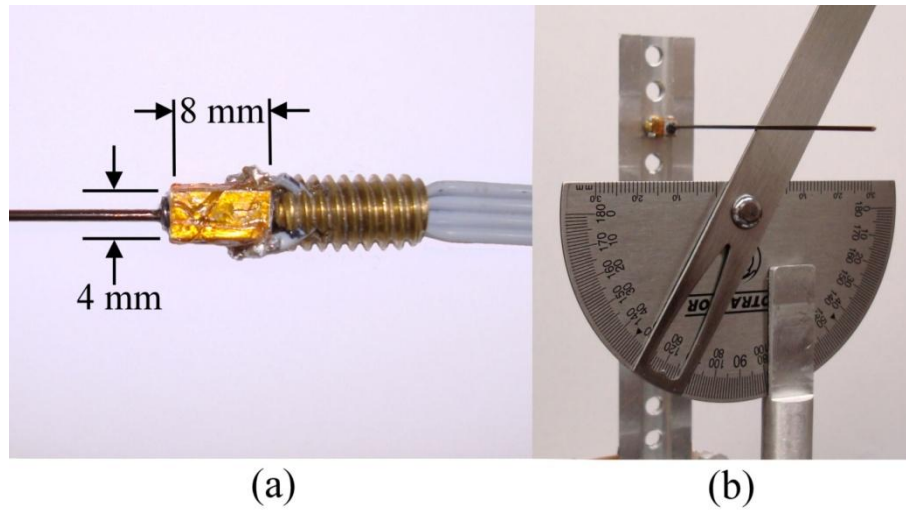
Figure 4.7: The experimental setup: **(a)** the whisker follicle, and **(b)** the object surface (a protractor).

The vibrissa is a straight superelastic Nitinol wire, 1 mm in diameter and 10 cm in length, with a small setscrew attached at the base. The relatively thick wire diameter was chosen to ensure a strong torque signal to sense small lateral deflections; generally, much thinner whiskers can be used. The setscrew allows different size and shape vibrissa to be easily interchanged within the follicle. The follicle is a small aluminum block (4×4×8 mm) with the center tapped to match the setscrew at the base of the vibrissa. Each of the four faces of the follicle is fitted with a strain gauge, allowing independent measurement of m_z and m_y, and the follicle itself is attached to a larger setscrew to allow easy connection to an array. For these experiments, the array was simply a vertically oriented aluminum bar with a series of threaded holes, which allowed whiskers to be configured in a single column (see Section 4.6). The array was attached to an AC servomotor at the base for actuation. The most important – but not essential – feature of the present design is that it positions the base of the vibrissae (and the tips of their follicles) at the center of rotation, thus conforming to the model as expressed in (4.13) and (4.14). Equations

(4.13) and (4.14) could be modified to account for non-center rotation (similar to [72]), but that was not tested in the present experiments.

The experiment involved rotating the whisker against a slender stainless steel bar (see Figure 4.7(b)) at a variety of surface slopes: from $\beta = 0°$ (vertical) to 75° (nearly horizontal) in 5° increments (similar to [72]), and at two different speeds: $\dot{\theta} = 10$ deg/s and 90 deg/s. Signals from the follicle strain gages were first calibrated from voltage to moment. The m_y component was calibrated by rotating the whisker against the bar with $\beta = 0°$ at a radial distance of $d_x = 5$ cm. Ten whisks were performed at both $\dot{\theta} = 10$ deg/s and 90 deg/s. The location at which the whisker gently touched the bar was defined as $\theta = 0°$. Whisker trajectories were chosen to ensure a smooth acceleration to the maximum velocity. For $\dot{\theta} = 10$ deg/s the whisker was rotated through a range of –3° to 12°, while for $\dot{\theta} = 90$ deg/s, an expanded range of –15° to 20° was used. All data were filtered at 800 Hz, sampled at 2000 Hz and passed through a zero-phase digital filter with a cutoff frequency of either 5 Hz (for $\dot{\theta} = 10$ deg/s) or 45 Hz (for $\dot{\theta} = 45$ deg/s). Using (4.2) along with a pushing angle $\theta = 3°$, we arrive at a calibration factor between voltage and moment m_y. The follicle was then rotated 90° and the calibration process repeated for m_z.

Experimental data were gathered in the same way as the calibration process, but for varying β. For each β, the plane of the bar was perpendicular to the orientation of the whisker at $\theta = 0°$. Figure 8(a,b) plots $|m|$ and ϕ vs. β, for the two different whisking velocities. Units for $|m|$ are EI/meters, that is, equivalent to $EI \cdot \kappa$ since $\kappa = m/EI$. Figure 4.8(c,d) is the same as Figure 4.8(a,b), except that a rough surface was obtained by covering the object surface with 180 grit

(fine) sandpaper. The sandpaper was replaced for each β to prevent wear from affecting the results. Least-mean-square (LMS) fits were performed on the experimental data sets. Specifically, LMS fits were performed on the sum of the squares of (4.13) and (4.14) with α_{est} as the free parameter. Absolute value of the moment was then calculated as $|m| = \sqrt{m_z^2 + m_y^2}$, and ϕ was calculated from (4.8).

Figure 4.8(a) demonstrates that an excellent fit between model and experiment was obtained for whisking against the steel rod at 10 deg/s, for an estimated value of friction cone angle $\alpha_{est} = 10.5°$. At 90 deg/s (Figure 4.8(b)) the data again conforms well to the model, the fit yielding $\alpha_{est} = 12.3°$, but the measurement variability is significantly higher. The increased variability is likely due to dynamic effects, namely vibrations, starting to become significant, though this was not confirmed.

Figure 4.8(c,d) illustrates the phenomenon of stick-slip friction, in which the whisker irregularly switches between periods of no slip, smooth slip and sudden, abrupt slip. This led to a high level of variability in the data obtained at $\dot{\theta} = 10$ deg/s, but had a smaller effect at $\dot{\theta} = 90$ deg/s. The difference is likely due to the well-known sensitivity of stick-slip behavior to velocity. The fits to $\dot{\theta} = 10$ and 90 deg/s yielded 23.3° and 18.7°, respectively for α_{est}.
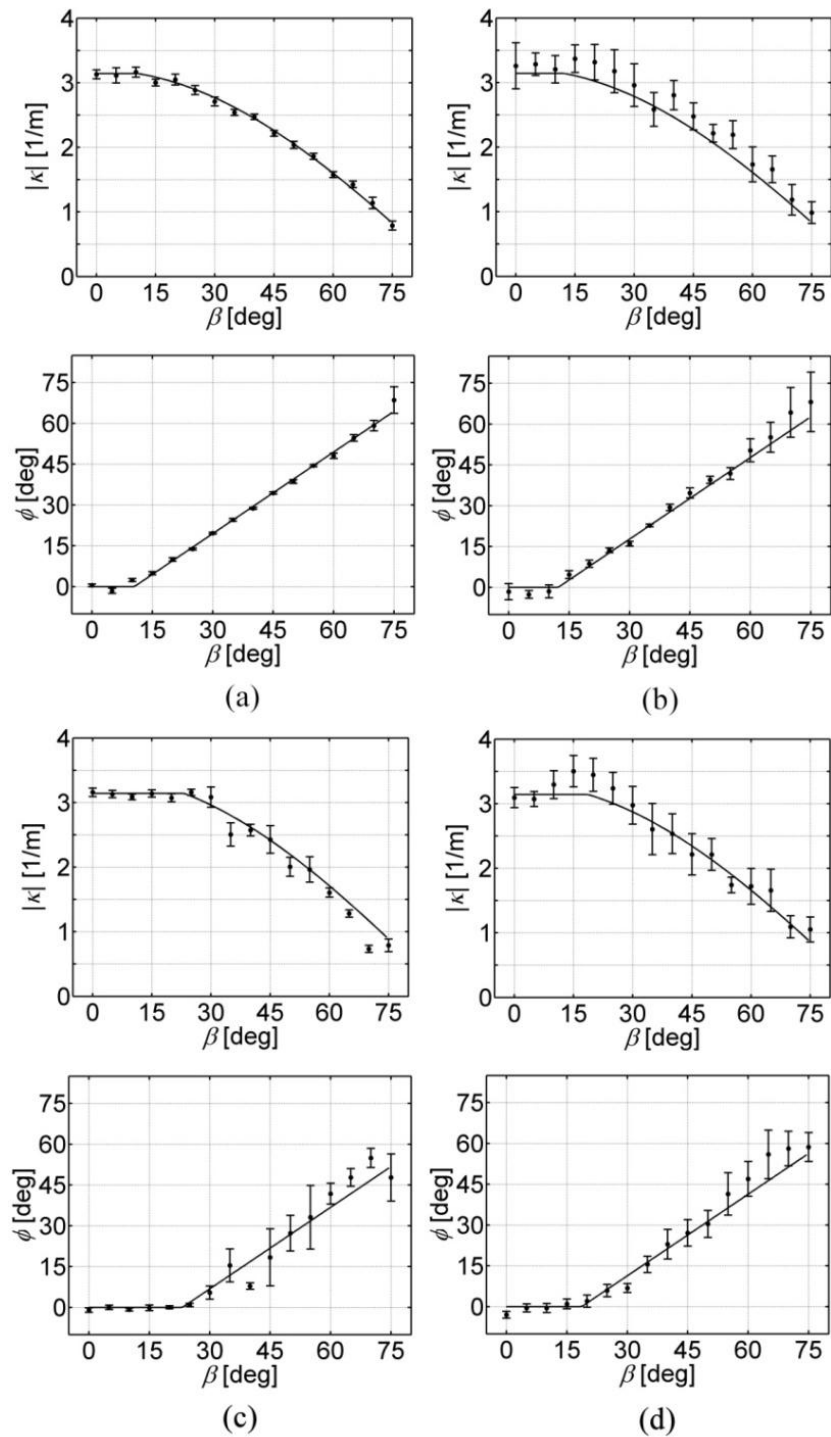
Figure 4.8: Experimental results for stainless steel surface with **(a)** $\dot{\theta}$ = 10 deg/s, **(b)** $\dot{\theta}$ = 90 deg/s, and for sandpaper surface with **(c)** $\dot{\theta}$ = 10 deg/s, **(d)** $\dot{\theta}$ = 90 deg/s. Error bars are standard deviations. Solid lines are LMS fits, calculated as described in the text.

4.6 Array Design

Although the results presented here have specifically addressed radial distance extraction with a single whisker, they are particularly relevant to implementation on an array of robotic whiskers. Because the proposed method allows radial distance extraction to be performed in the presence of lateral slip, multiple whiskers can be configured into arrays wherein their relative base-positions and planes of rotation are fixed. Hence, the method enables the synchronous movement of multiple whiskers against an arbitrarily shaped and oriented object to efficiently collect multiple contact points, which can be processed in parallel to extract complex surface features [47].

Because whisking often involves the rotation of multiple whiskers in close synchrony, a desirable property of a whisker array is the need for only a single motor for actuation. In [60], a servomotor is used to move a flexible membrane, through which the base region of multiple whiskers is threaded, thus allowing a 40° whisking amplitude. In [72], a DC motor connects to a support plate, upon which multiple whiskers are attached at varying angles. As mentioned in Section 4.5, the present model requires that each whisker rotate about its cantilevered base – where the moment sensor resides – requiring a different design than [60] and [72]. Our solution was to mill an aluminum cylinder down to a slender plank except for the region at the base, where a hole is drilled for attachment to an AC servomotor. Several holes were then drilled through the plank and threaded for attachment of the whiskers. Figure 4.9 shows the entire array along with four whiskers, similar to the one used in the above experiments (see Figure 4.7(a)).
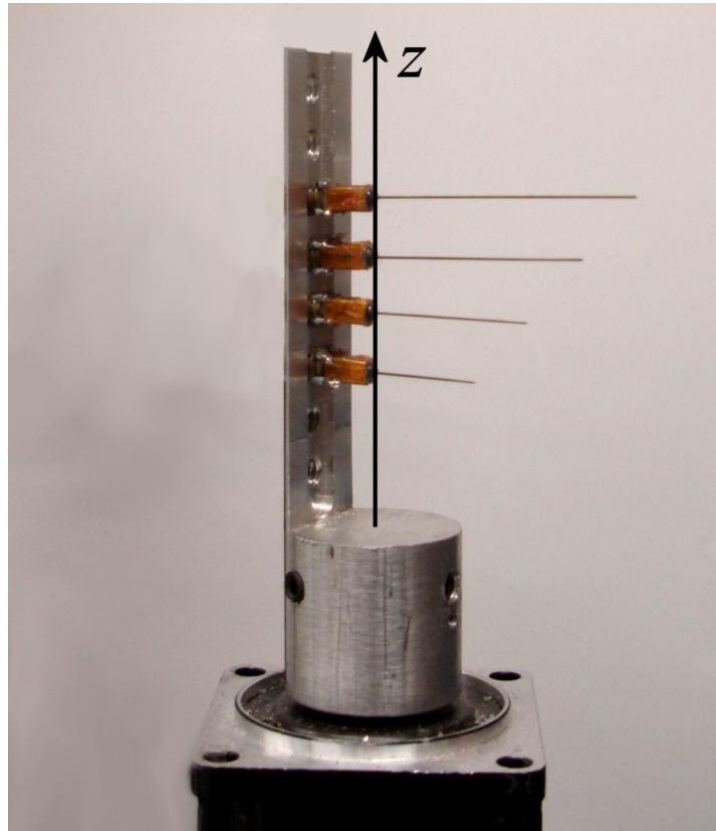
Figure 4.9: Array design for a single column of whiskers.

In order to actuate multiple columns of whiskers, a simple solution is to use a classic multi-bar linkage system, such as the one used in [59], thus allowing for the actuation of an arbitrarily-sized grid of whiskers, still using only a single motor.

4.7 Discussion

This chapter has demonstrated that reorientation of the whisking plane is not necessary for reliable measurement of contact point location, thus opening the possibility for whisker arrays of simple mechanical design capable of detailed 3-D feature extraction. In order to perform accurate

feature extraction with objects of arbitrary shape and orientation, a reasonable estimate of the friction coefficient between the whisker and the object is beneficial. In many cases, it may be reasonable to assume the environment is composed of mostly smooth surfaces, in which case an estimate of $\mu_{est} = 0.18$ ($\alpha_{est} = 10°$) should be reasonable, as indicated in by the fits in Figure 4.8(a,b). If that assumption is inaccurate and the surface is rough, say with $\alpha = 20°$, then Figure 4.5(b) tells us that distance extraction will remain accurate to within 10% error as long as the surface slope β is less than about 45° (also depending on the normalized lateral curvature κ_n and pushing angle θ, as shown in Figure 4.6).

If a more reliable estimate is desired, there are a few possible solutions, as follows:

1) If the orientation of the entire whisker array can be tilted along the x-axis of any particular whisker, whisks would be performed against the object at a variety of orientations, effectively adjusting the relative surface slope. The range of slopes for which $\phi = 0°$ would be equal to $2 \cdot \alpha$ (the accuracy depending on how gradually the orientation was adjusted). This essentially amounts to an in-field test of the object to determine the friction coefficient. Note that this change in orientation occurs for the entire array (not for each individual whisker) and only needs to be done when a new estimate of friction is desired.

2) Have the array explore the object, and repeat the feature extraction algorithm (the transformation of contact points into 3-D object shape, e.g. splining [47]) using a range of friction coefficients. The one that leads to the most consistent contact point positions and thus the smoothest surface is kept.

3) Have the array whisk against the object at a variety of array orientations. All the contact points sampled are given a confidence measure related to ϕ, such that points with large ϕ are ignored or have less influence on the feature extraction algorithm.

Methods 1 and 2 assume the friction coefficient is constant over the entire object, while method 3 does not.

Another problem involves the occurrence of stick-slip, in which the coefficient of static friction is significantly greater than that of kinetic friction (which the model assumes are the same). However, we have shown experimentally that stick-slip is reduced by whisking quickly (e.g., 90 deg/s), a behavior that is also desirable for the sake of sensing an object quickly, as rats are able to do.

Other potential sources of distance extraction error include:

- simultaneous longitudinal and lateral slip – The analysis performed in this paper assumes that no longitudinal slip occurs along with the lateral slip. However, this assumption is not always valid. Consider the case in which the object shown in Figure 4.3 is tilted by an angle ψ either towards or away from the motor instead of oriented vertically. This could cause simultaneous lateral and longitudinal slip, depending on the friction conditions and particular values of β and ψ. Additional analyses are required to quantify the effect on distance extraction, but it should be small unless both β and ψ are large.

- object compliance – A solution is offered in [68] in which two whisks are performed on the object from two different distances, and the difference in whisker compliance reveals both the contact distance and a measure of the object compliance.

- multi-point contact – This should be rare even for complex objects because it would require two distinct point along the object's surface to closely line up along the initial contact orientation of the whisker. As the pushing angle θ becomes smaller, this situation becomes increasingly unlikely.

- moving objects – Most environments are static on the temporal scale over which exploration is likely to occur. Also, if the environment is moving, its velocity is often negligible relative to the whisking speed $\dot{\theta}$. Because the whiskers have very little mass, they can move very rapidly (in rats, up to 1500 degrees/second [23]).

One final issue involves contact occurring at the whisker tip. Such cases may result in decreased rotational compliance, causing (4.6) to estimate d_x to be greater than the whisker length. The solution is to simply give d_x a threshold equal to the whisker length [47]. It is also worth noting that regions of an object that are concave with respect to the plane of whisker rotation can only be sampled through tip contact if the whisker is straight. Tip contact is thus actually desirable for two reasons: it potentially helps provide a very precise measurement of contact distance (since the whisker length is exactly known), and allows concave regions of an object to be sampled.

We point out that the method presented here is not limited to the case of a cylindrical whisker. In general, moment can be related to pushing angle by a monotonically decreasing stiffness function that depends on the shape and elastic modulus of the whisker [47]. This allows us to write (4.12) in the more general form:

$$d_x = v(\theta, |M|)\cos\phi \qquad (4.16)$$

where $v(\theta, |M|)$ is the distance extraction equation for the whisker in the case of no lateral slip ((4.2) for a cylindrical whisker). For the case of a conical beam, which is a good approximation for a rat whisker (see Chapter 3 and [47]), we have:

$$d_x = \frac{C\theta L}{C\theta + |M| L} \cos\phi \qquad (4.17)$$

4.8 Conclusion

We have demonstrated the effectiveness of a method to measure contact point location with an artificial whisker in the presence of significant lateral slip and surface friction. The method requires only that the whisker be equipped with a two-axis torque sensor at the base, and works best when a reasonable estimation for the object's friction coefficient is available. The biggest advantage of this method is that it does not require that each whisker can independently adjust its plane of rotation, and is thus very amenable to implementation on an array of whiskers to extract complex object features, as is done in the next chapter.

Chapter 5

Object Feature Extraction

This chapter contains material that has been slightly altered from the following publication:

J. H. Solomon and M. J. Hartmann, "Robotic whiskers used to sense features," *Nature,* vol. 443, p. 525, Oct. 5 2006.

5.1 Introduction

Chapters 3 and 4 addressed the problem of radial distance extraction with a whisker in great detail. Combined with the angular position of contact and the height of the whisker (which can be considered fixed), the 3-D location of contact can be defined in terms of cylindrical coordinates. Importantly, behavioral and electrophysiological experiments have thoroughly established that rats possess the ability to extract both the radial [30, 36, 38, 74] and angular [38, 52, 74, 75] position of an object with a single whisker, and that whisking movements are generally constrained to within a plane [23, 76, 77]. One might argue that extraction of a discrete contact point cannot account for the rat's ability to sense the shape of objects, but one must consider that a rat typically whisks at about 8 Hz and possesses 30 macrovibrissae on each side

of the face, thus accounting for the extraction of about 500 contact points in a single second! Clearly the inference of shape is possible from such a spatially dense sampling, but to do so with precision requires the adherence of several critical assumptions (see Chapter 4). Here I show experimentally that detailed feature extraction is possible with a robotic whisker array using the method outlined in Chapter 4, combined with the use of a spline to fit a smooth surface to the contact points.

5.2 Methods and Results

The array discussed in Section 4.6 was implemented with 4 robotic whiskers of length 5, 4, 3 and 2 cm (top to bottom), each 0.5 mm in diameter and spaced vertically by 1 cm. A small sculpted head was used as the subject for feature extraction due to its intricate concavities and convexities. These items are shown in Figure 5.1, with their relative scale preserved.
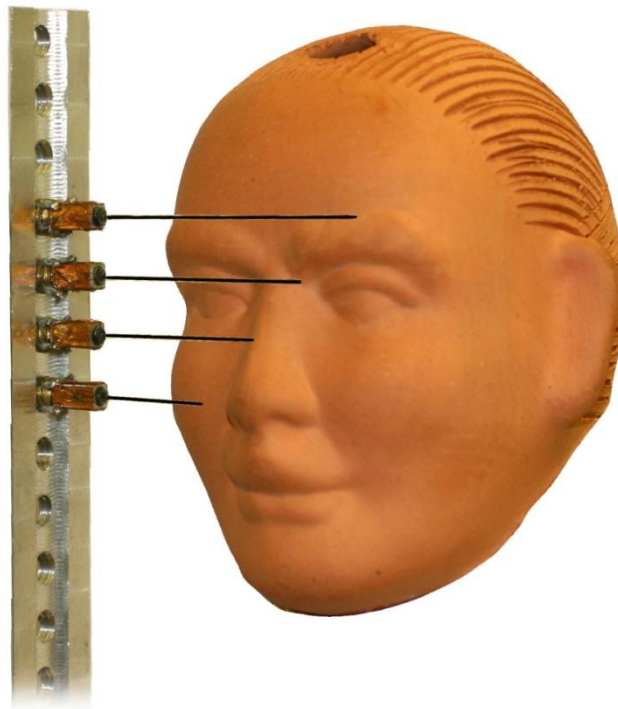
Figure 5.1: The whisker array and sculpted head.

Calibration between voltage and moment for the artificial whisker array was performed by sweeping each whisker five times against a peg placed at a single distance of 2 cm. A low whisking velocity (10 deg/s) minimized inertial effects and maximized the resolution of contact angle detection. This same procedure was then done with the whisker follicles rotated 90° to calibrate in the vertical plane (necessary to sense whisker movements out of the plane of primary motion).

To gather experimental data, the sculpted head was fixed at the center of a cylindrical coordinate system (r, θ, z) while the array whisked at several different positions. Note that θ of this general coordinate system is not the same as the angle θ through which the whisker deflects.

The array was positioned at regular intervals of height z and angle θ. The choice of r was necessarily dictated by the requirement that the whiskers make contact with all regions of the left side of the head (Table 5.1).

Table 5.1: The array was positioned in regular intervals of height z and angle θ, while distance r was manually chosen to ensure whisker contact with all regions of the face.

z (cm)	θ (degrees)	r (cm)
0.000 – 2.000, 0.125 cm increments	0 – 60˚, 10˚ increments	5.00
2.125 – 3.250, 0.125 cm increments	"	4.75
3.375 – 4.250, 0.125 cm increments	"	5.50
4.375 – 6.000, 0.125 cm increments	"	5.25

A single whisk was performed at each position. Analog signals from each whisker base were filtered at 160 Hz, sampled at 500 Hz and then passed through a zero phase forward digital filter (period = 1/2 second). The location of each contact point was then computed relative to the array. The angular component θ was taken to be the angle at which the whisker first made contact with the object (when $\dot{M}$ crossed a threshold), and the radial d component was found using (4.12) (i.e., the surface friction was assumed to be zero).

A total of 343 whisks were performed. In cases where a whisker did not make contact, or the data analysis showed that the whisker hit on the right side of the face, the data were automatically removed. All other contact points were mirror-imaged to the right side of the head. The longer whiskers captured the broad convex features, while the shorter whiskers explored the finer concave regions. Equation (4.12) was also used to determine when contact occurred at a

whisker tip. Tip contact always resulted in an estimate of *d* very close to or greater than the whisker length. In the case that estimated *d* was greater than the whisker length, *d* was automatically set equal to the length. Thus, (4.12) provided the critical information that contact did indeed occur at the whisker tip and not mid-length. This would not have been possible had the sensing mechanism been, for example, a simple binary contact-switch.

Note that regions of the sculpture that are concave in the horizontal plane (for any given height) are only reachable through tip contact, which accounts for 25% of the splined surface. A total of 1036 contact points on the left side were collected, with 438 points determined through (4.12) to occur at or near the tip (42% of all points). The points were converted to head-centered Cartesian coordinates to simplify splining, mirror-imaged to the right side, and plotted along with the spline to create Figure 5.2.
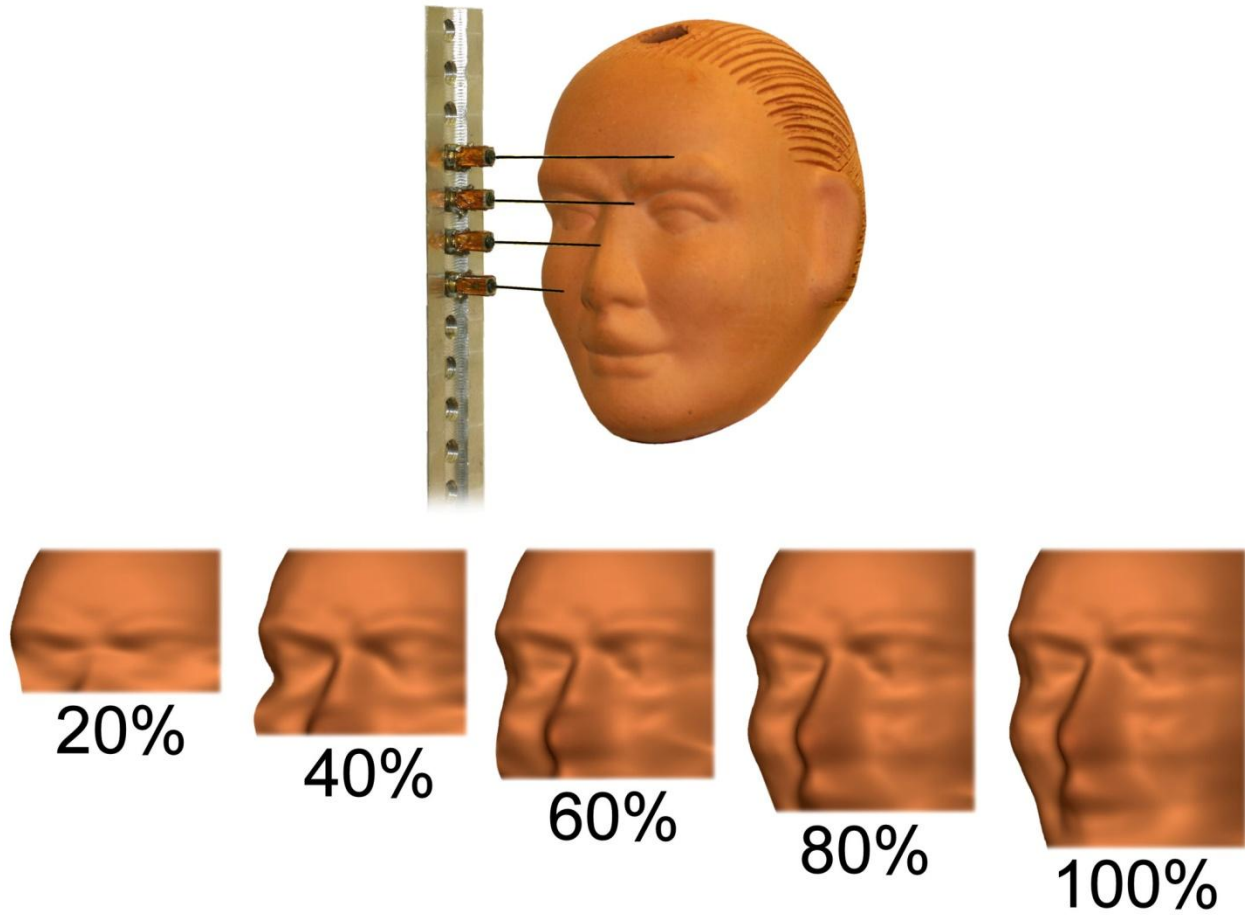
Figure 5.2: The process of feature extraction. The sculpture was "scanned" from top to bottom, hence the gradual extraction of features in the vertical dimension.

Chapter 6

Object Profile Extraction

This chapter contains material that has been slightly altered from the following publication:

J. H. Solomon and M. J. Z. Hartmann, "Object profile sensing with a robotic whisker using only torque information," in preparation.

6.1 Introduction

Chapter 4 reviewed the current literature with regards to robotic whiskers. Here, we subdivide those approaches related to the subject of feature extraction into two categories. The first, more straightforward approach was the subject of Chapters 3-5, wherein the whisker rotates (or translates) against the object by a small angle to accomplish radial distance extraction. Using this information, along with the angle of initial contact and location of the whisker base, allows estimation of the contact point location in 3-D space for each whisker during each whisk. The second approach incorporates moving the whisker along or against the object by a significant amount past initial contact in order to estimate a collection of contact point locations as the

whisker slips along the surface. The former approach will henceforth be referred to as *tapping*, and the latter as *sweeping*. For the sake of completeness, we again review the relevant literature.

Several studies have addressed whisker tapping. Tsujimura and Yabuta derived and demonstrated a general method of estimating contact point location of a stiff probe (e.g., a beam) pressing against an object using a six-axis force/torque sensor [64]. Ueno *et al.* measured vibration frequencies at the base of a flexible beam using a torque sensor to estimate contact point position [67]. Kaneko *et al.* used a two-axis actuator, two-axis torque sensor and a flexible beam to determine contact positions along an object based on the rotational compliance [68]. Clements and Rahn applied a large-angle elastica model as the basis for determining contact point location with a two-axis actuator, flexible beam and six-axis force/torque sensor [71]. Kim and Möller attached multiple flexible beams with two-axis torque sensors to an actuated support plate, showing that whisker arrays can provide basic object shape information in a single whisk [72]. My own research, outlined in Chapters 4 and 5, has shown that highly detailed shape information can be extracted by using a whisker array and combining data from several whisks, while accounting for lateral slip of the whiskers along the object.

Whisker sweeping, the approach undertaken in this chapter, has received somewhat less attention in the literature than tapping. Russell swept the tip of a flexible curved beam with a binary (touch or no-touch) sensor along objects with a Puma robot to measure their profile [65]. Wilson and Chen used a pneumatic bellow tube actuation system and closed-loop control to sweep the tip of a flexible beam with a 2-D torque sensor along objects and estimate their profiles [66]. Scholz & Rahn rotated a flexible beam equipped with a six-axis force/torque load

cell against objects and used a large-angle elastica model to repeatedly compute the entire whisker shape, providing an accurate 2-D object profile measurement with a single whisk [70].

The approach outlined in this chapter was inspired by the ultimate goal of constructing a whisker array that mimics the structure of that found in the rat. This places two fundamental constraints on the system: 1) each whisker much rotate about its base, where the bending moment (torque) is measured, and 2) all whiskers must rotate in unison, thus reasonably approximating a natural whisking motion and also allowing for a simple array design that requires only a single motor for actuation (see Section 4.6 and [59]). Chapter 4 has established a method for performing initial contact point measurement under these conditions. A natural extension to these results is to develop a sweeping technique that will allow continued estimation of contact point beyond initial contact, thus providing the maximum amount of available shape information per whisk, and is the topic of this chapter. Although this capability was impressively achieved by Scholz and Rahn [70], their method is incompatible with our envisioned array design, as the requisite force/torque sensor is too bulky and expensive to be considered for array implementation. Their method also lacks biological plausibility. Hence, the method presented here accomplishes a similar result, but does so using only measurement of moment to iteratively infer successive contact point locations.

6.2 Longitudinal Slip

As explained in Chapter 4, there are two distinct ways whiskers can slip along an object in the context of whisking behavior. *Lateral* slip occurs when the object surface at the contact point is slanted relative to the plane of rotation and the angle of the friction cone is not large enough to

prevent out-of-plane movement, as depicted in Figure 4.1(a). Lateral slip can be detrimental to the process of radial distance extraction, and Chapter 4 developed a method to passively account for it to enable radial distance extraction. *Longitudinal slip* occurs when the contact point moves along the length of the whisker. In the absence of lateral slip, longitudinal slip ensues immediately following contact if the curvature of the object within the plane of rotation at the contact point is finite (not an edge or a point), as depicted in Figure 4.1(b). It also occurs during contact with point-objects for larger whisks. Kaneko *et al*. showed that (in the absence of lateral slip) longitudinal slip has a small effect on distance extraction unless the object curvature is low or the contact point is close to the base [68]. Conveniently, longitudinal slip affords the opportunity to sense additional contact points as the whisker slips along the object periphery, providing further information about object shape over a single whisk. The algorithm presented here accomplishes this task.

6.3 Approach

6.3.1 Determining the Initial Contact Point

We assume the environment contains only static, rigid objects (rigid relative to the whisker), and that the whisker bends only within its plane of rotation. Note that the latter assumption prohibits this method from working when surface contact conditions cause lateral slip to occur [68] (see Discussion section).

The sensing process begins with the whisker freely whisking in the air. When a small moment threshold M_{thresh} is exceeded, the first step is to estimate the radial distance to the first contact point r_0, using:

$$r_0 = 3EI \frac{\theta_0}{M_0}$$

(6.1)

where E is the elastic modulus, I is the area moment of inertia, θ_0 is a small pushing angle (typically about 3°) beyond initial contact (where M_{thresh} is reached), and M_0 is the moment sensed at the whisker base. Calculation of the contact point location in Cartesian coordinates with respect to the base is useful:

$$\begin{bmatrix} d_{x_0} \\ d_{y_0} \end{bmatrix} = \begin{bmatrix} r_0 \\ -r_0 \cdot \theta_0 \end{bmatrix}$$

(6.2)

Figure 6.1 shows the state of the whisker after measurement of the first contact point. As the whisker continues to rotate against the object and θ_0 increases, the contact point will slip along the length of the whisker in a way that depends on the local shape of the object. The sweeping algorithm is designed to infer that local shape based on the continued measurement of moment, as outlined in the following section.
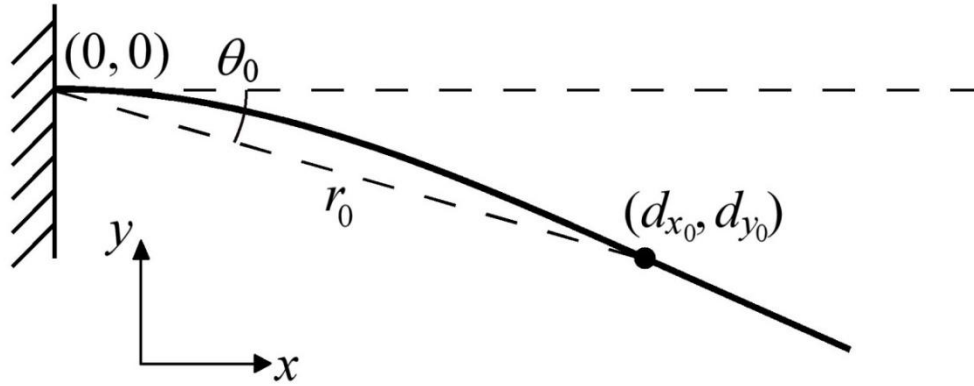
Figure 6.1: Geometry of whisker after rotation by θ_0. The *x*-axis of the coordinate system is coincident with the line tangent to the whisker base. The magnitude of θ_0 is exaggerated here, as 3° is typically sufficient.

6.3.2 Determining Additional Contact Points

The basic premise of the algorithm is that given the current (iteration i, $i \geq 1$) estimated contact point location relative to the base (d_{x_i}, d_{y_i}), its new position after a small incremental rotation $d\theta$ can be inferred based on the new measured moment M_{i+1}. The derivation begins by decomposing the translation of the contact point during $d\theta$ into two components: a nominal deflection $\overline{\delta}_i$ concentric with the whisker base (angle θ_i), and a component $\overline{ds}_i$ parallel to the longitudinal axis at the contact point (angle γ_i) and towards the base, as depicted in Figure 6.2. Hence, we have

$$\begin{bmatrix} d_{x_{i+1}} \\ d_{y_{i+1}} \end{bmatrix} = \begin{bmatrix} d_{x_i} \\ d_{y_i} \end{bmatrix} + \overline{\delta}_i + \overline{ds}_i \tag{6.3}$$
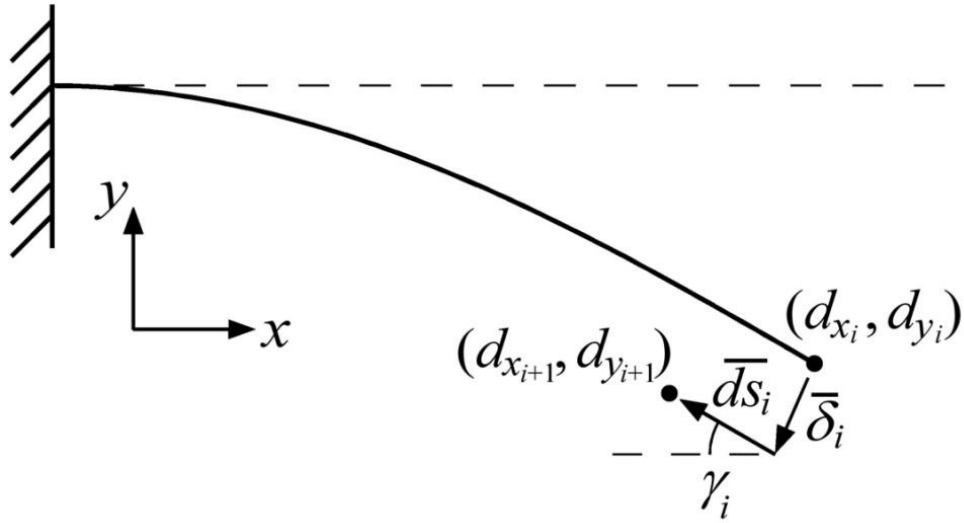
Figure 6.2: Illustration of a single iteration of the sweeping algorithm. The magnitude of $d\theta$ is exaggerated here, as ~1° is typically used.

The result of the $\bar{\delta}_i$ component is immediately evident, shifting the contact point by magnitude $r_i \cdot d\theta$ concentric with the base, allowing us to write:

$$\bar{\delta}_i = -r_i \cdot d\theta \cdot \begin{bmatrix} \sin\theta_i \\ \cos\theta_i \end{bmatrix} \tag{6.4}$$

Determination of $\overline{ds}_i$, however, involves greater effort in finding both its direction and magnitude. These two problems will now be treated independently.

As stated earlier, $\overline{ds}_i$ is oriented parallel to the longitudinal axis of the whisker at the contact point, at angle γ_i. For small θ, it is straightforward to show using Euler-Bernoulli beam theory applied to the classical model of a cantilever beam with concentrated end load, that

$$\gamma = \tfrac{3}{2}\theta \tag{6.5}$$

for small deflections. However, assumptions of linearity become violated for angles larger than about $\sim14°$, and hence we turn to a numerical elastica model to compute the relation between γ and θ for larger deflections.

The model considers a static cantilever beam divided into n nodes, with a concentrated load F at arc length $s = 1$ along the beam. Friction is assumed to be zero, and hence the force acts perpendicular to the longitudinal axis at the force location. Starting at node 1 where the force is applied, the shape of the beam is iteratively computed node-by-node towards node n at the base using a version of the Euler-Bernoulli equation. Repeating this procedure for a range of forces provides a continuum of beam shapes for increasingly large deflections, with units automatically normalized to E, I and s. The resulting table can be efficiently interpolated to generate the beam shape for various methods of query, including (d_x, d_y), (r, θ), and (s, F, EI). Details can be found in Appendix D.

Using the results of the numerical model, Figure 6.3(a) plots γ vs. θ for up to $\theta = 60°$. Perhaps surprisingly, (6.5) continues to hold with very high accuracy well past the regime where small angle assumptions are valid. Figure 6.3(b) shows that use of (6.5) results in only 0.35% error at $\theta = 30°$, and 1.63% error at $\theta = 60°$. Since sweeps of less than 60° are likely to be used in practice, (6.5) is a very good approximation even for large angles and thus is used to estimate the orientation of $\overline{ds_i}$.
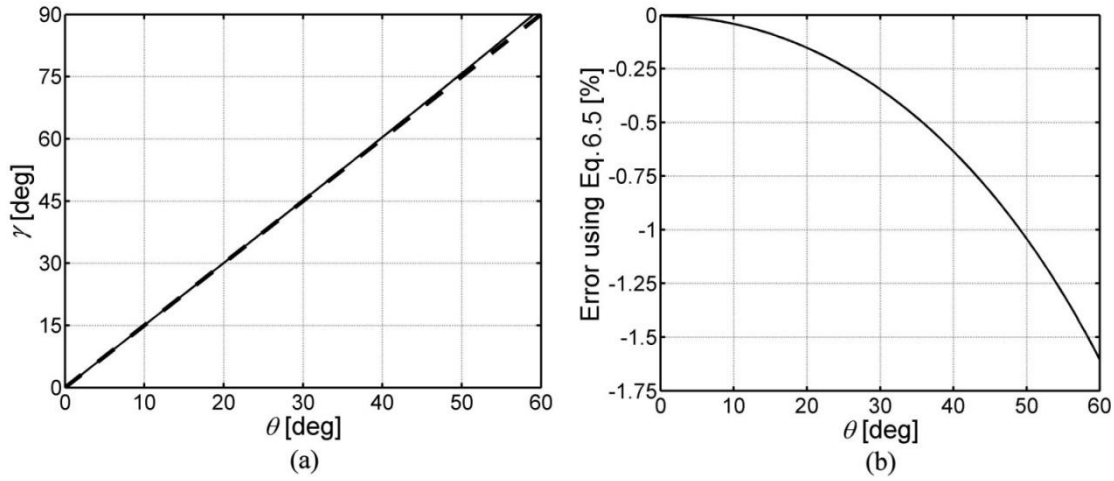
Figure 6.3: (a) Relationship between deflection angle θ and tip angle γ for a cantilever beam with concentrated end load. The solid line is the numerical result, and the dashed line is from (6.5). **(b)** Error incurred using (6.5) as a function of θ.

The only remaining task is to formulate a method of estimating $\left|ds_i\right|$ – the magnitude of $\overline{ds_i}$ – which (neglecting friction) depends entirely on the curvature of the object surface at the current contact point. If the curvature is infinite (i.e., the contact point is an edge or a point-object), then $\left|ds_i\right| = 0$; otherwise, $\left|ds_i\right| > 0$. Defining M_{δ_i} as the moment and dM_{δ_i}/ds as the rate of change of moment with respect to $\left|ds_i\right|$ (following along the beam towards the base) after deflection δ_i, we can write

$$M_{i+1} = M_{\delta_i} + \frac{dM_{\delta_i}}{ds} \cdot \left|ds_i\right| \tag{6.6}$$

And, solving for $\left|ds_i\right|$, we have

$$\left|ds_i\right| = \left(M_{i+1} - M_{\delta_i}\right) \cdot \frac{ds}{dM_{\delta_i}} \tag{6.7}$$

Consolidating (6.5) and (6.7),

$$\overline{ds}_i = \left(M_{i+1} - M_{\delta_i}\right) \cdot \frac{ds}{dM_{\delta_i}} \cdot \begin{bmatrix} -\cos \frac{3}{2}\theta_i \\ \sin \frac{3}{2}\theta_i \end{bmatrix} \tag{6.8}$$

Finally, combining (6.3), (6.4) and (6.8), we have

$$\begin{bmatrix} d_{x_{i+1}} \\ d_{y_{i+1}} \end{bmatrix} = \begin{bmatrix} d_{x_i} \\ d_{y_i} \end{bmatrix} - r_i \cdot d\theta \cdot \begin{bmatrix} \sin \theta_i \\ \cos \theta_i \end{bmatrix} + \left(M_{i+1} - M_{\delta_i}\right) \cdot \frac{ds}{dM_{\delta_i}} \cdot \begin{bmatrix} -\cos \frac{3}{2}\theta_i \\ \sin \frac{3}{2}\theta_i \end{bmatrix} \tag{6.9}$$

Since M_{i+1} is measured by the torque sensor, there are only two remaining unknown variables needed to find the new contact point: M_{δ_i} and dM_{δ_i}/ds. Again, the numerical model provided in the Appendix is utilized, and the results are shown in Figure 6.4.
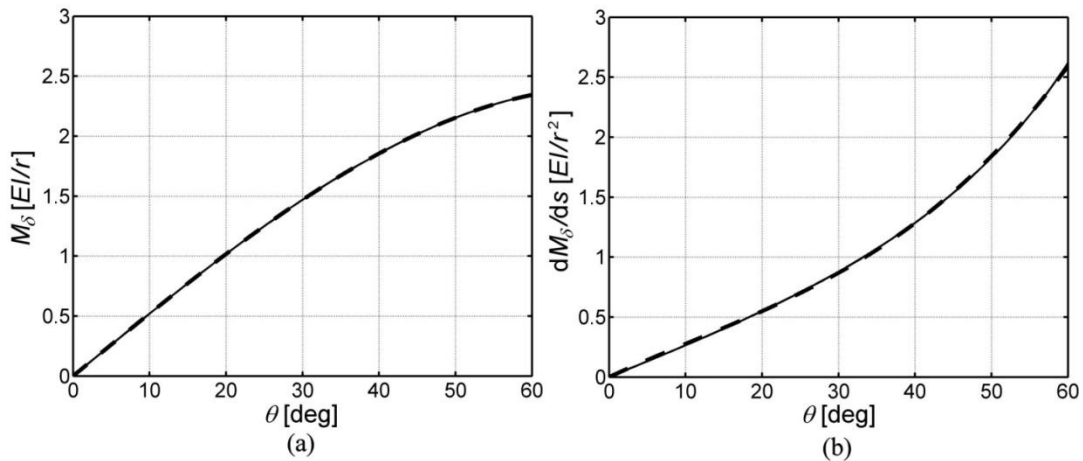
Figure 6.4: The numerical elastica model (see Appendix D) provides the relationship between θ and **(a)** M_δ and **(b)** dM_δ/ds, required by the sweeping algorithm. The solid lines are the numerical data, and the dashed lines are the results of cubic polynomial fits.

The curves are normalized using r as a scaling parameter, so that M_{δ_i} has units of $[EI/r]$, and dM_{δ_i}/ds has units of $[EI/r^2]$. Also shown are the results of cubic polynomial fits to both curves (dashed lines), which serve as convenient methods of implementing these relations. The

polynomials contain no constant term since the underlying function passes through zero, and were fit by minimizing the sum of squared errors. The resulting equations are as follows:

$$M_{\delta_i} = \frac{EI}{r_i} \cdot \left(-0.6673 \cdot \theta_i^3 - 0.0354 \cdot \theta_i^2 + 3.0069 \cdot \theta_i \right) \tag{6.10}$$

$$\frac{dM_{\delta_i}}{ds} = \frac{EI}{r_i^2} \cdot \left(1.5289 \cdot \theta_i^3 - 0.8402 \cdot \theta_i^2 + 1.6799 \cdot \theta_i \right) \tag{6.11}$$

where θ is in units of radians and $r_i = \sqrt{d_{x_i}^2 + d_{y_i}^2}$. Note that (6.10) and (6.11) have the relevant normalization factors included, but also that bending stiffness EI may not be obtainable with high precision. In practice, it is not necessary to know EI, as the torque sensor is calibrated to units of curvature at the whisker base (e.g., from voltage), in which case EI effectively becomes 1. This is addressed further in the Results section.

6.4 Results

The algorithm was tested using aluminum bars with circular-, hexagonal- and square-shaped cross-sections. The robotic whisker used in these experiments was described in Chapter 4 (0.5 mm in diameter, 5 cm in length, and composed of superelastic Nitinol). Although the follicle is capable of sensing both orthogonal components of moment, no lateral slip occurred in these experiments and hence only two of the four strain gages were utilized. The centers of the test objects were placed 4 cm in front of the whisker base, as shown in Figure 6.5.
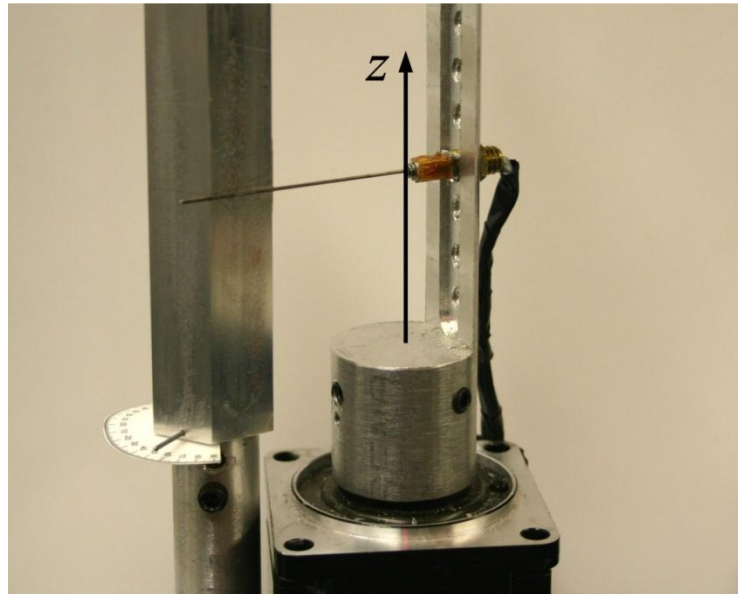
Figure 6.5: The experimental setup. The whisker was rotated against aluminum bars with circular-, hexagonal- and square-shaped cross-sections (hexagonal shown here). The vertical arrow indicates the axis of rotation. The protractor shown underneath the object was used to manually set its orientation.

Calibration of the whisker signal was undertaken before the actual experiments. Throughout this paper, the moment at the whisker base has been referred to as the variable measured by the torque sensor. The Euler-Bernoulli equation (D.1) reveals that curvature is proportional to moment for an inherently straight beam, related by the bending stiffness *EI*. In practice, it is more convenient to calibrate the follicle to curvature instead of moment, because this requires no knowledge of *EI*. We generally refer to the moment at the base instead of curvature because it is somewhat more intuitive, but these units of measure are effectively equivalent in this particular context.

The follicle was calibrated by rotating the whisker at a speed of 10 deg/s through an amplitude of 60° against a slender peg at a radial distance of 4 cm (starting out barely touching). The data were low-pass filtered at 800 Hz, sampled at 2000 Hz, and passed through a zero-phase

digital filter with a cutoff frequency of 10 Hz. Using (6.10) with *EI* set to 1 allows the true curvature to be inferred for all values of θ. Plotting curvature vs. voltage generates a calibration curve, which was stored as a spline, to be used to convert the experimental data from voltage to curvature. The curve starts out linear, but levels off slightly as the curvature becomes large.

Each experimental trial occurred as follows. The whisker starts at rest, oriented $-30°$ relative to the object's center. At a speed of 10 deg/s, it whisks against the object with an amplitude of $60°$, immediately retracting back to $-30°$, and then rests for 5 seconds while the object is rotated about its center by $30°$. This procedure occurred a total of 12 times, resulting in all or almost all of the objects' perimeters to be contacted by the whisker. Although in actuality we are keeping the location of the whisker base fixed in space and rotating the object between whisks, this is functionally equivalent to having the whisker base move around the fixed object between whisks, in a circular matter.

After filtering the data, (6.1) and (6.2) were used to compute the initial contact point using $\theta_0 = 3°$. Subsequent points were generated by iteratively applying (6.9), (6.10) and (6.11), with $d\theta = 1°$. This procedure gives the contact points within the local whisker reference frame (see Figure 6.2); hence conversion to a global frame was necessary before plotting. The results, shown in Figure 6.6(a-c), show that the sweeping algorithm accurately estimates successive contact points as the whisker slips along the perimeters of all three shapes.

The most noteworthy assumption implicit in the sweeping algorithm is that of no friction between the whisker and the object, which influences (6.5), (6.10) and (6.11). These equations were derived under the assumption that the direction of the contact force is normal to the whisker at the contact point, which is increasingly inaccurate for a rough object as θ becomes large. To

test the effect of friction, the experiments were repeated with 120 grit (moderately rough) adhesive-backed sandpaper stuck to the objects. Figure 6.6(d-f) shows that although some precision is lost, the general object profile shapes are again faithfully reproduced.
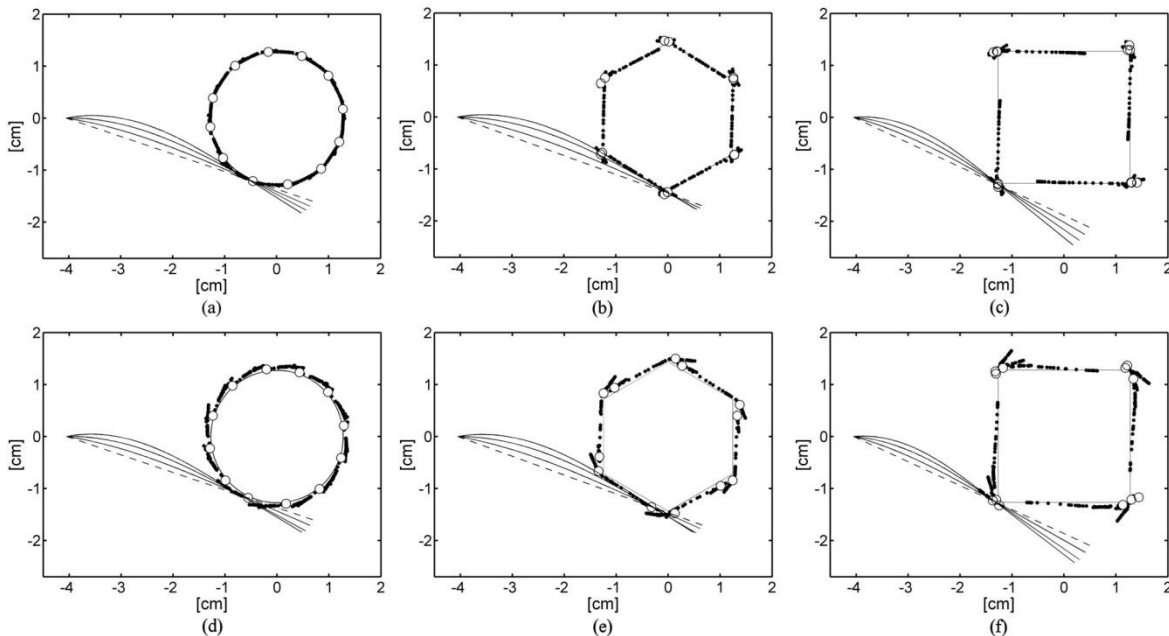
Figure 6.6: Results of implementing the sweeping algorithm on smooth **(a)** circular, **(b)** hexagonal, and **(c)** square objects, and rough **(d)** circular, **(e)** hexagonal, and **(f)** square objects. A total of 12 whisks were performed at evenly-spaced (30°) intervals around the objects. Initial contact points are indicated by small white circles, and subsequent points computed by the sweeping algorithm are smaller black dots. Thin lines indicate the actual underlying shape profile. For the first whisk, the orientation of the whisker upon object contact is indicated by the dashed line, and subsequent whisker shapes are indicated in 10° increments by solid lines. These shapes were generated using the numerical model in Appendix D. This was done for illustrative proposes, and is not required by the sweeping algorithm.

6.5 Discussion

The sweeping algorithm presented here has been shown to be highly accurate for three distinct 2-D shapes. In all three cases, the entire profile shape was reliably extracted with only 12

whisks, clearly providing significant additional shape information beyond that provided by the initial contact point alone, as shown in Figure 6.6. In addition, visual observation showed that the sequence of extracted points seemed to closely match the actual movement of the whisker along the object. In several cases, the whisker remained in discrete contact with an edge during the whisk. As expected, the estimated contact points would remain in the same region, usually within a range of 2 mm from the first contact point for the smooth objects. In other cases, significant slip along the object occurred, whereupon the estimated contact points would accurately align with the side of the object.

When using the algorithm, the user must choose reasonable values for M_{thresh}, θ_0 and $d\theta$. M_{thresh} should be as close to zero as possible while ensuring it won't be exceeded due to the combination of dynamic effects and sensor noise. A good rule-of-thumb is to make θ_0 as small as possible, while still ensuring a strong enough torque signal to allow accurate distance extraction when contact occurs near the whisker tip. The choice of $d\theta$ is predicated on a tradeoff between accuracy and computational efficiency, as well as the desired number of extracted points. Decreasing $d\theta$ below 1° has an insignificant effect on the accuracy of the algorithm. In fact, good accuracy can be obtained for $d\theta$ as large as ~5°.

Another important issue involves the whisking speed. The experiments undertaken here used a very slow speed (10 deg/s) to minimize dynamic effects, but much faster speeds may be implemented in practice. The above experiments were repeated using a whisking speed of 90 deg/s with nearly equally accurate results for both the smooth and rough surfaces (data not shown). The only significant difference involved a greater dispersion of contact points at the edges of the smooth objects.

The assumptions inherent in the sweeping algorithm deserve careful consideration:

- friction – Although the assumption of zero friction is not technically valid if the surface is rough, we have shown that the sweeping algorithm produces good results even in the relatively extreme case of 120 grit sandpaper. Hence, the model has proven to work in the presence of friction, but with somewhat reduced accuracy.

- tip contact – For distance extraction (6.1), tip contact is easily handled by setting an upper threshold on r_0 equal to the length of the whisker (see Chapter 5). However, the assumption that the contact force acts normal to the whisker at the contact point can be inaccurate in the case where the whisker touches the object at the tip, and also the tip can slide along the object, invalidating (6.4). We implemented a modified version of the sweeping algorithm for the case of tip contact, setting $\overline{ds_i}$ to zero (since tip contact generally persists during a whisk), and using a numerical technique to estimate $\overline{\delta_i}$ based on the moment M_{i+1}. Unsatisfactory results were achieved, likely due to the non-perpendicular inclination of the contact force. Therefore, in practice, the sweeping algorithm should be halted for whisks in which r_0 is equal to the whisker length.

- lateral slip – The model explicitly assumes that no lateral slip occurs; any significant amount is likely to be highly detrimental. Note that this does not necessitate that the surface is oriented exactly perpendicular to the plane of rotation, as friction can prevent lateral slip in some cases (see Chapter 4). When lateral slip does occur, it can easily be sensed through measurement of the orthogonal (y) component of moment, in which case either the sweeping algorithm could be halted until the next whisk, or the plane of rotation could be actively adjusted to prevent lateral slip from occurring [68, 71].

- single-point contact – Two distinct cases are possible.

  1. If the whisker contacts the object at two discrete points during its initial rotation θ_0, distance extraction using (6.1) can be affected. However, this situation is unlikely to occur because it would require the precise alignment of two points along the object to coincide with the orientation of the whisker upon contact. Moreover, we found that the sweeping algorithm is able to quickly dampen-out error associated with the use of (6.1). To show this, we processed the experimental data, except set r_0 to an arbitrary value instead of using (6.1). After an additional rotation of about $5°$, subsequent extracted points aligned accurately along the objects.

  2. During a whisker sweep, the whisker may come in contact with the object along a continuous segment of its length, inconsistent with the discrete contact model. This situation clearly occurred in the experiments for both the hexagon and square objects, yet it did not seem to adversely affect the results.

- object compliance – If the object is not rigid relative to the stiffness of the robotic whisker(s), computation of r_0 using (6.1) and the $\bar{\delta}_i$ components using (6.4) during a sweep may be inaccurate. A method for finding r_0 is offered by [68] which involves whisking at two different distances. Although further research would be required to accommodate the sweeping algorithm, the most straightforward solution is to use thin, flexible robotic whiskers.

It is worth drawing some comparisons between the sweeping algorithm developed here, and that implemented by Scholz and Rahn [70]. The latter method uses a hub load cell and a

nonlinear elastica model to numerically integrate the shape of the whisker each time step. There are two drawbacks to this method. First, it requires a sensor that can measure two components force in addition to moment, which is prohibitively bulky and expensive for use in an array of whiskers. Second, it requires the entire shape of the whisker to be numerically computed each time step, which can require significant computational resources, especially for multiple whiskers. In contrast, the algorithm presented here computes contact points by iteratively inferring position changes based on small successive increments in whisker angle θ and sensed moment M. This makes it extremely efficient, involving only the evaluation of a simple algebraic expression and two polynomials per time step. Also, because the follicle needs to only measure moment, it can be based on a single strain gage or other basic technology. The principal limitation of this method at the moment is that it loses significant accuracy when contact occurs at the tip, unlike [70].

Although the sweeping algorithm has been derived for cylindrically-shaped whiskers, it is not limited to this case. Since real rat whiskers are more accurately described as cone-shaped (linearly tapering from base to tip; see Chapter 3), it is interesting to ask whether this method could work for a conical whisker. Theoretically, the answer is yes. Equation (6.1) would simply be replaced with the distance extraction equation for a conical whisker ((3.7)). However, γ, M_{δ} and dM_{δ}/ds would now also depend on the normalized contact distance (r/L_{BT}, where L_{BT} is the linear base-to-tip length of the whisker) in addition to θ, due to the varying whisker diameter along the length. As a result, (6.5), (6.10) and (6.11) would have to be replaced with functions of two variables − θ and r/L_{BT} − which could be generated using the numerical method in

Appendix D and stored using any convenient function approximator, e.g. two-variable polynomial, look-up table, radial basis function network, or multilayer perceptron.

Future research is warranted to develop a strategy for dealing with tip contact. Another interesting possibility is to expand the algorithm to allow continued estimation of contact point location during lateral slip. Chapter 4 presented a method for distance extraction during lateral slip, so much of the puzzle has already been addressed. Development of such a 3-D version of the sweeping algorithm described here that incorporates a 2-D moment sensor would be of great benefit to the ultimate goal of quick and precise object feature extraction with a robotic whisker array.

6.6 Conclusion

This chapter has derived and demonstrated an effective, efficient and easy-to-implement method for obtaining object profile shape information over a single whisk with a robotic whisker. The fact that only moment needs to be measured allows it to be implemented with small, inexpensive torque sensors (e.g. strain gages), making it highly amenable to implementation on an array of robotic whiskers. The algorithm was shown to be robust with regard to sensor noise and object friction.

The extraction of a continuous segment of an object's profile with a single whisker/whisk is also somewhat biologically plausible, in that the shape could be inferable through torque information gathered with a tapered rat whisker during a sweep. In fact, the taper of the whisker would serve to increase the length of the segment swept over, as the whisker would increasingly

tend to bend in on itself for contact near the tip. Although "sensor noise" would be a significant

limiting factor in the rat, it is conceivable that basic curvature information could be extracted.

Chapter 7

Discussion and Conclusion

This chapter contains material that has been slightly altered from the following publication:

J. H. Solomon and M. J. Hartmann, "Robotic whiskers used to sense features," *Nature,* vol. 443, p. 525, Oct. 5 2006.

7.1   Summary of Results

The goal of this thesis has been to gain insight into the functional principles that underlie tactile sensing in the rat whisker system. The approach centered around the development of mechanical models − analytical, numerical and robotic − to understand how the fundamental coupling of movement (whisking) and sensing (moment) can allow extraction of object shape. Referring back to Figure 1.1, we may now reflect upon how this multifaceted approach has facilitated the both the development and validation of ideas.
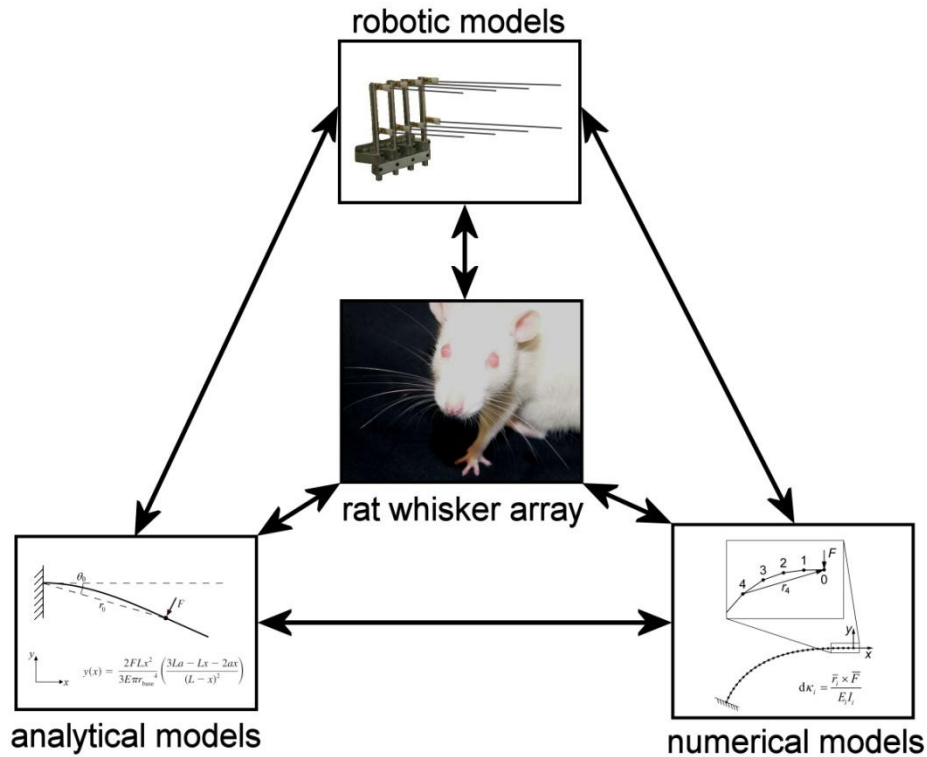
Figure 1.1: The synergistic interactions between analytical, numerical and robotic modeling techniques led to new insights about the rat whisker system.

Following the arrows in Figure 1.1, the analytical models were used to:

1. explicate how external forces and imposed deflections cause a rat whisker to bend and mechanically react at the base where the bending moment (and/or its derivative) can be sensed by mechanoreceptors surrounding the follicle, yielding a functional theory for how the rat might be extracting object features. (Chapter 3)

2. explicate how external forces and imposed deflections cause a robotic whisker to bend and mechanically react at the base where the bending moment can be sensed by an artificial follicle, yielding a method for distance extraction analogous to 1 that is tailored to a robotic platform. (Chapters 4, 5 and 6)

3. validate the numerical models for small deflections. (Chapters 3 and 6)

The numerical models were used to:

1. compute how rat whiskers bend and transmit moment in instances where assumptions the analytical models are invalid. (Chapter 3)

2. develop a novel "sweeping" algorithm for feature extraction with a robotic platform. (Chapter 6)

3. elucidate the effects of inherent whisker curvature on the analytical models. (Chapter 3)

The robotic models were used to:

1. test and validate theoretical methods for object feature extraction by the rat whisker system in the real world where sensor noise and unmodeled dynamics exist, and important assumptions may be violated. (Chapters 4, 5, 6)

2. validate assumptions of the analytical models. (Chapters 4, 5 and 6)

3. validate assumptions of the numerical models. (Chapter 6)

7.2   Alternative Methods for the Estimation of Radial Contact Distance

There are at least five alternative methods to those presented here for computing radial contact distance using sensors only at the whisker base.

1. Measure force and moment simultaneously [70] and then calculate the distance d using $d = M / F$. In practice, however, the simultaneous, independent measurement of force and moment is extremely difficult. Multi-axis sensors that can provide independent measurements of moment and force are prohibitively bulky and expensive for small-scale

whisker arrays, and it is highly unlikely that biological sensors in the follicle can measure the two quantities independently.

2. Measure the normal component of force on the whisker, and use it to estimate the distance to the object using:

$$d = \frac{\sqrt{C\dot{\theta}\left(C\dot{\theta} + 4\dot{F}L^2\right)} - C\dot{\theta}}{2\dot{F}L} \tag{7.1}$$

where the time derivatives are included for biological plausibility. This equation is analogous to (3.7), and can be derived by plugging $\dot{M} = d \cdot \dot{F}$ into (3.7).

For a cylindrical (robotic) whisker, this equation becomes

$$d = \sqrt{C\frac{\dot{\theta}}{\dot{F}}} \tag{7.2}$$

which is analogous to (6.1). Again, since measurement of moment is more plausible in the rat and straightforward in a robot, this method is not of much practical significance.

3. If the whisker is tapered (i.e., a rat whisker), then the longitudinal component of force after a small rotation θ against the object monotonically depends on radial distance [78], and hence could be used to estimate the radial distance. Note that the inherent whisker curvature would help to accentuate this relationship.

4. Measure the vibrations associated with collision and correlate them with object distance [67]. However, vibrations alone are unlikely to permit the rat to determine radial distance for two reasons: 1) Previous work has shown that whiskers are quite damped, limiting the amplitude and duration of any signals transmitted to the base. This means that if there is any noise in the signal, it will be difficult to obtain an accurate estimate of object

distance. In contrast, if whisking velocity is constant (a good approximation for the real rat), $\dot{M}$ will be constant for a fraction of the whisk. This means the rat has a comparatively long time to take an average measurement of $\dot{M}$ and $\dot{\theta}$, and thus obtain a robust estimate for object distance. 2) Vibrations due to object contact would likely overlap with those caused by object texture [79], thus generating a signal that contains ambiguous information about texture and distance.

5. Movement of the entire follicle-whisker complex could be obstructed in a distance-dependent manner, or sling-muscle force could likewise vary with radial contact distance. Cells responsive to these phenomena could thus encode contact distance [74].

Given all these possible alternative methods for radial distance extraction, why single out the one focused upon here in this thesis as the one used by the rat? Recent studies have confirmed that some primary sensory neurons in the trigeminal ganglion spike as would be expected if they were primarily responding to the rate of change in bending moment at the whisker base [36, 38]. Moreover, these results are not surprising. Torque (moment) is much easier to measure in engineered systems because it directly corresponds to mechanical states, such as the bending of a strain gage on a surface or the current running through an electric motor. In an analogous way, it is reasonable to suggest that the bending of mechanoreceptors or the tension within intrinsic muscles are used to measure moment. On the other hand, as nervous systems are renowned for exploiting all available information, vibrations, force and moment may all play roles in distance extraction.

It should be mentioned that this thesis does not postulate that rats *explicitly* attempt to estimate the positions of contact points with the object for every whisker during every whisk.

Instead, the goal has been to identify the relevant variables involved in tactile sensation with the rat whisker system, to systematically elucidate how these variables relate to the movement and deflection of the whiskers against the object being sensed, and to show how measurement of these variables provides the information necessary to infer shape. It is expected that neural correlates to these concepts will continue to be found as neuroscientists continue to study the whisker system, perhaps with the aid of this research.

7.3 Conclusion

The rat whisker system is an amazing sensory modality. Although the whiskers are few in number and whisking movements are rhythmic and stereotyped, the acute sensitivity of this system rivals that of the human fingertip [24]. This unique juxtaposition of simplicity and complexity has proven difficult for scientists to understand, but great progress is being made. This thesis approached the problem using engineering-oriented techniques, including the synergistic use of analytical, numerical and robotic models. The equations and concepts that have been developed may help researchers to understand the relationships between the ways whiskers deform during whisking, and the corresponding responses of sensory neurons. The use of robots as research tools is continuing to gain traction within the scientific community [13, 15, 56, 61]. This biorobotic approach is not only useful for testing hypotheses that are difficult or impossible to address through other means, but also can produce innovative new technologies that borrow from the intricate and elegant principles of movement and sensing in animals.

References

[1]   D. M. Fragaszy and S. Perry, *The Biology of Traditions: Models and Evidence*: Cambridge University Press, 2003.

[2]   G. T. Prusky, P. W. R. West, and R. M. Douglas, "Behavioral assessment of visual acuity in mice and rats," *Vision Research,* vol. 40, pp. 2201-2209, 2000.

[3]   W. I. Welker, "Analysis of sniffing of the albino rat," *Behaviour,* vol. 22, pp. 223-244, 1964.

[4]   M. Brecht, B. Preilowski, and M. M. Merzenich, "Functional architecture of the mystacial vibrissae," *Behavioural Brain Research,* vol. 84, pp. 81-97, 1997.

[5]   G. E. Carvell and D. J. Simons, "Task-Related and Subject-Related Differences in Sensorimotor Behavior During Active Touch," *Somatosensory and Motor Research,* vol. 12, pp. 1-9, 1995.

[6]   S. B. Vincent, "The tactile hair of the white rat," *Journal of Comparative Neurology,* vol. 23, pp. 1-38, 1913.

[7]   M. J. Hartmann, "Active sensing capabilities of the rat whisker system," *Autonomous Robots,* vol. 11, pp. 249-254, Nov. 2001.

[8]   T. A. Woolsey and H. Van der Loos, "The structural organization of layer IV in the somatosensory region (SI) of mouse cerebral cortex. The description of a cortical field composed of discrete cytoarchitectonic units," *Brain Research,* vol. 17, pp. 205-242, 1970.

[9]   J. W. Haefner, *Modeling Biological Systems: Principles and Applications*, 2nd ed. New York: Springer, 2005.

[10]   W. Silvert, "Modeling as a Discipline," *International Journal of General Systems,* vol. 30, pp. 261-282, 2000.

[11]   B. Webb and T. R. Consi, *Biorobotics*: AAAI Press, 2001.

[12]   K. Nishikawa, A. A. Biewener, P. Aerts, A. N. Ahn, H. J. Chiel, M. A. Daley, T. L. Daniel, R. J. Full, M. E. Hale, T. L. Hedrick, A. K. Lappin, T. R. Nichols, R. D. Quinn, R. A. Satterlie, and B. Szymik, "Neuromechanics: an integrative approach for understanding motor control," *Integrative and Comparative Biology,* vol. 47, pp. 16-54, 2007.

[13]   R. D. Beer, H. J. Chiel, R. D. Quinn, and R. E. Ritzmann, "Biorobotic approaches to the study of motor systems," *Current Opinion in Neurobiology,* vol. 8, pp. 777-782, December 1998.

[14]   M. H. Lee, "Tactile sensing: New directions, new challenges," *The International Journal of Robotics Research,* vol. 19, pp. 636-643, 2000.

[15]   M. Fend, S. Bovet, and V. V. Hafner, "The artificial mouse - A robot with whiskers and vision," in *Proceedings of the 35th International Symposium on Robotics (ISR)*, Paris, 2004.

[16]   D. Jung and A. Zelinsky, "Whisker based mobile robot navigation," in *Proceedings of the 1996 IEEE/RSJ International Conference on Intelligent Robots and Systems*, 1996, pp. 497-504.

[17]   H. Haidarliu and E. Ahissar, "Size gradients of barreloids in the rat thalamus," *Journal of Comparative Neurology,* vol. 429, pp. 372-387, 2001.

[18]   J. Dorfl, "The musculature of the mystacial vibrissae of the white mouse," *Journal of Anatomy,* vol. 135, pp. 147-154, 1982.

[19]   V. Gopal, J. H. Solomon, N. Naik, and M. J. Z. Hartmann, "Two and three dimensional morphology of the rat vibrissal array," *Annals of Biomedical Engineering,* accepted with revisions.

[20]   M. Do Carmo, *Differential Geometry of Curves and Surfaces*: Prentice Hall, 1976.

[21]   S. B. Vincent, "The function of the vibrissae in the behavior of the white rat," *Behavioral Monographs,* vol. 1, pp. 7-85, 1912.

[22]   M. L. Andermann, J. Ritt, M. A. Neimark, and C. I. Moore, "Neural correlates of vibrissa resonance: Band-pass and somatotopic representation of high-frequency stimuli," *Neuron,* vol. 42, pp. 451-463, 2004.

[23]   G. E. Carvell and D. J. Simons, "Biometric analyses of vibrissal tactile discrimination in the rat," *Journal of Neuroscience,* vol. 10, pp. 2638-2648, 1990.

[24]   E. Guic-Robles, C. Valdivieso, and G. Guajardo, "Rats can learn a roughness discrimination using only their vibrissal system," *Behavioural Brain Research,* vol. 31, pp. 285-289, 1989.

[25]   F. L. Rice, B. T. Fundin, J. Arvidsson, H. Aldskogius, and O. Johansson, "Comprehensive immunofluorescence and lectin binding analysis of vibrissal follicle sinus complex innervation in the mystacial pad of the rat," *Journal of Comparative Neurology,* vol. 385, pp. 149-184, 1997.

[26]   S. Ebara, K. Kumamoto, T. Matsuura, J. E. Mazurkiewicz, and F. L. Rice, "Similarities and differences in the innervation of mystacial vibrissal follicle-sinus complexes in the rat and cat: A confocal microscopic study," *Journal of Comparative Neurology,* vol. 449, pp. 103-119, Jul 22 2002.

[27]   T. M. Mosconi, F. L. Rice, and M. J. Song, "Sensory innervation in the inner conical body of the vibrissal rollicle-sinus complex of the rat," *Journal of Comparative Neurology,* vol. 328, pp. 232-251, 1992.

[28]   M. A. Neimark, M. L. Andermann, J. J. Hopfield, and C. I. Moore, "Vibrissa resonance as a transduction mechanism for tactile encoding," *Journal of Neuroscience,* vol. 23, 2003.

[29]   M. J. Hartmann, N. J. Johnson, R. B. Towal, and C. Assad, "Mechanical characteristics of rat vibrissae: Resonant frequencies and damping in isolated whiskers and in the awake behaving animal," *Journal of Neuroscience,* vol. 23, pp. 6510-6519, 2003.

[30]   D. Krupa, M. Matell, A. Brisben, L. Oliveira, and M. A. L. Nicolelis, "Behavioral properties of the trigeminal somatosensory system in rats performing whisker-dependent tactile discriminations," *Journal of Neuroscience,* vol. 21, pp. 5752-5763, 2001.

[31]   L. Euler, *Eneström Number 65: Methodus inveniendi lineas curvas maximi minimive proprietate gaudentes, sive solutio problematis isoperimetrici lattissimo sensu accepti (A method for finding curved lines enjoying properties of maximum or minimum, or solution of isoperimetric problems in the broadest accepted sense)*. Lausannæ, Genevæ: Marcum-Michaelem Bousquet & socios, 1744.

[32]   A. E. H. Love, *A Treatise on the Mathematical Theory of Elasticity*, 4th ed. ed. New York: Dover, 1944.

[33]   S. Timoshenko, *Theory of Elasticity*, 3rd ed. ed. New York: McGraw-Hill, 1970.

[34]   W. C. Young and R. Budynas, *Roark's Formulas for Stress and Strain*, 7th ed.: McGraw-Hill Professional, 2001.

[35]   E. Ahissar and A. Arieli, "Figuring space by time," *Neuron,* vol. 32, pp. 185-201, Oct 25 2001.

[36]   M. Szwed, K. Bagdasarian, B. Blumenfeld, O. Barak, D. Derdikman, and E. Ahissar, "Responses of trigeminal ganglion neurons to the radial distance of contact during active vibrissal touch," *Journal of Neurophysiology,* vol. 95, pp. 791– 802, 2006.

[37]   E. Ahissar, R. Sosnik, and S. Haidarliu, "Transformation from temporal to rate coding in a somatosensory thalamocortical pathway," *Nature,* vol. 406, pp. 302-306, Jul 20 2000.

[38]   M. Szwed, K. Bagdasarian, and E. Ahissar, "Encoding of vibrissal active touch," *Neuron,* vol. 40, pp. 621-630, Oct 30 2003.

[39]   M. Shoykhet, D. Doherty, and D. J. Simons, "Coding of deflection velocity and amplitude by whisker primary afferent neurons: implications for higher level processing," *Somatosensory and Motor Research,* vol. 17, pp. 171-180, 2000.

[40]   S. H. Lichtenstein, G. E. Carvell, and D. J. Simons, "Responses of rat trigeminal ganglion neurons to movements of vibrissae in different directions," *Somatosensory and Motor Research,* vol. 7, pp. 47-65, 1990.

[41]   R. M. Webber and G. B. Stanley, "Transient and steady-state dynamics of cortical adaptation," *Journal of Neurophysiology,* vol. 95, pp. 2923–2932, 2006.

[42]   S. C. Leiser and K. A. Moxon, "Relationship between physiological response type (RA and SA) and vibrissal receptive field of neurons within the rat trigeminal ganglion," *Journal of Neurophysiology,* vol. 95, pp. 3129–3145, 2006.

[43]   M. G. Paulin, "System identification of spiking sensory neurons using realistically constrained nonlinear time series models," in *Advances in Processing and Pattern Analysis of Biological Signals*, I. Gath and G. Inbar, Eds. New York: Plenum, 1996, pp. 183-194.

[44]   M. G. Paulin and L. F. Hoffman, "Optimal firing rate estimation," *Neural Networks,* vol. 14, pp. 877-881, 2001.

[45]   M. G. Paulin, L. F. Hoffman, and C. Assad, "Dynamics and the single spike," *IEEE Transactions on Neural Networks,* vol. 15, pp. 987- 994, 2004.

[46]   L. M. Jones, S. Lee, J. C. Trageser, D. J. Simons, and A. Keller, "Precise temporal responses in whisker trigeminal neurons," *Journal of Neurophysiology,* vol. 92, pp. 665-668, Jul 2004.

[47]   J. H. Solomon and M. J. Hartmann, "Robotic whiskers used to sense features," *Nature,* vol. 443, p. 525, Oct. 5 2006.

[48]   M. Scott, "Blood supply of mystacial vibrissae," *Nature,* vol. 175, pp. 395–396, 1955.

[49]   B. Mitchinson, C. J. Martin, R. A. Grant, and T. J. Prescott, "Feedback control in active sensing: rat exploratory whisking is modulated by environmental contact," *Proceedings of the Royal Society B,* vol. 274, pp. 1035-41, 2007.

[50]   E. Zucker and W. I. Welker, "Coding of somatic sensory input by vibrissae neurons in the rat's trigeminal ganglion," *Brain Research,* vol. 12, pp. 138-156, 1969.

[51]   V. Gopal and M. J. Z. Hartmann, "Using hardware models to quantify sensory data acquisition across the rat vibrissal array," *The Journal of Bioinspiration and Biomimetics,* vol. 2, pp. S135-S145, 2007.

[52]   P. M. Knutsen, M. Pietr, and E. Ahissar, "Haptic object localization in the vibrissal system: Behavior and performance," *Journal of Neuroscience,* vol. 21, pp. 8451-8464, 2006.

[53]   S. J. Lederman and R. L. Klatzky, "Hand movements: A window into haptic object recognition," *Cognitive Psychology,* vol. 19, 1987.

[54]   R. A. Brooks, "A robot that walks; emergent behaviors from a carefully evolved network," *Neural Computation,* vol. 1, pp. 253-262, 1989.

[55]   S. Hirose, S. Inoue, and K. Yoneda, "The whisker sensor and the transmission of multiple sensor signals," *Advanced Robotics,* vol. 4, pp. 105-117, 1990.

[56]   M. J. Pearson, A. G. Pipe, C. Melhuish, B. Mitchinson, and T. J. Prescott, "Whiskerbot: A robotic active touch system modeled on the rat whisker sensory system," *Adaptive Behavior,* vol. 15, pp. 223-240, 2007.

[57]   V. V. Hafner, M. Fend, P. König, and K. P. Kording, "Predicting properties of the rat somatosensory system by sparse coding," *Neural Information Processing Letters and Reviews,* vol. 4, pp. 11-18, 2004.

[58]   M. Fend, H. Yokoi, and R. Pfeifer, "Optimal morphology of a biologically-inspired whisker array on an obstacle-avoiding robot," in *Proceedings of the 7th European Conference on Artificial Life*, 2003, pp. 771-780.

[59]   A. E. Schultz, J. H. Solomon, M. J. Peshkin, and M. J. Hartmann, "Multifunctional whisker arrays for distance detection, terrain mapping, and object feature extraction," in *Proceedings of the 2005 IEEE International Conference on Robotics and Automation*, 2005, pp. 2588-2593.

[60]   M. Fend, S. Bovet, H. Yokoi, and R. Pfeifer, "An active artificial whisker array for texture discrimination," in *Proceedings of the 2003 IEEE/RSJ International Conference on Intelligent Robots and Systems*, 2003, pp. 1044-1049.

[61]   J. Hipp, E. Arabzadeh, E. Zorzin, J. Conradt, C. Kayser, M. E. Diamond, and P. König, "Texture signals in whisker vibrations," *Journal of Neuroscience,* vol. 95, pp. 1792-1799, 2006.

[62]   M. Kaneko and T. Tsuji, "A whisker tracing sensor with 5 μm sensitivity," in *IEEE/RSJ International Conference on Intelligent Robots and Systems*, 2000, pp. 3907-3912.

[63] O. Bebek and M. C. Cavusoglu, "Whisker sensor design for three dimensional position measurement in robotic assisted beating heart surgery," in *Proceeedings of the 2007 IEEE International Conference on Robotics and Automation*, 2007, pp. 225-231.

[64] T. Tsujimura and T. Yabuta, "Object detection by tactile sensing method employing force/torque information," *IEEE Transactions on Robotics and Automation,* vol. 5, pp. 444-450, Aug. 1989.

[65] R. A. Russell, "Using tactile whiskers to measure surface contours," in *Proceedings of the 1992 IEEE International Conference on Robotics and Automation*, Nice, France, 1992, pp. 1295-1299.

[66] J. Wilson and Z. Chen, "A whisker probe system for shape perception of solids," *ASME Journal of Dynamic Systems, Measurement, and Control,* vol. 117, pp. 104-108, 1995.

[67] N. Ueno, M. Svinin, and M. Kaneko, "Dynamic contact sensing by flexible beam," *IEEE/ASME Transactions on Mechatronics,* vol. 3, pp. 254-264, Apr. 1998.

[68] M. Kaneko, N. Kanayama, and T. Tsuji, "Active antenna for contact sensing," *IEEE Transactions on Robotics and Automation,* vol. 14, pp. 278-291, Apr. 1998.

[69] R. Russell and J. Wijaya, "Object location and recognition using whisker sensors," in *Proceedings of the 2003 Australian Conference on Robotics and Automation*, 2003.

[70] G. R. Scholz and C. D. Rahn, "Profile sensing with an actuated whisker," *IEEE Transactions on Robotics and Automation,* vol. 20, pp. 124-127, Feb. 2004.

[71] T. N. Clements and C. D. Rahn, "Three dimensional contact imaging with an actuated whisker," *IEEE Transactions on Robotics,* vol. 22, pp. 844-848, 2006.

[72] D. Kim and R. Möller, "Biomimetic whiskers for shape recognition," *Robotics and Autonomous Systems,* vol. 55, pp. 229-243, Mar. 2007.

[73] M. Kaneko, N. Kanayama, and T. Tsuji, "Vision-based active sensor using a flexible beam," *IEEE/ASME Transactions on Mechatronics,* vol. 6, pp. 7-16, 2001.

[74] M. Szwed, D. Derdikman, K. Bagdasarian, and E. Ahissar, "Pre-neuronal encoding of object location by single whiskers," to appear.

[75] S. B. Mehta, D. Whitmer, R. Figueroa, B. A. Williams, and D. Kleinfeld, "Active spatial perception in the vibrissa scanning sensorimotor system," *PLoS Biology,* vol. 5, pp. 1-14, 2007.

[76] R. Bermejo, A. Vyas, and P. Zeigler, "Topography of whisking-I. Two-dimensional monitoring of whisker movements," *Somatosensory and Motor Research,* vol. 19, pp. 341-346, 2002.

[77]   P. Gao, R. Bermejo, and H. P. Zeigler, "Vibrissa deafferentiation and whisking kinematics: Evidence for a whisking "pattern generator"," *Journal of Neuroscience,* vol. 21, pp. 5374-5380, 2001.

[78]   B. W. Quist and M. J. Z. Hartmann, "Quantifying axial forces in the isolated vibrissae," in preparation.

[79]   J. T. Ritt, M. L. Andermann, and C. I. Moore, "Emdodied information processing: Vibrissa mechanics and texture features shape micro-motions in actively sensing rats," *Neuron,* vol. 57, pp. 599-613, 2008.

[80]   L. D. Landau and E. M. Lifshitz, *Theory of Elasticity*, 3rd ed. Oxford, England: Pergamon Press, 1986.

[81]   M. Batista and F. Kosel, "Cantilever beam equilibrium configurations," *International Journal of Solids and Structures,* vol. 42, pp. 4663-4672, 2005.

[82]   S. Navee and R. E. Elling, "Equilibrium configurations of cantilever beams subjected to inclined end loads," *Transactions of the ASME Journal of Applied Mechanics,* vol. 59, pp. 572-579, 1992.

[83]   J. A. Birdwell, J. H. Solomon, M. Thajchayapong, M. A. Taylor, M. Cheely, R. B. Towal, J. Conradt, and M. J. Z. Hartmann, "Biomechanical models for radial distance determination by rat vibrissae," *Journal of Neurophysiology,* vol. 98, pp. 2439-2455, 2007.

Appendix A

Fitting of Whisker Shape

Whiskers from the A, B, C, D and E whisker rows, along with the "straddler" whiskers α, β, γ, and δ, were obtained from both the right and left whisker pads of four adult female Sprague-Dawley rats. All rats had between four and seven whiskers in each of the A-E rows. Each whisker was grasped firmly at the base with tweezers, and plucked from the follicle with a single swift motion. Isolated whiskers were then scanned and digitized at a spatial resolution of ~5 or 13 μm in the *x*-direction and ~5 or 25 μm in the *y*-direction, using either an Epson Perfection 4180 or a UMAX Powerlook 2100 XL scanner (these scanners have different resolutions). These scans were converted to black and white binary images, using either Photoshop version 7.0 or the MATLAB Image Processing Toolbox version 4.2, and all further

analysis was performed with these binary images. A total of 231 whiskers were digitized in this manner.

Figure A.1 shows the outline of a representative binary image of a whisker. At each horizontal (x) position, the midpoint of the upper and lower edges of the whisker was found. These midpoints were connected to obtain a "middle" curve that closely matched the whisker shape. The middle curve is shown in the inset to Figure A.1 as a light gray line, and it can be seen that it is an excellent match to the overall shape of the whisker. For each whisker, the middle curve was used for the analysis of whisker shape.
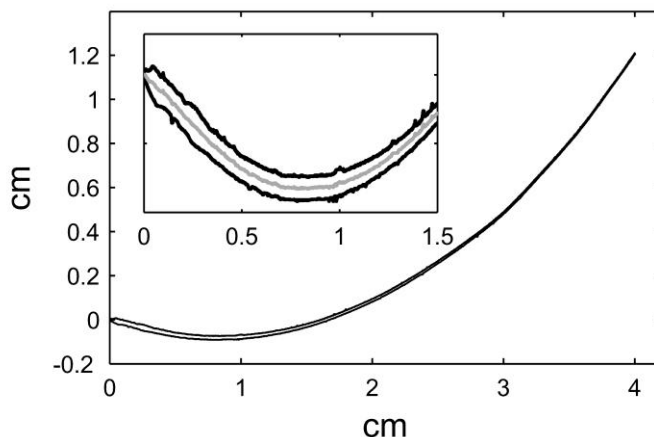
Figure A.1: A typical 2-D scan of a whisker. Each whisker was scanned with its concave side oriented in the positive *y*-direction. The inset shows a magnified portion of the whisker. The light gray line is the "middle whisker," generated by averaging the *y*-values of the upper and lower edges of the whisker at each *x*-position.

To describe whisker shape without reference to Cartesian coordinates, a coordinate-free representation was used. In a coordinate-free representation of a plane curve, one end of the curve is specified as the origin, and the position of any point on the curve is specified by the arc-

length s traveled along the curve from the origin to reach that point [20]. The shape of the curve is then specified by the curvature $\kappa(s)$ at each point as a function of the arc length s, where

$$\kappa = \frac{d\phi}{ds} \qquad (A.1)$$

and ϕ represents the angle of the line tangent to the curve. The curve $\{s, \kappa(s)\}$ can be represented in either a discrete of continuous manner, and transformed to Cartesian coordinates using the following procedure.

First, if $\kappa(s)$ is represented in a continuous form, it is discretized into n nodes. The procedure then begins by placing the first node (x_1, y_1) at the origin of the Cartesian coordinate system and defining the initial tangent line to point along the positive x-axis: $\phi_1 = 0$. This node represents the base of the whisker. Successive node coordinates are then computed by iteratively applying the following equations, starting at $i = 2$ and stopping at $i = n-1$:

$$\phi_i = \phi_{i-1} + \kappa_{i-1} ds \qquad (A.2)$$

$$x_{i+1} = x_i + ds \cos \phi_i \qquad (A.3)$$

$$y_{i+1} = y_i + ds \sin \phi_i \qquad (A.4)$$

As explained in Chapter 2, excellent fits were obtained using a linear parameterization:

$$\kappa(s) = as + b \qquad (2.1)$$

The first step of the fitting process was to divide the whisker into $n = 20$ nodes ($n > 20$ did not significantly affect the fit, but slowed computations). The resulting segments ds were then scaled by the total whisker length L, thus normalizing the total whisker length to unity, and the length of each segment to $ds = 1/(n-1)$. Using (A.1), values of κ for each node except the first and last were computed. Initial values for a and b in (2.1) were then found by performing a linear fit to

the digitized values of {s, $\kappa(s)$} for the whisker using MATLAB's 'polyfit' function. While this minimizes the sum of squared error between the nodes in terms of the curvature at each node, we seek coefficients that lead to an optimal fit in Cartesian space. Therefore, we define our error function as the mean sum of squared Euclidean distances between the nodes on the fit curve and their corresponding nodes on the normalized real whisker. The MATLAB routine 'fminsearch,' which minimizes a function of several variables using the Nelder-Mead simplex algorithm, was used to find the values of a and b that minimized the error function. Initial guesses for the coefficients were based on the values obtained from the curvature-based fits.

Appendix B

Analytical Solution for Deflection of a Conical Beam

This appendix consists of material from the following publication:

J. A. Birdwell, J. H. Solomon, M. Thajchayapong, M. A. Taylor, M. Cheely, R. B. Towal, J. Conradt, and M. J. Z. Hartmann, "Biomechanical models for radial distance determination by rat vibrissae," *Journal of Neurophysiology,* vol. 98, pp. 2439-2455, 2007.

Elasticity equations ([31-34]) relate the curvature κ of a cantilever beam to the moment M at its base:

$$\kappa = \frac{d^2 y}{dx^2} = \frac{M}{EI} \tag{B.1}$$

where

$$M = \begin{cases} F(a-x) & 0 \le x \le a \\ 0 & a \le x \le L \end{cases}$$

In (B.1), F is the force exerted at a distance a from the base of the beam, $y(x)$ is the vertical displacement of the beam at each x (horizontal) location, E is Young's modulus (also called the elastic modulus) and I is the second areal moment of inertia. For a cylinder,

$$I = \frac{\pi r^4}{4} \tag{B.2}$$

For a cone, however, r varies with length as

$$r(x) = r_{base}\left(1 - \frac{x}{L}\right) \tag{B.3}$$

Substituting (B.3) into (B.2) yields

$$I = \alpha(L - x)^4$$

where α is a constant defined as

$$\alpha = \left(\frac{\pi}{4}\right)\left(\frac{r_{base}}{L}\right)^4 \tag{B.4}$$

Inserting expressions for I and M into (B.1) for $x \le a$ gives

$$\frac{d^2 y}{dx^2} = \left(\frac{F}{E\alpha}\right)(a - x)(L - x)^{-4} \tag{B.5}$$

Integrating once with respect to x yields

$$\frac{dy}{dx} = \left(\frac{F}{E\alpha}\right)\left(\frac{1}{2(L - x)^2} - \frac{(L - a)}{3(L - x)^3}\right) + C_1 \tag{B.6}$$

And integrating again with respect to x yields

$$y(x) = \left(\frac{F}{E\alpha}\right)\left(\frac{(a - L)}{6(L - x)^2} - \frac{1}{2(L - x)}\right) + C_1 x + C_2 \tag{B.7}$$

To find the constant of integration C_1 we note that $\dfrac{dy}{dx}$ at $x = 0$ must equal zero, so that (B.6)

becomes

$$0 = \left(\frac{F}{E\alpha}\right)\left(\frac{1}{2(L-x)^2} - \frac{(L-a)}{3(L-x)^3}\right) + C_1 \tag{B.8}$$

Solving for C_1 gives

$$C_1 = \left(\frac{-F(L+2a)}{6E\alpha L^3}\right) \tag{B.9}$$

To find the constant of integration C_2 we note that y at $x = 0$ must equal zero, so that (B.7)

becomes

$$0 = \left(\frac{F}{E\alpha}\right)\left(\frac{(a-L)}{6(L-x)^2} - \frac{1}{2(L-x)}\right) + 0 + C_2 \tag{B.10}$$

Solving for C_2 gives

$$C_2 = \left(\frac{-F(2L+a)}{6E\alpha L^2}\right) \tag{B.11}$$

Substituting our expressions for C_1, C_2 and α back into (B.7) we find

$$y(x) = \frac{2FL^4}{3E\pi r_{\text{base}}^4}\left(\frac{(a-L)}{(L-x)^2} + \frac{3}{(L-x)} - \frac{(L+2a)x}{L^3} - \frac{(a+2L)}{L^2}\right), \quad x \le a. \tag{B.12}$$

which simplifies to the top half of (3.4). To solve for the deflection at values of x greater than or

equal to a, we note that the moment is zero. This means we can write

$$y(x) = y(a) + \frac{dy}{dx}\bigg|_{x=a}(x-a) \tag{B.13}$$

Substituting in (3.6) evaluated at $x = a$ gives the bottom half of (3.4).

Appendix C

Effects of Taper on Whisker Deformation

This appendix consists of material from the following publication:

J. A. Birdwell, J. H. Solomon, M. Thajchayapong, M. A. Taylor, M. Cheely, R. B. Towal, J. Conradt, and M. J. Z. Hartmann, "Biomechanical models for radial distance determination by rat vibrissae," *Journal of Neurophysiology,* vol. 98, pp. 2439-2455, 2007.

We used Model 1 as expressed in (3.4) to explore two important consequences of the tapered geometry on whisker deformation, as would occur when a real whisker contacted an object. First, whisker taper ensures that the ratio between the displacement at some distance, *a*, and the force applied at *a* increases faster with *a* for the tapered whisker than for the cylindrical whisker. Intuitively, this makes sense: as a given force is exerted at increasing distances from the base, a tapered whisker will bend more than a cylindrical whisker. Figure C.1(a) illustrates this effect for a 50 μNewton force exerted at 10, 20, and 30 mm along the length of a 60 mm whisker with a base radius of 100 microns. For the force applied closest to the whisker base (*a* = 10 mm), the equations describing cylindrical and tapered whiskers yield almost the same deflected

whisker shape. As the value of *a* increases, however, the two results diverge, with the tapered

whisker deflecting far more than its cylindrical counterpart.

Both whiskers have a length L = 60 mm and a base radius r_{base}= 100 μm. **(b)** Theoretical force-displacement curves for cylindrical and tapered beams for the same values of horizontal distance *a* as in part (a). **(c)** Deflections resulting from an imposed vertical force, F, in the case that the tapered and cylindrical beams have matching radii at *a*, for *a* = 10, 20, and 30 mm. Arrows represent the locations of the imposed forces. **(d)** Force-deflection curves for cylindrical and tapered beams with matching radii at *a*, for *a* = 10, 20, and 30 mm. **(e)** Deflection of two cylindrical beams (base radii of 50 and 100 μm) and one conical beam (base radius of 100 μm) for a 50 μN force, showing the effect of whisker taper. **(f)** Deflections of the same cases as (e) on a log-log scale. **(g)** When a force is imposed 30 mm from the base, the length of the whisker does not affect how a cylindrical whisker will bend: the single blue trace shows results for both a 60 mm and a 40 mm whisker. In contrast, the shorter (40 mm) conical whisker bends much more than the longer (60 mm) whisker (red traces), when the same force is applied at the same position. **(h)** Relationship between deflection and whisker length, for a force applied at 10 mm. Deflections of the cylindrical whisker are unaffected by total whisker length (blue trace is a constant value). In contrast, deflections of the conical whisker fall off sharply with whisker length (red trace).

Figure C.1: Cylindrical (blue) versus tapered (red) beam models. For all graphs, Young's modulus was assumed to be 3.5 GPa. **(a)** Deformations of ideal cylindrical and tapered cantilever beams under a vertical force *F* imposed a distance *a* from the base, for three different horizontal values of *a*.

Figure C.1(b) shows displacement-force curves for models of cylindrical and tapered whiskers for forces applied at the same values distance a as in Figure C.1(a). In Figure C1(b), each value on the y-axis indicates the vertical deflection at point a along the whisker for the corresponding force F on the x-axis. In other words, Figure C.1(b) indicates how much a given whisker will deflect when a force is applied at point a, for both the tapered and cylindrical beams. In both cases, the force F increases linearly with the deflection $y(a)$ (as can be seen directly in (3.4)), but the displacement associated with a given force is considerably larger for the tapered whisker than for the cylindrical whisker.

The above analysis has indicated that (for a given force imposed at a given distance) a cylindrical whisker will deflect less than a tapered whisker of the same base radius. This result is not surprising because the radius (and hence the stiffness) of the tapered whisker at every point between the base and the contact point is smaller than the radius of the cylindrical whisker. We next asked: what happens when we apply the same force to cylindrical and tapered whiskers, but choose the radius of the cylindrical whisker to match the radius of the tapered whisker at the point where the force is imposed? The answer is illustrated in Figure C.1(c,d). The cylindrical whisker now deflects more than the tapered whisker. Again, this result should be somewhat intuitive, because of the difference in radius profiles from whisker base to contact-point.

Thus one consequence of whisker taper is to ensure a steeper relationship between displacement and force closer to the tip of the whisker. This result is summarized in Figure C.1(e) which plots the deflection $y(a)$ as a function of a, for a 50 μN force imposed at a. The curve for the tapered whisker (base radius 100 μm) falls between the curves for cylindrical

whiskers of base radii 50 and 100 μm. The effect is easier to observe in Figure C.1(f), which plots the identical data as Figure C.1(e), but on a log-log scale. Here it can be seen that the deflection of the tapered whisker initially matches the deflection of the cylindrical whisker with the larger radius, but as *a* increases the trace curves upwards towards the curve representing deflections of the smaller cylindrical whisker. The tapered geometry thus specifically accentuates the magnitude of deflection that will occur further out along the length of the whisker.

A second difference between the equations for tapered and cylindrical whiskers is that deflections in the tapered case depend strongly on the whisker length, *L*, whereas the deflections of the cylindrical case are indifferent of whisker length. In other words, how a whisker will react to a given imposed force depends on its total length. This effect is illustrated in Figure C.1(g), which compares the deflections of cylindrical and tapered whiskers of two different lengths (40 and 60 mm), but with the same base radius (100 μm). In all cases the same magnitude force is applied 30 mm from the base. The cylindrical whisker bends the same amount regardless of length, and so only one curve is seen (blue line). In contrast, the short tapered whisker bends considerably more than the longer tapered one (red lines).

The effect of whisker length is further characterized in Figure C.1(h). We simulated a 50 μN force acting 10 mm from the base of a whisker whose length varied from 11 to 60 mm, but whose radius was held constant. The vertical deflection at the location of the imposed force (10 mm from the base) was then plotted as a function of whisker length, for both cylindrical and tapered whiskers. As described for Figure C.1(g), the deflection of a cylindrical whisker does not vary with overall whisker length, and so there is only one curve (blue line). In contrast, shorter

tapered whiskers deflect far more than longer ones (red lines). As whisker length increases, the tapered result asymptotes to the cylindrical result. The implication for real rat whiskers is that for a force imposed at a particular distance (say 10 mm), longer whiskers will deflect much less than shorter ones. This result would hold true even if the base radii of all whiskers were the same. This result would not hold true if the whiskers were cylindrical.

Appendix D

Numerical Modeling of a Cantilever Beam

This appendix contains material from the following publications:

J. H. Solomon and M. J. Hartmann, "Robotic whiskers used to sense features," *Nature,* vol. 443, p. 525, Oct. 5 2006.

J. H. Solomon and M. J. Z. Hartmann, "Object profile sensing with a robotic whisker using only torque information," in preparation.

The problem of determining the shape of a cantilever beam subjected to a point load at the end is one of the oldest in the study of bending beams, having been investigated by Bernoulli and Euler in the 1700's. Precise solutions can be obtained through the use of elliptic functions [80], and recent methods allow the determination of all equilibrium shapes for given material and geometric properties and end load [81, 82]. Here, we are only interested in determining a small subset of possible equilibrium shapes, namely those that can be expected to arise during a whisker rotation of reasonable amplitude against on object. It is assumed that dynamic effects are negligible, allowing use of a standard elastica model of beam bending.

The Euler-Bernoulli beam equation can be written as:

$$d\kappa = \frac{M}{EI} \tag{D.1}$$

where $d\kappa$ refers to change in curvature, and can vary with M, E and I along the length of the beam. Computation of the shape of a cantilever beam for an arbitrary end load can be accomplished by dividing the beam into n nodes and writing (D.1) in the following form:

$$d\kappa_i = \frac{d\phi_i}{ds} = \frac{\bar{r}_i \times \overline{F}}{E_i I_i} \tag{D.2}$$

where ϕ is the tangent angle of the beam, s is the arc length coordinate, $\bar{r}$ is a moment arm, and $\overline{F}$ is the end load. Subscript i refers to the node number, which we define as 1 at the location of $\overline{F}$ and n at the beam base. By starting a node 1 and repeatedly calculating the location of the next node up until n, (D.2) provides an accurate, efficient, compact and easy-to-implement way of computing the shape of a beam due to an end load. Note that the generality of this method allows arbitrary inclination α of the force, arbitrary variation of E and I along the length, and arbitrary inherent curvature of the beam (so long as the radius of curvature is at least 10 times the beam depth at all nodes [34]).

Equation (D.2) can be used in at least two interesting ways to compute the shape of the beam and the moment at its base:

1) Have the "user" specify the arc length location S of the force, its magnitude F, and its inclination α.

2) Have the "user" specify the coordinates of the desired deflection point (this case only applies to zero friction, such that the force inclination is zero).

The first method involves straightforward iterative application of (D.2), while the second method is somewhat more involved. It can be solved by a numerical optimization technique which searches amongst possible combinations of F and S to achieve intersection of the beam with the desired deflection point at S. Friction must be assumed to be zero in order to find a unique solution. This technique was used in Chapter 3 ([83]) as well as [47].

In the case of the sweeping algorithm (Chapter 6), we are dealing with a straight beam of constant E and I, making (D.2) particularly straightforward to implement. We assume that the friction between object and beam is negligible, making the force perpendicular to the beam's longitudinal axis at the contact point ($\alpha = 0$). Figure D.1 depicts the process of computing the beam shape for a force F.

curvature exaggerated for clarity
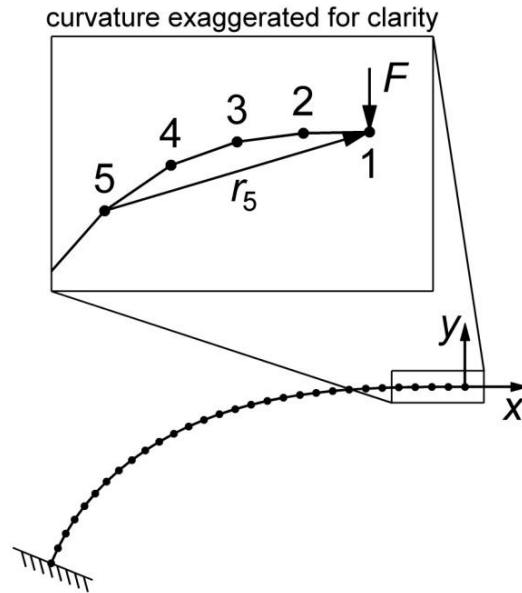
Figure D.1: The deflected shape of an inherently straight cantilever beam with a concentrated end load *F* acting perpendicular to the beam's longitudinal axis can be found using a simple iterative procedure depicted here. Only 30 beam nodes are shown for clarity, but a much larger number should be used for accurate results.

The procedure starts by placing node 1 at (0, 0) and node 2 at $(-ds, 0)$, where $ds = 1/(n-1)$ such that F acts at $s = 1$. The initial slope $\phi_1 = 0$. Successive node locations are then found by and iteratively applying the following equations, starting at $i = 2$ and ending at $i = n-1$:

$$\kappa_{i-1} = x_i \cdot F \tag{D.3}$$

$$\phi_i = \phi_{i-1} + \kappa_{i-1} \cdot ds \tag{D.4}$$

$$x_{i+1} = x_i - ds \cdot \cos \phi_i \tag{D.5}$$

$$y_{i+1} = y_i - ds \cdot \sin \phi_i \tag{D.6}$$

Once the beam shape is computed, its base point is translated to the origin, and it is rotated about its base by angle $-\phi_{n-1}$ to orient it as shown in Figure 6.2. Note that *EI* has been assumed to be 1, meaning that *F* is effectively normalized by s^2/EI.

Repeating the above process for a succession of forces ranging from 0 to F_{max} and storing the resulting beam shapes in a 2-D matrix amounts to pre-solving for all equilibrium shapes up to some maximum value of θ, θ_{max} (which depends on F_{max}). Figure D.2 shows these results for $F_{max} = 2.5$, which leads to $\theta_{max} \approx 45°$. A total of 10,000 nodes were used for high accuracy in computing the shapes, but only a subset of these points need to be stored in the look-up table due to the smoothness of the resulting curves. Similarly, the beam changes in a very continuous manner as *F* is increases, necessitating that only relatively small number of shapes be stored. A table of size 100×100 provides excellent accuracy.
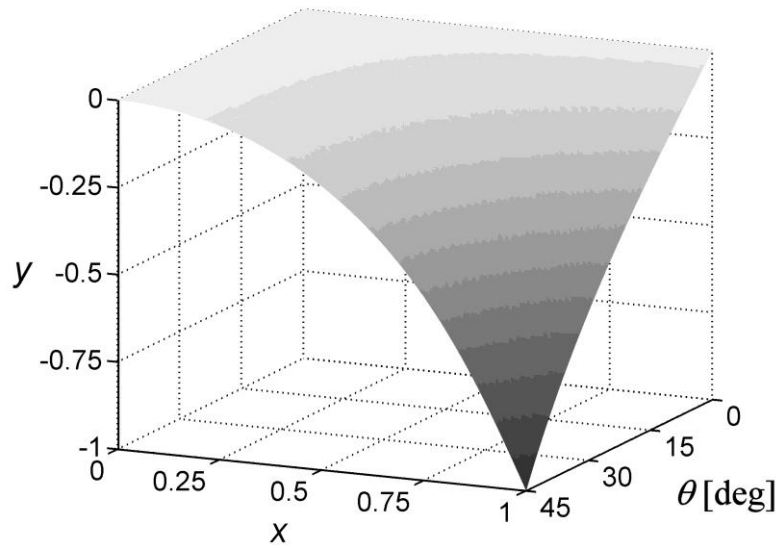
Figure D.2: A continuum of beam shapes up to θ_{max} = 45°, computed by using the method depicted in Figure D.1. Each beam length was normalized such that d_x = 1.

In general, one may wish to obtain the equilibrium shape based on various methods of query. In particular, (d_x, d_y), (r, θ), and (s, F, EI) all independently provide sufficient information to reconstruct the entire shape of the beam by interpolating the look-up table and scaling the units to match those provided in the query.

Appendix E

A Model of Lateral Slip

This appendix consists of material from the following publication:

J. H. Solomon and M. J. Z. Hartmann, "Artificial whiskers suitable for array implementation: Accounting for lateral slip and surface friction," *IEEE Transactions on Robotics*, to appear.

Equation (4.2) provides a relation between bending moment at the whisker base m_z, the radial distance d_x, and the pushing angle θ:

$$d_x = C \frac{\theta}{m_z} \tag{4.2}$$

Now, referring to Figure 4.2, it is clear that $\theta = \tan(d_y/d_x)$. For small angles, $\theta = d_y/d_x$, which we plug into (4.2) to obtain:

$$m_z = C \frac{d_y}{d_x^2} \tag{E.1}$$

Note that this equation holds when lateral slip occurs (Figure 4.4) because it simply relates moment in the z-direction to radial distance d_x and deflection in the y-direction, none of which are affected by independent deflection of the whisker in the z-direction (d_z). By symmetry, the same linear scaling between m_z and d_y also holds for m_y and d_z:

$$m_y = C \frac{d_z}{d_x^2} \tag{E.2}$$

Furthermore, from Figure 4.4, it is clear that

$$\tan \beta = \frac{d_x \theta - d_y}{d_z} \tag{E.3}$$

Combining (E.1), (E.2) and (E.3) and solving for d_x yields:

$$d_x = C \frac{\theta}{m_z + m_y \tan \beta} \tag{4.6}$$

Further inspection of Figure 4.4 reveals:

$$\tan \phi = \frac{d_z}{d_y} \tag{E.4}$$

Combining (E.1), (E.3) and (E.4) and solving for m_z yields:

$$m_z = \frac{C\theta}{d_x} \left(\frac{1}{\tan \beta \tan \phi + 1} \right) \tag{4.13}$$

Combining (E.2), (E.3) and (E.4) and solving for m_y yields:

$$m_y = \frac{C\theta}{d_x} \left(\frac{1}{\tan \beta + \cot \phi} \right) \tag{4.14}$$

Appendix F

Slip Behavior in the Presence of Lateral Curvature

This appendix consists of material from the following publication:

J. H. Solomon and M. J. Z. Hartmann, "Artificial whiskers suitable for array implementation: Accounting for lateral slip and surface friction," *IEEE Transactions on Robotics*, to appear.

Figure F.1 is a sensing plane diagram for the whisker rotating against a circle with initial contact point (y_c, z_c) relative to the center. Of course, the object need not literally be a circle; what matters is that any point along a (2-D) surface can be uniquely characterized by a single radius of curvature. Throughout this derivation, all distance units are normalized by contact distance d_x.
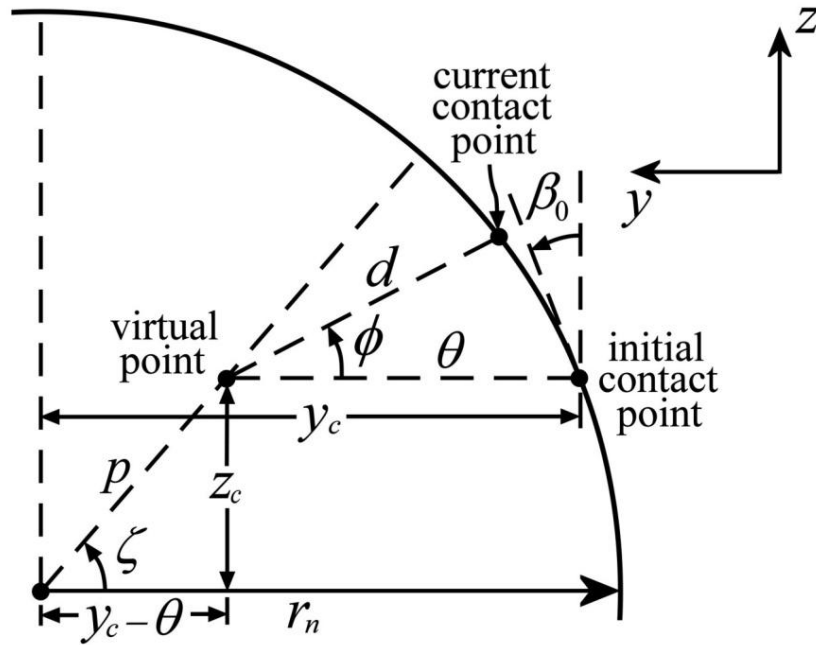
Figure F.1: A geometrical description of the sensing plane with lateral object curvature

We seek to characterize the performance of (4.6) as a function of four independent variables: r_n, θ, α and β_0. That is, we need to find expressions for m_z and m_y as functions of these variables. The first step is to observe the conspicuous relations:

$$\begin{cases} m_z = d\cos\phi \\ m_y = d\sin\phi \end{cases} \tag{F.1}$$

This immediately shifts our task to finding expressions for d and ϕ. As before, the whisker will laterally slip only if the initial contact angle is less than the friction cone angle, in which case the contact force will remain at the edge of the friction cone. Because the surface curvature now allows the contact angle to change, we modify (4.3) by replacing β with the angle ζ (defined in

Figure F.1) and noting that the constraint on slipping now depends on β_0, the surface slope in the sensing plane at the initial contact point:

$$\text{if } \begin{cases} \alpha \geq \beta_0, & \phi = 0 \\ \alpha \leq \beta_0, & \phi = \zeta - \alpha \end{cases} \tag{F.2}$$

Equation (F.2) can be reduced to

$$\phi = \max(0, \ \zeta - \alpha) \tag{F.3}$$

because $\zeta > \beta_0$ for any finite pushing angle θ.

To solve for ϕ requires that we express ζ in terms of the independent variables, so again examining Figure F.1, we find:

$$\zeta = \tan^{-1}\left(\frac{z_c}{y_c - \theta}\right) \tag{F.4}$$

The denominator of (F.4) may seem puzzling unless it is recalled that that each term has been normalized by contact distance d_x, so that y_c and θ are both unitless. To find expressions for y_c, and z_c, we again refer to Figure F.1 to find

$$r_n^2 = y_c^2 + z_c^2 \tag{F.5}$$

and

$$\tan \beta_0 = \frac{z_c}{y_c} \tag{F.6}$$

Equations (F.5) and (F.6) are combined to yield:

$$\begin{cases} y_c = \dfrac{r_n}{\sqrt{\tan^2 \beta_0 + 1}} \\[4mm] z_c = \dfrac{r_n \tan \beta_0}{\sqrt{\tan^2 \beta_0 + 1}} \end{cases} \tag{F.7}$$

Inserting (F.7) into (F.4), we obtain

$$\zeta = \tan^{-1}\left(\frac{r_n \tan \beta_0}{r_n - \theta\sqrt{\tan^2 \beta_0 + 1}} \right) \tag{F.8}$$

which can be inserted into (F.3) to find ϕ.

Now seeking an expression for d, we apply the Pythagorean Theorem to Figure F.1:

$$r_n^2 = \left(p\cos\zeta + d\cos\phi \right)^2 + \left(p\sin\zeta + d\sin\phi \right)^2 \tag{F.9}$$

Solving (F.9) for d,

$$d = \sqrt{r_n^2 - \frac{p^2}{2}\left(1 - \cos\left(2\left(\zeta - \phi\right)\right)\right)} - p\cos\left(\zeta - \phi\right) \tag{F.10}$$

where p can be found using the Pythagorean Theorem:

$$p = \sqrt{\left(y_c - \theta\right)^2 + z_c^2} \tag{F.11}$$

Finally, (F.7), (F.8), (F.10) and (F.11) can be combined to express d as a function of the independent variables, though we were unable to obtain a compact expression.

Vita

Joseph Hai Solomon

Education Northwestern University, Evanston, Illinois
Ph.D. in Mechanical Engineering   June 2008

University of Illinois at Chicago, Chicago, Illinois
M.S. in Mechanical Engineering   December 2003

University of Illinois at Urbana-Champaign, Urbana, Illinois
B.S. in Aerospace Engineering   June 2001

Journal Publications J. H. Solomon and M. J. Hartmann, "Robotic whiskers used to sense features," *Nature,* vol. 443, p. 525, Oct. 5 2006.

J. A. Birdwell, J. H. Solomon, M. Thajchayapong, M. A. Taylor, M. Cheely, R. B. Towal, J. Conradt, and M. J. Z. Hartmann, "Biomechanical models for radial distance determination by rat vibrissae," *Journal of Neurophysiology,* vol. 98, pp. 2439-2455, 2007.

V. Gopal, J. H. Solomon, N. Naik, and M. J. Z. Hartmann, "Two and three dimensional morphology of the rat vibrissal array," *Annals of Biomedical Engineering,* accepted with revisions.

J. H. Solomon and M. J. Z. Hartmann, "Artificial whiskers suitable for array implementation: Accounting for lateral slip and surface friction," *IEEE Transactions on Robotics,* to appear.

J. H. Solomon and M. J. Z. Hartmann, "Object profile sensing with a robotic whisker using only torque information," in preparation.

Conference Publications A. E. Schultz, J. H. Solomon, M. J. Peshkin, and M. J. Hartmann, "Multifunctional whisker arrays for distance detection, terrain mapping, and object feature extraction," in *Proceedings of the 2005 IEEE International Conference on Robotics and Automation*, 2005, pp. 2588-2593.